Wilton, Benjamin (2004) BURST Imaging at High Field. PhD thesis, University of Nottingham.

BURST Imaging at High Field

by Benjamin Wilton, MSc.

Thesis submitted to The University of Nottingham for the degree of Doctor of Philosophy, September 2004.

CONTENTS

Abstract

The work in this thesis is that undertaken by the author, except where indicated by reference, within the Sir Peter Mansfield Magnetic Resonance Centre at the University of Nottingham during the period October 2000 to September 2004.

BURST is a fast single-shot imaging technique used in magnetic resonance imaging. Most previous implementations of BURST on whole body systems have been carried out at fields of 1.5T and lower. In this work BURST has been implemented on a 3T whole body system. The signal and attenuation characteristics are discussed, leading to an approximate expression for the optimum echo time.

A novel method for controlling the pulse amplitude envelope is described. It is shown that this can lead to a modest gain in signal with little loss of resolution, or to a much greater gain in signal with more severe blurring of the image.

Frequency modulated RF pulses have been introduced in order to reduce the peak RF power required, which was found to be beyond the range of a 2kW amplifier. The resulting images show a quadratic phase roll in the readout direction, with no reduction in magnitude or image artefacts. A reduction in peak power of more than ten-fold is demonstrated. The maximum reduction factor possible is shown to be approximately equal to the number of pulses applied in the RF train.

The total RF power has been reduced by superimposing a sinusoidal oscillation onto the constant excitation gradient. Each pulse is applied at a gradient minimum, and hence need be of lower bandwidth, while the overall excitation is unchanged. The RF pulses are transformed using VERSE. A reduction in SAR of 32% is demonstrated. Greater reductions can be achieved by increasing the amplitude of the oscillation. However, this technique introduces a moderate amount of acoustic noise into the sequence.

Acknowledgements

I would like to use these few words to thank those who have willingly helped and encouraged me through this work, and the many who have lightened the last four or so years and made my time here perhaps that little bit too merry.

First of all, I wish to thank my supervisor, Paul Glover, with whom I've faced, and at times overcome, the challenges of BURST imaging.

I owe a debt of gratitude to those who, along the way, have given of their expertise and insider knowledge of the ways and wherefores of the 3T scanner, most notably Andy Peters. Also, for countless other bits of vital advice and knowledge I am indebted to many.

I have also had the benefit of visiting Simon Doran in the Royal Marsden and learning from his experiences with the technique.

I am grateful to many for their very good company: to Rachel, Sarah and Alison, for those early office years; to Silvia, Benito, Jim and Jose, for the countless welcome distractions; and to Dan K., Davide, Jiabao and the many more who have made it all most pleasurable. A particular note of thanks due to Alison, Martin, Jose, Walter and Jon, who went beyond the call of duty one evening to help spare my blushes.

Finally, to my family I am indebted for their complete support.

1 Introduction

1.1 Background

The development of magnetic resonance imaging has provided clinicians with a versatile tool for assessing and monitoring the health of the human body. Some of the areas of greatest interest, such as cardiac and functional imaging, call for techniques which can snap-shot the body many times a second. Likewise, a number of clinical investigations are impeded by the effects of cardiac and respiratory motion, and hence require fast imaging techniques.

A pool of techniques has been developed to meet these requirements. Echo planar imaging [1], the first of the fast techniques, provides images in less than 100ms. It relies on rapid switching of the gradients, which places particular demands on the hardware and leads to acoustically noisy imaging sequences. Furthermore, it is prone to image distortion and signal dropout resulting from field inhomogeneities, susceptibility differences and chemical shifts. Similar problems affect other gradient-based techniques, such as the multishot techniques FLASH [2] and FISP [3], which also are not as fast, and to some extent RARE [4] also, which additionally requires multiple 180° pulses, and hence has a high power deposition. At high magnetic fields these effects become more severe and alternative strategies will be needed.

In 1988 an RF-based imaging technique called BURST was first described [5]. It consists of a train of short RF pulses which are then refocussed to give a train of echoes, with only little switching of the gradients. It stands out as an acoustically quiet technique, an unusual feature among imaging methods. However, its main disadvantage is that is has an inherently low SNR compared with other rapid techniques. In the early to mid-nineties the sequence was successfully optimised by a number of groups, and the current BURST sequences have a much improved, if still comparatively low, SNR.

In recent years interest in BURST has faded and it has generated only a few occasional publications. However, with the increasing interest in high field human

imaging BURST would seem to be a potentially useful technique, which can benefit from the signal improvements of higher fields without suffering the problems of gradient-based techniques. The SE-BURST technique [6, 7], in which pure spin echoes are acquired, would be expected to produce less distorted images even at very high fields. Of the work so far presented of human studies on whole body systems using BURST most has been conducted at 1.5T or lower, and there is only one publication so far at 3T.

1.2 The scope of this thesis

This thesis describes the implementation of BURST on a 3T whole body system. A novel strategy is presented for controlling the pulse envelope. Also, the RF power demands were found to restrict the implementation of the optimised BURST sequence. Two strategies are presented which together are able to overcome these difficulties.

The first chapters outline the background theory, from the spin properties of the nucleus to the principles of image reconstruction. The theory of BURST is described in some detail. Following this, the system hardware is briefly described and a picture is given of the work required to implement the sequence.

In Chapter 5 the signal and attenuation characteristics of BURST are described and optimum imaging parameters are derived.

A novel method for controlling the pulse train envelope is presented in Chapter 6. This leads to an improvement in the signal, but with a worsening of the resolution. The gains to be made and the limits to the technique are explored in this chapter.

Frequency modulated pulses have been used to overcome the constraint of a limited peak RF power. In Chapter 7 the theory of these pulses is described and their consequences for BURST are discussed.

Finally, a further modification is given in Chapter 8 which brings substantial reductions to the total power deposition. The introduction of a time-varying gradient

brings the specific absorption rate (SAR) within the allowed range. The technique for transforming the RF pulses to preserve the response of the spins is also presented.

1.3 References

1. Mansfield, P., *Multi-Planar Image Formation using NMR Spin Echoes.* Journal of Chemical Physics, C, 1977. **10**: p. L55.

2. Haase, A., J. Frahm, D. Matthaei, et al., *FLASH imaging. Rapid NMR imaging using low flip-angle pulses.* J. Magn. Reson., 1986. **67**: p. 258-266.

3. Oppelt, A., R. Grauman, H. Fischer, et al., *FISP—a new fast MRI sequence.* Electromedica, 1986. **54**: p. 15–18.

4. Hennig, J., A. Nauerth and H. Friedburg, *RARE imaging: a fast imaging method for clinical MR.* Magn. Reson. Med., 1986. **3**: p. 823-833.

5. Hennig, J. and M. Mueri, *Fast imaging using Burst excitation pulses.* in 'Proc., SMRM, 7th Annual Meeting', 1988: p. 238.

6. Hennig, J. and M. Hodapp, *Burst imaging.* MAGMA, 1993. **1**: p. 39-48.

7. Lowe, I.J. and R.E. Wysong, *DANTE ultrafast imaging sequence (DUFIS).* J. Magn. Reson. Series B, 1993. **101**: p. 106-109.

2 Nuclear Magnetic Resonance

2.1 Introduction

Many atomic nuclei possess an intrinsic angular momentum, and associated with this angular momentum is a magnetic moment [1]. Pauli [2] suggested in 1924 that the hyperfine structure of atomic spectra was due to an interaction between this postulated magnetic moment and the orbiting electron. Nine years later the nuclear magnetic moment was measured by Eastermann and Stern [3] and by Frisch and Stern [4] from the deflection of a molecular beam, the method used earlier by Stern and Gerlach [5, 6] in their renowned experiments on the atomic magnetic moment. Rabi and colleagues [7] later (in 1939) made much more accurate measurements of nuclear magnetic moments with the incorporation of a resonant RF field into the deflection method. The leap to the solid state was made at the end of 1945 by two groups working independently. Purcell and his colleagues [8] detected resonant absorption in solid paraffin, while in Bloch's lab a method termed 'nuclear induction' [9] was used to detect resonance in water. From these formative experiments many and varied applications of nuclear magnetic resonance (NMR), from the detection of metabolites *in-vivo* [10] to the monitoring of hydrating cement [11], have sprung [12].

2.2 The nucleus

Angular momentum is quantised and is related to the spin quantum number I by

$$p = \hbar\sqrt{I(I+1)}\,, \tag{1}$$

where $\hbar$ is Planck's Constant divided by 2π and I is either an integer or a half-integer.

The measurable components of the angular momentum are given by

$$p_z = m_z\hbar\,, \tag{2}$$

where m_z may take $(2I+1)$ values, from I down to $-I$.

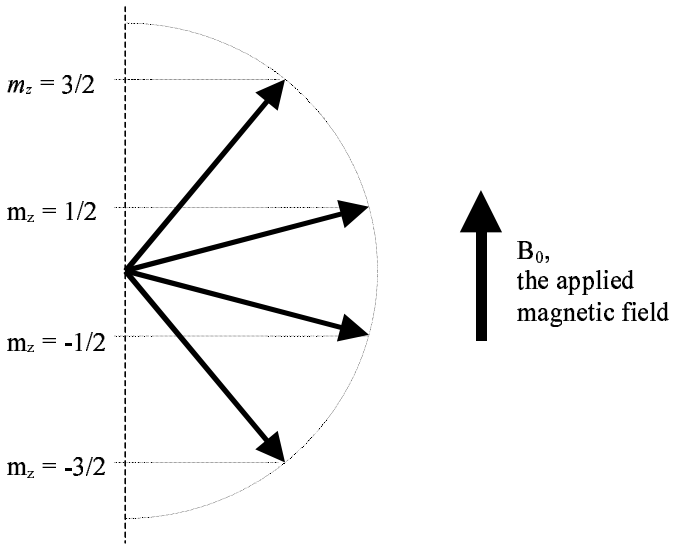

Figure 1 Quantisation of the nuclear spin for a spin 3/2 nucleus.

The magnetic moment, which arises as a result of the nuclear charge, is proportional to the angular momentum and is given by

$$\mu_z = \gamma p_z = \gamma \hbar m_z, \tag{3}$$

where γ is the gyromagnetic ratio.

In a magnetic field the energy of interaction of a nucleus depends on the measurable component of **μ** along the magnetic field,

$$E = -\mu_z B_0 = -\gamma \hbar m_z B_0, \tag{4}$$

where B_0 is taken to be along z.

The energy between states is given by

$$\Delta E = \gamma \hbar B_0. \tag{5}$$

Transitions between the different energy states can be induced by the application of an oscillating magnetic field. Quantum mechanical selection rules dictate that transitions can only take place between adjacent energy levels, hence there is a single energy of transition. The energy of radiation of frequency ω is $E = \hbar\omega$, and therefore the frequency of magnetic field required is given by

$$\omega_L = \gamma B_0 . \tag{6}$$

This frequency of radiation is termed the Larmor frequency.

2.3 The Boltzmann distribution

However, this radiation can induce both absorptive and emissive transitions with equal probability. For a system of nuclear spins in thermal equilibrium the population of each state will be given by the Boltzmann distribution

$$P(E_z) \propto e^{-\frac{E_z}{kT}} . \tag{7}$$

For the case of a hydrogen nucleus I=1/2 and there are only two states available, either the spins align with (↑) or against (↓) the field. The energies of these states are

$$E_{\uparrow/\downarrow} = \mp \frac{\gamma}{2} \hbar B_0 . \tag{8}$$

The relative populations of these states is

$$\frac{N_\downarrow}{N_\uparrow} = \frac{e^{\frac{\gamma\hbar B_0}{2kT}}}{e^{-\frac{\gamma\hbar B_0}{2kT}}} = e^{\frac{\gamma\hbar B_0}{kT}} . \tag{9}$$

At room temperature the energy of thermal vibrations is much greater than the separation of the spin energy levels. This results in near-equal populations in the two states.

Using power series expansion for an exponential,

$$\frac{N_\downarrow}{N_\uparrow} \sim 1 + \frac{\gamma\hbar B_0}{kT} \text{ for } \gamma\hbar B_0 << kT . \tag{10}$$

The fractional difference in population is therefore

$$\frac{N_{\downarrow} - N_{\uparrow}}{N_{\uparrow}} \sim \frac{\gamma \hbar B_0}{kT}. \tag{11}$$

In a 3T magnet at room temperature this population difference works out at ~10^{-5}, a very small amount. It can be fundamentally increased either by reducing the temperature (of limited clinical use!) or by increasing B_0. The observed signal is proportional to the net magnetisation, which depends on the difference in populations between these states. This is the cause of the fundamentally low signal in NMR. Hence, this is one of the main factors in the drive to higher magnetic fields.

2.4 The Classical Description

In classical mechanics a magnetic moment placed in a magnetic field experiences a torque, tending to align it with the field. This provides an easier way to think about the interaction of the spins and the field, and moreover this is a valid technique for spin ½ nuclei, for which the predictions of the classical and the quantum models agree exactly. The torque, **L**, is given by

$$\mathbf{L} = \boldsymbol{\mu} \times \mathbf{B}. \tag{12}$$

This causes the nuclei to rotate, changing their angular momentum, **p**, where

$$\frac{d\mathbf{p}}{dt} = \mathbf{L}$$

$$\Rightarrow \qquad \frac{d\boldsymbol{\mu}}{dt} = \gamma(\boldsymbol{\mu} \times \mathbf{B}) = \boldsymbol{\omega} \times \boldsymbol{\mu} \quad \text{where } \boldsymbol{\omega} = -\gamma \mathbf{B}. \tag{13}$$

This describes a precession about the applied field **B**, with frequency ω = |**ω**| r/s. This frequency is the same as the resonant frequency required for energy level transitions, ω_L (see Equation (6)).

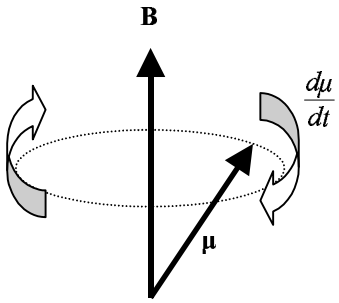

Figure 2 Precession of the nuclear magnetic moment about the magnetic field.

2.5 The bulk magnetisation

In an NMR experiment it is the net effect of all the spins in the sample which is observed. The sum of the individual magnetic moments gives **M**, the bulk magnetisation,

$$\mathbf{M} = \sum \boldsymbol{\mu} . \tag{14}$$

The motion of **M** is the same as that of **μ**, a precession about **B**, described by Equation (13),

$$\frac{d\mathbf{M}}{dt} = \boldsymbol{\omega} \times \mathbf{M} = \gamma(\mathbf{M} \times \mathbf{B}). \tag{15}$$

The magnitude of **M** in the presence of an applied field is that predicted by the quantum mechanical model above (see Section 2.3).

2.6 Rotating Frame of Reference

At this point it is useful to consider transforming Equation (15) into a frame of reference rotating with the Larmor frequency.

In the laboratory frame, *S*, $\mathbf{M} = M_x \mathbf{i} + M_y \mathbf{j} + M_z \mathbf{k}$.

In the rotating frame, *S′*, $\mathbf{M}' = M_{x'} \mathbf{i}' + M_{y'} \mathbf{j}' + M_{x'} \mathbf{k}'$.

A time derivative in one frame is transformed into the other frame according to

$$\left.\frac{d\mathbf{r}}{dt}\right|_{xyz} = \boldsymbol{\omega}\times\mathbf{r} + \left.\frac{d\mathbf{r}}{dt}\right|_{x'y'z'}, \text{ where } \boldsymbol{\omega} = -\omega\mathbf{k}. \tag{16}$$

Applying this transformation to Equation (15) gives the equation of motion in the rotating frame

$$\Rightarrow \qquad \gamma(\mathbf{M}\times\mathbf{B}) = \boldsymbol{\omega}\times\mathbf{M} + \left.\frac{d\mathbf{M}}{dt}\right|_{x'y'z'}$$

$$\Rightarrow \qquad \left.\frac{d\mathbf{M}}{dt}\right|_{x'y'z'} = \gamma\left[\mathbf{M}\times\left(\mathbf{B}+\frac{\boldsymbol{\omega}}{\gamma}\right)\right] = \gamma\left[\mathbf{M}\times\left(B-\frac{\omega}{\gamma}\right)\mathbf{k}\right]. \tag{17}$$

Substituting

$$\mathbf{B}_{eff} = \left(B-\frac{\omega}{\gamma}\right)\mathbf{k},$$

Equation (17) becomes

$$\frac{d\mathbf{M}}{dt} = \gamma(\mathbf{M}\times\mathbf{B}_{eff}). \tag{18}$$

Therefore, the motion in the rotating frame is equivalent to motion in the laboratory frame at a lower value of the field. For $\omega=\omega_L$ the value of the effective field is zero and there is no precession in the rotating frame. If an oscillating transverse magnetic field ($\mathbf{B_1}$) is applied at this frequency so as to be stationary in the rotating frame, the magnetisation can be seen simply to rotate about a fixed axis with frequency $\boldsymbol{\omega}=-\gamma\mathbf{B_1}$. This is the basis of the NMR experiment.

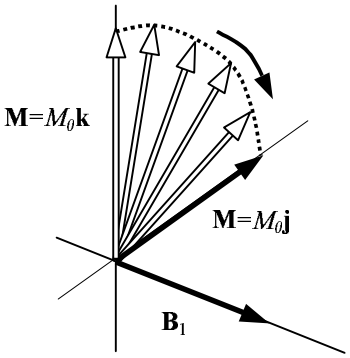

Figure 3 Rotating frame motion of **M** from its equilibrium position to the transverse plane under the action of a resonant transverse field, $\mathbf{B}_1$.

The magnetisation is rotated out of its equilibrium position as energy is absorbed by the system. In quantum mechanical terms this is equivalent to inducing transitions between the energy states.

2.7 Relaxation

Once the magnetisation is moved out of equilibrium it will be continuously drawn back to its equilibrium position by processes termed relaxation. The longitudinal component of **M** (M_z) experiences spin-lattice relaxation, whereby the energy of the spins are gradually exchanged with the surroundings. The transverse component of **M** (M_{xy}) experiences spin-spin relaxation, whereby spins dephase in the transverse plane causing M_{xy} to diminish.

The main mechanism which causes relaxation in water is based on dipole-dipole interactions. On a microscopic level each spin experiences not only the main field, but also a complicated small fluctuating field which arises from other dipoles in the vicinity. In a water molecule the dipolar field at the site of one proton is predominantly due to the other hydrogen nucleus in the same molecule. This local contribution to the field fluctuates with the motion of the molecule, as it jostles and turns amongst the surrounding water molecules.

T_1 relaxation

Those frequency components of the transverse local field which match the Larmor frequency will induce transitions between the spins states of the nuclei, just as the

applied RF also induced transitions. This is the basis of the return of the spins to their equilibrium position (T_1 relaxation mechanism). In general, the return of the longitudinal component M_z to the equilibrium value M_0 follows an exponential in time:

$$\frac{d\mathbf{M}_z}{dt} = \frac{\mathbf{M}_0 - \mathbf{M}_z}{T_1}$$

$$\Rightarrow \qquad \mathbf{M}_z(t) = \mathbf{M}_0 - (\mathbf{M}_0 - \mathbf{M}_z)e^{-\frac{t}{T_1}}. \tag{19}$$

T_2 relaxation

Any variation in the longitudinal component of the field will affect the precession of the spins and can lead to a loss of coherence between the spins. Immediately after an excitation pulse all the spins will have the same phase. Then, as each spin experiences the fluctuations in the local field, the precession rates of the spins will vary and they will accumulate different phases. Over time the individual spins will dephase more and more, and this will lead to a progressive decay in the transverse bulk magnetisation.

This leads to an exponential decay of the transverse component of the magnetisation:

$$\frac{d\mathbf{M}_{xy}}{dt} = -\frac{\mathbf{M}_{xy}}{T_2}$$

$$\Rightarrow \qquad \mathbf{M}_{xy}(t) = \mathbf{M}_{xy}(0)\, e^{-\frac{t}{T_2}}. \tag{20}$$

2.8 The Bloch Equations

The effects of relaxation can be incorporated into the equation for the magnetisation. This then yields the Bloch Equations, the phenomenological description of the magnetisation formulated by Bloch,

$$\frac{d\mathbf{M}}{dt} = \gamma\left(\mathbf{M} \times \mathbf{B}_{eff}\right) - \frac{M'_x}{T_2}\mathbf{i} - \frac{M'_y}{T_2}\mathbf{j} + \frac{M_0 - M'_z}{T_1}\mathbf{k}. \quad (21)$$

This equation can be further modified to take account of other effects, such as diffusion. In general, the attenuation due to diffusion takes the form of an exponential decay. The precise form depends on the choice of gradients and refocussing pules applied to the spins. It can be incorporated into the Bloch Equations with the addition of another term,

$$D\nabla^2(\mathbf{M}), \quad (22)$$

where D is the diffusion coefficient, which quantifies the mobility of the spins.

The Bloch Equations modifies to account for diffusion then become

$$\frac{d\mathbf{M}}{dt} = \gamma\left(\mathbf{M} \times \mathbf{B}_{eff}\right) - \frac{M'_x}{T_2}\mathbf{i} - \frac{M'_y}{T_2}\mathbf{j} + \frac{M_0 - M'_z}{T_1}\mathbf{k} + D\nabla^2(\mathbf{M}). \quad (23)$$

2.9 References

1. Andrew, E.R., *Nuclear Magnetic Resonance*. 1969: Cambridge University Press.

2. Pauli Jr., W., Naturwissenschaften, 1924. **12**: p. 741.

3. Estermann, I. and O. Stern, Zeischrift fur Physik, 1933. **85**: p. 17.

4. Frisch, R. and O. Stern, Zeischrift fur Physik, 1933. **85**: p. 4.

5. Gerlach, W. and O. Stern, *Uber die Richtungsquantelung im Magnetfield.* Zeischrift fur Physik, 1921. **8**: p. 110.

6. Stern, O., Zeischrift fur Physik, 1921. **7**: p. 249.

7. Rabi, I.I., S. Millman, P. Kusch, et al., Phys. Rev., 1939. **55**: p. 526.

8. Purcell, E.M., H.C. Torrey and R.V. Pound, *Resonance Absorption by Nuclear Magnetic Moments in Solids.* Physics Review, 1946. **69**: p. 37.

9. Bloch, F., W.W. Hansen and M.E. Packard, *Nuclear Induction.* Physics Review, 1946. **69**: p. 127.

10. Ackerman, J.J.H., T.H. Grove, G.G. Wong, et al., *Mapping of metabolites in whole animals by 31-P NMR using surface coils.* Nature, 1980. **283**: p. 167-170.

11. Gussoni, M., F. Greco, F. Bonazzi, et al., *1H NMR spin-spin relaxation and imaging in porous systems: an application to the morphological study of white portland cement during hydration in the presence of organics.* Magn. Reson. Imag., 2004. **22**(6): p. 877-889.

12. Gadian, D.G., *NMR and its Application to Living Systems*. 2nd ed. 1995: Oxford University Press.

3 Magnetic Resonance Imaging

3.1 Introduction

NMR spectroscopy soon found applications in the study of macromolecules and, later, in metabolism studies. However, not until the 1970s were the first steps made towards acquiring images. The early point scan methods were simple in concept and required only basic hardware [1]. The fonar method of Damadian et al [2, 3] and the sensitive point method of Hinshaw [4, 5] acquired signal from one spatial point at a time. Then, line scan techniques made use of selective irradiation to retrieve data from single lines of the image. The isolation of the line of interest was achieved by a combination of RF pulses, such as used in the selective refocussing method of Maudsley [6] or in the difference method of Hutchison [7], or, more crudely, the response of the receiver coil was used to similar effect. Later, the development of 2-D imaging techniques transformed the potential of NMR imaging (later abbreviated to MRI - magnetic resonance imaging). Hounsfield [8] had developed a projection reconstruction method for X-ray imaging, and the first NMR images were made also with this method by Lauterbur [9]. At a similar time Mansfield and Grannell presented their NMR diffraction technique for acquiring images [10]. In 1980 Edelstein et al [11] proposed the spin warp method, which is now a mainstay of MR imagers. Finally, sub-second imaging was realised by the development of EPI (Echo Planar Imaging) by Mansfield and co-workers [12, 13]. NMR imaging had come of age, from a 4 hour scanning method to snapshot imaging technique, with its potential as a essential clinical tool waiting to be explored.

3.2 Linear magnetic field gradients

In MRI field inhomogeneities are, for the most part, considered a hindrance, degrading images and reducing signal. On the other hand, a controllable field variation is the key to enabling discrimination between regions of the sample, and thereby the generation of an image. The simplest variation is a linear increase in one direction. As described in the previous chapter, the spins precess at a rate proportional to the field they experience, and in this case this leads to a linear increase in Larmor frequency (and a linear increase in phase with time). Hence, a

field gradient can be used to map the positions of spins to precession frequencies which are observed in the detected RF signal. In a similar sense the selective response of different frequencies of spin to an applied RF pulse can be translated to a selective positional response by use of a field gradient again. This is termed selective excitation and is discussed in the next section before moving on to the principles of encoding the RF signal in the subsequent sections.

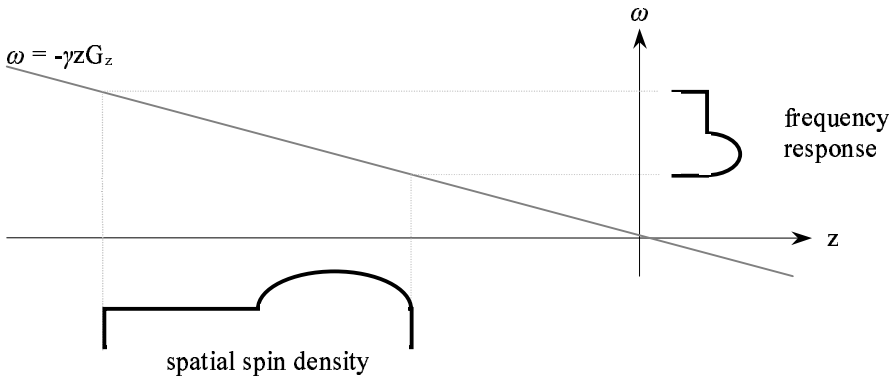

Figure 4 A linear gradient maps the positions of spins along the gradient direction to the frequency of precession.

3.3 Selective Excitation

The first step in many an MRI experiment is the application a selective RF pulse in the presence of a linear gradient field, which constrains the region of excited spins to a single slice of the sample.

If a linear field gradient in the same direction as the main field is applied the field varies with position as

$$B = B_0 + zG_z, \tag{24}$$

where B_0 is the main applied field, G_z is the gradient field in the z direction and z is the position along the gradient.

The Larmor frequency then varies as

$$\omega_L = -\gamma(B_0 + zG_z). \tag{25}$$

The response to any RF pulse varies with the frequency offset of the spins. The Bloch Equations for the transverse components of the magnetisation in the absence of relaxation are

$$\frac{dM_x}{dt} = \omega_y M_z - \omega_z M_y \tag{26}$$

and

$$\frac{dM_y}{dt} = \omega_z M_x - \omega_x M_z . \tag{27}$$

Writing the transverse magnetisation as a complex quantity $M_\perp = M_x + iM_y$ these two equations can be condensed into one

$$\frac{dM_\perp}{dt} = i\left(\omega_z M_\perp - \omega_\perp M_z\right), \tag{28}$$

where $\omega_\perp = \omega_x + i\omega_y$.

For small flip angles $M_z \sim M_0$ throughout. Substituting for M_z this equation can now be solved for a given ω_z as follows

$$M_\perp(\omega_z, T/2) = -iM_0 e^{i\omega_z \frac{T}{2}} \int_{-\frac{T}{2}}^{\frac{T}{2}} \omega_\perp e^{-i\omega_z t}\, dt = -iM_0 e^{i\omega_z \frac{T}{2}} \hat{F}(\omega_\perp), \tag{29}$$

where the RF pulse $\omega_\perp$ extends from $-T/2$ to $T/2$, and $\hat{F}(\omega_\perp)$ is the Fourier transform of $\omega_\perp$.

Therefore, for small flip angles the response of the spins is approximately proportional to the Fourier transform of the pulse. This is termed the linear approximation, and even for higher flip angles it is still a useful guide to the response of the spins.

If a rectangular slice of spins is to be excited, this would require a sinc profile RF pulse. In practice there are limitations on the durations of the pulses that can be used. Other techniques can be used to tailor the exact response of the spins as required.

Equation (29) above also describes the requirement of a refocussing gradient. In general, if the RF pulse is symmetric in amplitude and anti-symmetric in phase i.e. it displays Hermitian symmetry, its Fourier transform will have constant phase. For example, any even real pulse fulfils this condition. Then, the only contribution to the phase is from the factor $e^{i\omega_z T/2}$. This linear phase through the excited slice can be removed by reversing the linear gradient for a time $T/2$ after the pulse. This reverses the precession rates and leads to complete 'unwinding' of the spins.

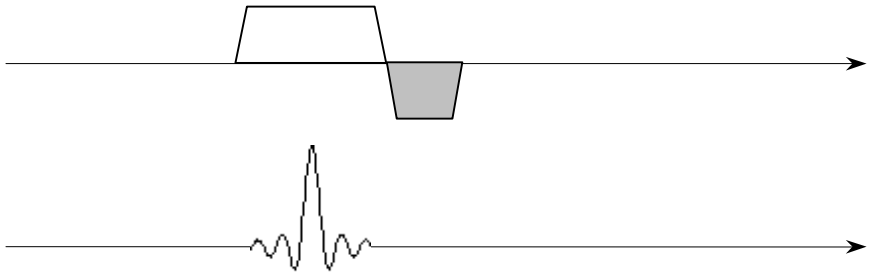

Figure 5 Gradient reversal removes the dephasing through the slice. The area of the shaded gradient lobe is half that of the unshaded lobe.

3.4 Frequency and phase encoding

Once spins have been excited by an RF pulse they immediately begin to relax, and in so doing emit radiation at the Larmor frequency. A linear field gradient can be applied to introduce a variation in Larmor frequency, as described above:

$$\omega_L = -\gamma(B_0 + xG_x),$$

where G_x is the field gradient in the x direction.

The signal from a spin at position x will vary as

$$S(x,t) \propto \rho(x)e^{i\omega_L t}, \tag{30}$$

where $\rho(x)$ is the projected spin density at position x along the field gradient.

The overall detected signal is therefore

$$S(t) \propto \int_{all\ x} \rho(x) e^{-i\gamma(B_0 + xG_x)t} dx . \tag{31}$$

Removing the component due to the main field (a process similar to the receiver demodulating the signal to baseband frequency) this becomes

$$\propto \int_{all\ x} \rho(x) e^{-i\gamma x G_x t} dx .$$

Then, substituting $\omega' = -\gamma x G_x$

$$S(t) \propto -\frac{1}{\gamma G_x} \int_{all\ \omega} \rho(-\frac{\omega'}{\gamma G_x}) e^{i\omega' t} d\omega' \ . \tag{32}$$

As expected, this is the inverse Fourier transform of the spin density in the x direction; that is, it is the sum of a series of spectral components weighted by the spin density. The original spin density can then be recovered by inverting the transform. This method of acquiring the profile is termed frequency encoding.

However, this gives only a 1-D projection of the excited region of the sample. The function $\rho(x)$ is the net sum of spin densities with position co-ordinate x. In general, this will be all spins within a plane or, following a slice selective excitation, along a line. In order to be able to further discriminate between spins, to be able to build up a 2-D image, further data has to be acquired. One option is to rotate the projection axis to obtain more projections, each containing contributions from different sets of spins. If sufficient projections are acquired, the signal due to spins at different locations can be calculated, thereby enabling a 2-D image to be reconstructed. This technique, termed projection reconstruction, is the basis of X-ray CT imaging, but is no longer a routine technique in MRI.

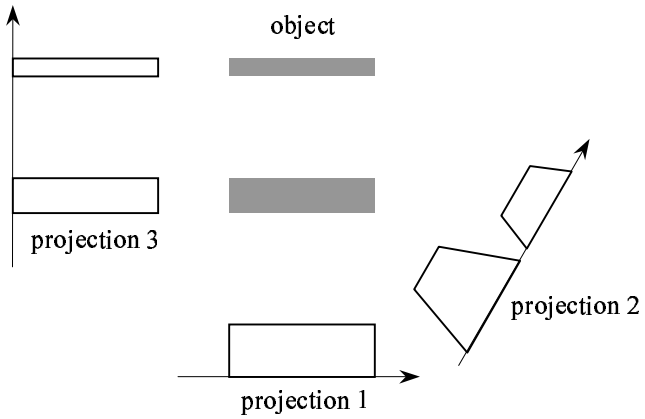

Figure 6 Projections can be acquired at different angles. From sufficient projection angles a complete image can be reconstructed.

The primary technique for encoding along further spatial dimensions is that of Fourier encoding once again. Rather than change the angle of the projection axis, the same axis is maintained throughout, but prior to acquiring each projection, the spins are first encoded along the orthogonal axis. This gives a projection of Fourier components, from which a full 2-D set of Fourier data can be built up.

Firstly, Equation (32) can be rewritten in terms of spatial (instead of temporal) frequency

$$S(t) \propto \int_{all\ x} \rho(x) e^{-i\gamma x G_x t}\, dx, \tag{33}$$

$$\Rightarrow \qquad S(k_x) \propto \int_{all\ x} \rho(x) e^{i 2\pi k_x x}\, dx, \tag{34}$$

where $k_x = -\dfrac{\gamma G_x t}{2\pi}$. k_x is a spatial wavenumber.

Consider the evolution of spins along the x direction. Adjacent spins precess at slightly different frequencies and this produces a phase roll, or winding of the spins, along the gradient direction. This yields a signal proportional to the Fourier component at the spatial period of the phase winding. In this way the encoding is achieved by modulating the phases of the spins – hence, 'phase encoding'. More generally the gradient need not be constant, and k_x can be written

$k_x = -\frac{\gamma}{2\pi}\int G_x dt$. Mathematically, this is tantamount to frequency modulation, however phase encoding provides a more general tool for appreciating the Fourier encoding technique.

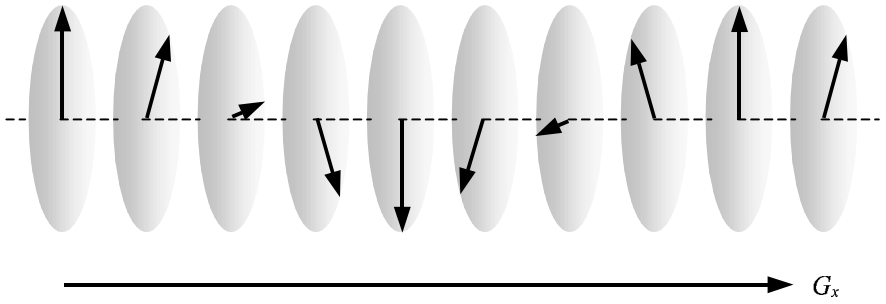

Figure 7 The spins are wound up along the gradient direction.

By introducing a 2nd orthogonal gradient similar modulation can be imposed along this direction too. The resultant signal is then a 2-D Fourier component of the image plane

$$S(k_x, k_y) \propto \int_{all\ x\&y} \rho(x,y) e^{i2\pi k_x x} e^{i2\pi k_y y} dxdy. \tag{35}$$

where now $\mathbf{k} = -\frac{\gamma}{2\pi}\int \mathbf{G}\, dt$, where $\mathbf{k} = \begin{pmatrix} k_x \\ k_y \end{pmatrix}$ and $\mathbf{G} = \begin{pmatrix} G_x \\ G_y \end{pmatrix}$.

This is the signal equation; it is simply the 2-D Fourier transform of the spin density. This can easily be expanded to a third dimension to give 3-D Fourier components.

3.5 k-space

The Fourier components which are read out describe a function in k-space, which can then be inverted to give the spin distribution. The gradients are used to vary the k_x and k_y components and thereby steer a path through k-space. It is not possible to acquire a continuum of data points in k-space, but instead the data is discretely sampled over a finite region. Conventionally the data is sampled at Cartesian grid

points over a rectangular region of k-space of dimensions 2^{nx} x 2^{ny}, which allows use of the Fast Fourier Transform (FFT) algorithm. The consequences of this for the reconstructed image can be understood from sampling theory.

Discrete sampling

Consider a 1-D function, *g(k)*, which is sampled at intervals Δk. This is described mathematically as a multiplication by a comb function (a periodic train of δ functions). The Fourier transform of the sampled function is given by the convolution of the transform of the function *g(k)* with another comb function, of period $2\pi/\Delta k$.

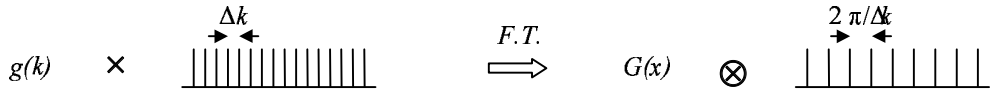

Figure 8 A sampled function and its Fourier transform.

This will result in an overlap between adjacent functions unless G(x) is contained within a range equal to $2\pi/\Delta k$, the sampling frequency. If *g(k)* represents a signal in time, sampled at intervals Δt, then *G(x)* has to have a bandwidth no greater than $2\pi/\Delta t$. This determines the field-of-view (FoV) of the image. In practice, frequencies outside of the FoV can be filtered out prior to sampling (in the case of frequency encoded data).

Alternatively, in terms of the Nyquist theorum the signal has to be sampled at twice the maximum frequency within the signal in order to be able to accurately determine all components. If the signal contains frequencies from $-\omega/2$ to $\omega/2$, then it must be sampled with frequency ω.

Truncation

k-space is only sampled over a limited range. This is equivalent mathematically to multiplying the full k-space data by a top hat function to truncate the data. Following Fourier transform this results in the convolution of the image with a sinc function, which places a limit on the resolution.

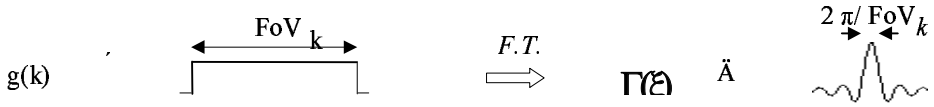

Figure 9 A truncated function and its Fourier transform.

At this point it is interesting to note a connection with BURST imaging. The comb function and top hat function above can be used to describe the basic BURST excitation. Therefore, analysis of BURST in the linear regime involves identical expressions, as is described in later sections.

3.6 Image Sequences

There are various strategies for mapping out k-space. Most imaging sequences record k-space data at Cartesian grid points, which can then be easily Fourier transformed. Imaging sequences might scan across a single line of k-space at a time, re-exciting the spins between successive acquisition – so-called multi-shot techniques. Alternatively, the entire k-space data set can be acquired after one excitation – single shot techniques. This can be achieved using a single echo to trace out a single long path, either with the gradients or with additional RF pulses, or by using a multiple RF excitation which gives a train of echoes, each of which can be separately encoded.

Single shot techniques, of which BURST is one, are by their nature fast. Multishot techniques in general are slower but give a higher SNR. However, they can be made almost as fast as single shot techniques if the time between successive excitations is kept as short as possible.

Multishot sequences

Spin Warp imaging [11], developed by the Aberdeen group in 1980, is the archetypal Fourier image technique. k-space is traced out one line at a time with a delay between excitations to allow the magnetisation to return to equilibrium.

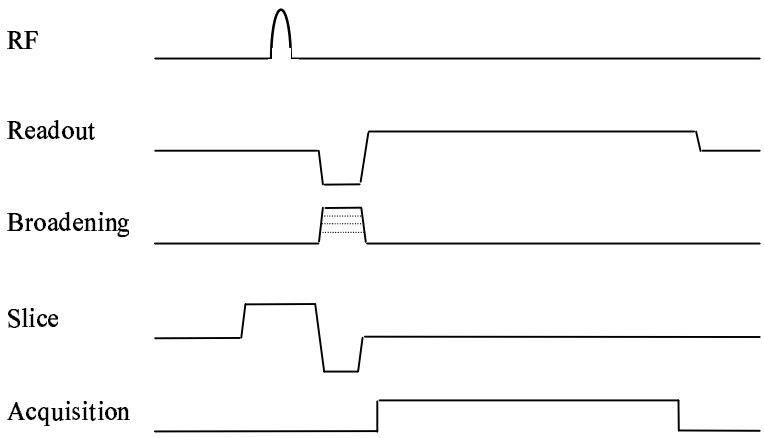

Figure 10 The Spin Warp pulse sequence.

Reducing the repetition time of the Spin Warp sequence produces the FLASH (Fast Low Angle Shot) sequence [14], in which the gain in imaging speed is offset by a reduction in SNR. In this sequence the longitudinal magnetisation reaches an equilibrium value short of M_0, where the recovery of M_z between excitation pulses exactly matches the loss of M_z due to the pulses. More generally, there is a family of similar sequences with short TR and repeated refocussing which are termed steady state sequences. As gradient echo sequences they tend to suffer from signal loss in inhomogeneous regions of field.

Single shot sequences

The RARE (Rapid Acquisition with Relaxation Enhancement) sequence [15] uses 180° pulses to continuously recycle the magnetisation after each traverse across k-space. The signal attenuation is primarily due to T_2. The multiple number of 180° pulses results in a high RF power requirement.

In EPI (Echo Planar Imaging) [13] the transverse magnetisation is continuously encoded by means of the gradients alone. In the MBEST version the magnetisation tracks back and forth along consecutive lines of k-space as one gradient is reversed and the other blipped, giving symmetrical coverage of k-space. Signal attenuation is due to both T_2 & T_2^*. Susceptibility effects can lead to geometric distortion and signal drop out, with a greater effect at higher fields. Also, the high frequency

switching of the gradient is very demanding on the gradient coil structures and leads to high levels of acoustic noise.

An alternative, if now uncommon, method of mapping out k-space with gradients is that of spiral scan imaging [16]. Starting at the centre of k-space a spiral route is taken, passing first through the low frequencies close to the centre, then moving to the higher frequencies. This makes gentler demands on the gradients, however the data has to be rebinned into a Cartesian grid before Fourier processing can take place.

QUEST (Quick Echo Split Imaging Technique) [17], like BURST, is a technique that does not recycle coherences, but which instead generates multiple coherences by the application of multiple RF pulses. A short train of RF pulses is applied in the presence of an in-plane gradient. Each pulse splits the magnetisation into different pools which evolve individually to give rise to echoes. This analytical perspective is described by the extended phase graph algorithm [18], which can be used to show that the maximum number of echoes which can be generated by n RF pulses is $E_n=3^{n-2}$. Therefore, the magnetisation can be split into several components, each of which can be refocussed and used to encode a single line of k-space. QUEST uses as few pulses as possible to generate sufficient echoes to cover k-space, choosing the interpulse spacings so that no echoes are superposed. In general, the echoes will vary in amplitude and phase and will have individual T_1 and T_2 weightings. The pulse flip angles can be optimised (for a given object) to reduce these variations, but significant differences will remain, which will lead to severe ghosting artefacts. This can be somewhat overcome by acquiring a calibration echo train, which will add the total imaging time. The SSHQ (Single Shot Hybrid QUEST) technique [19] incorporates the calibration set in a single acquisition, thereby maintaining the single shot nature of the technique. However, the primary drawback is the low SNR.

3.7 BURST

3.7.1 Introduction

In contrast to QUEST the signal in BURST is the sum of several coincident echoes. A long train of regularly spaced RF pulses is applied in the presence of an in-plane gradient. The magnetisation is refocussed, either with a 180° pulse or with a gradient reversal. Slice selection can be introduced through the 180° pulse and the echoes are phase encoded with a further orthogonal gradient, which is applied during the readout period.

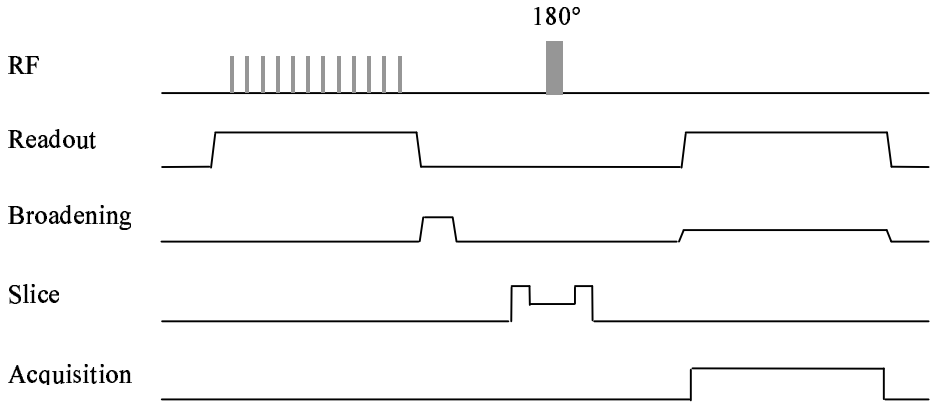

Figure 11 Spin echo variant of the BURST imaging sequence.

3.7.2 Formation of echoes

The 64 pulse BURST train above results in 64 echoes. However, each pulse of the train splits the evolving magnetisation into a number of separate components. As described earlier this can result in very many echoes, far more than the number of pulses. This is not the case in BURST. Firstly, the individual flip angles are generally small, which means that the echoes resulting from the interactions of the pulses are very small. More importantly, the periodic spacing of the pulses leads to echoes which exactly coincide, which reduces the observed number of echoes to just the number of applied pulses. In fact, this is not the complete picture. If the readout gradient is held on after the last pulse has been applied, another train of echoes, 63 in number, will be observed, which are generated through the interactions of individual pulses. These echoes can then be refocussed by the 180° pulse to give a further train of echoes. In general, these ‘direct’ echoes have much smaller amplitudes than the

'mirror' echoes (those described above) and they are not used for acquiring image data. Zha & Lowe [20] describe more fully these different echoes.

The amplitudes and phases of the observed echoes depend on the different component echoes present. At low flip angles spin echoes form, resulting from the interaction of excitation pulses with the 180° pulse. These are termed primary echoes and their amplitudes reflect the available longitudinal magnetisation at the time of the corresponding RF pulse. At higher flip angles the contributions from the interactions between the individual excitation pulses are much more significant and can lead to very variable amplitudes and phases of the echoes. These higher order echoes scale in amplitude with $sin^k(\theta)$, where k is an odd integer ≥ 3, and their phases depend on the phases of their generating pulses (and so are, in general, different to the primary echo phases). Hence, the amplitude of the composite echo is lower than that of the primary echo alone. However, further developments of BURST have led to a number of techniques for phase modulating the RF pulses [20-24], which turn these destructive interferences into constructive ones, thereby improving the efficiency of the sequence.

However, even for optimised sequences the resultant echoes cannot be accurately predicted, because the amplitudes and, in particular, the phases depend on the pattern of B_1 inhomogeneity across the sample. The flip angles depend on the local B_1 field, and so the relative amplitudes of the different order echoes ($sin(\theta)$, $sin^3(\theta)$, $sin^5(\theta)$…) will depend on the local B_1. Hence, the resultant superimposed echoes will have amplitudes and phases determined by the pattern of the B_1 field. At higher fields the B_1 field tends to be more inhomogeneous and so this is more of an issue.

One way to account for this variation in the amplitudes and phases is by performing a calibration run and acquiring echoes in the absence of a phase encoding gradient, which would provide data for correcting the echoes in an imaging experiment. Alternatively, reducing the flip angle of the pulse train will result in a diminished contribution from higher order echoes, however it would also reduce the amplitudes of the primary echoes.

Another way to overcome this problem of B_1 inhomogeneity is to use only pulses with phases of either 0° or 180°, so that higher order echoes will have these phases also. In this way the phase variation can be eliminated, but there will still be variability in the contributions of the amplitudes of higher order echoes to the observed echoes.

3.7.3 Frequency domain

The DANTE pulse train, the regularly-spaced, short, hard rf pulses utilised in BURST, was first proposed to overcome limitations of NMR spectrometers; primarily that the transmitter frequency could not be adjusted finely enough for certain experiments and that it did not settle rapidly enough after being switched [25]. The RF pulses have a cumulative effect, exciting the magnetisation at the transmitter frequency and at a series of sideband frequencies displaced periodically either side of the transmitter frequency, whilst in-between frequencies experience very little excitation.

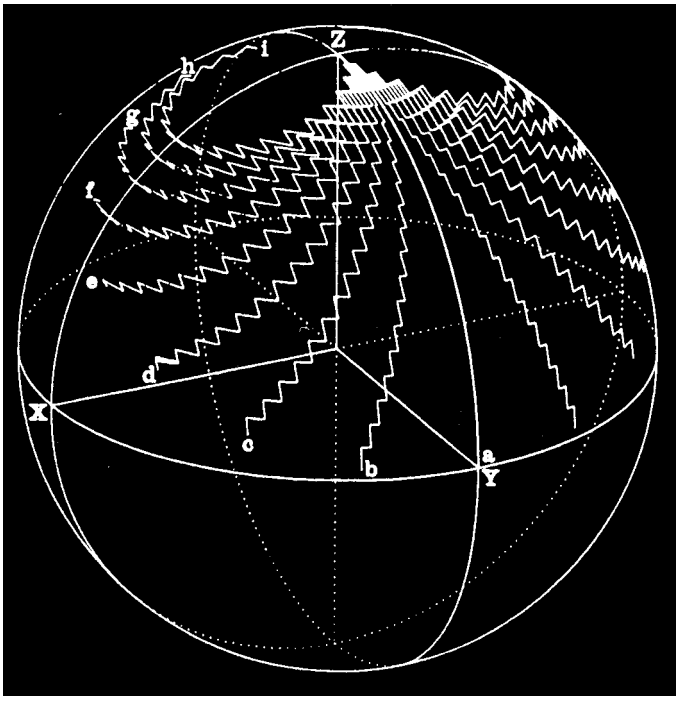

Figure 12 The motion of the magnetisation vectors in the rotating frame (from [26]).

This can be easily visualised by following the motion of a macroscopic magnetisation vector at a frequency offset $\Delta\omega$ from the transmitter frequency ω_0,

ignoring the effects of relaxation. In a frame of reference rotating at ω_0, the first RF pulse tips the magnetisation vector an angle α about the x axis, and this then precesses about the z axis through an angle $\theta = \Delta\omega\tau$. The next RF pulse tips the magnetisation further, and then it precesses again. On resonance, as there is no precession, this produces a cumulative tipping effect, which also occurs at frequencies displaced by $\Delta\omega=(2n\pi)/\tau$, where n is an integer, from the transmitter frequency. At these frequencies the precession carries the magnetisation an integral number of revolutions about the z axis between successive RF pulses. At frequencies in-between these resonances, $\Delta\omega=(2n\pi+\theta)/\tau$, where θ gives the excess angle of precession between RF pulses, the magnetisation is carried progressively further away from the YZ plane, and hence this results in a lesser cumulative excitation. At small frequency offsets the magnetisation vectors curl away from the YZ plane and fall short of the XY plane, and at more distant frequencies the magnetisation vector makes small, approximately circular, trajectories close to the z axis as shown.

Hence, the excitation is highly selective, resulting in narrow strips of excitation. Since only a small proportion of the magnetisation (~1/N) is fully excited the echoes will have a comparatively low SNR. However, this excitation pattern has also been made use of to achieve a higher imaging resolution. The intrinsic resolution of the sequence is equal to the spacing of the sidebands, whereas the narrow strips of excitation allow for a sub-pixel localisation of the spins. This has been used in a microscopic imaging technique developed by Taniguchi et al. [27].

> *It is the motion of the magnetisation vector at the first sideband frequency which gives the DANTE sequence its name. In the second section of Dante Alighieri's "La Divine Commedia", the "Purgatorio", Dante and Virgil make a journey through Purgatory, in which there are ten circular ledges, one above the other, running around a mountain. In order to progress towards heaven, souls must circumnavigate each ledge before making their way up to the next. This motion parallels that of the tip of the magnetisation vector at the first sideband frequency, albeit*

running in reverse temporal order. Hence the name DANTE - Delays Alternating with Nutations for Tailored Excitation.[26]

A more quantitative analysis of the excitation pattern can be achieved by restricting the flip angles to small values, such that the linear approximation applies and Fourier analysis can be used. In this case an approximate excitation profile is obtained from the Fourier transform of the pulse sequence. This approximation has been found to remain useful for a phased multi-pulse sequence (as described later), even when the sum of the flip angles is much larger than $\pi/2$, provided the excitation is reasonably uniform (so that even at spectral peak the total nutation is not too far beyond $\pi/2$)[20].

Mathematically, the DANTE pulse train can be derived from three basic functions: an infinite, periodic train of δ functions and two rectangular (top hat) functions, as shown below.

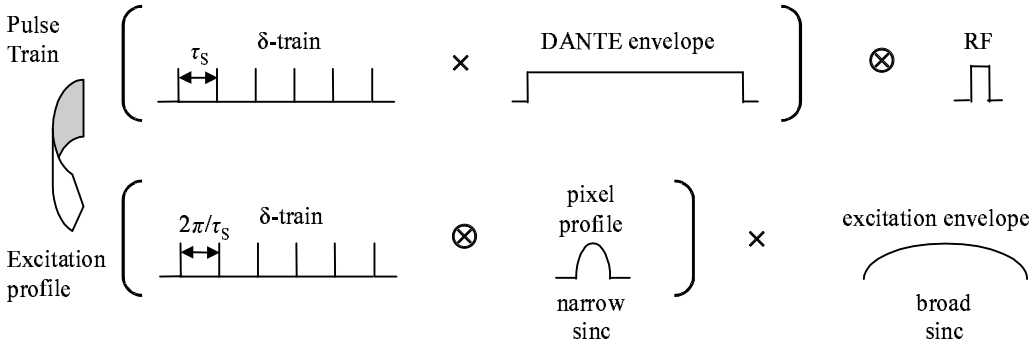

Figure 13 Fourier transform of the DANTE pulse train

The Fourier transform is determined by the convolution theorem. This shows that the excitation results in a periodic train of narrow sinc functions modulated by a broad sinc function. In terms of imaging, the spins are excited in narrow planes through the sample. Then, the 180° pulse selects spins in an orthogonal plane so that the excited spins lie in strips within the imaging plane. The spectral width of the strips is equal to the width of the narrow sinc, $2\pi/N\tau_s$, where N is the number of pulses applied and τ_s is the pulse spacing. The spacing of the strips is equal to $2\pi/\tau_s$ (see Figure 13 above), which is equal to (N x strip width). Hence, only $1/N$ of the spins are excited.

The duration of each sampled echo determines the spectral resolution, that is, spectral resolution = 2π/(sampled echo duration). However, since the sampling duration is necessarily the same as the spacing of the pulses ($=\tau_s$), the spectral resolution is equal to the spacing of the strips, $2\pi/\tau_s$. That is, there is exactly one excited strip within each pixel of the image. The broad sinc function reflects the bandwidth of the individual RF pulses. In practice, the excitation needs to be uniform over the FoV, and this can be achieved by shaping the RF pulses. This analysis is very similar to the digital sampling theory described earlier in Section 3.5, which gave rise to aliasing and put a limit on the resolution.

Further developments in BURST have introduced phase modulation and frequency switching. These techniques produce a near-complete excitation and lead to much higher SNR, although still lower than in EPI. These are discussed in the later chapter on phase and amplitude modulation of the RF train.

An interesting connection has been made between BURST imaging and a scanning technique from the early days of MRI. In 1976 Mansfield and Maudsley [28] proposed a technique known as planar imaging, whereby several lines of the object are simultaneously excited, and then the echoes are acquired with a slightly skewed gradient which projects all the image data at once. Matsuda et al. [29] showed that BURST works in an identical way. Firstly, they note that the echo train acquired is simply a 1-D projection of the image, since the entire echo train is observed under a fixed gradient. In this sense the phase-encoding gradient tilts slightly the overall orientation of the resultant gradient away from the readout gradient. This angle of tilt of the gradient, and so of the projection axis, is such that the projection signal at a point on the echo train originates from one and only one strip of the excited magnetisation in the field of view, as indicated below. In this way each point of the projected image can be traced back to a point on one of the strips. A 1-D Fourier transform can be performed on the echoes and then the data can be rebinned into a 2-D array to produce an image.

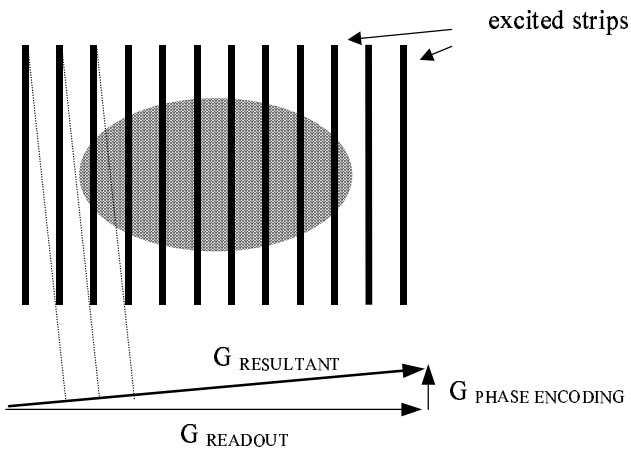

Figure 14 Line scanning interpretation of BURST. Each point on the strips is uniquely frequency-encoded by the resultant gradient.

3.7.4 BURST characteristics

BURST is an interesting imaging method that works in a fundamentally different way to most other methods. One drawback of the BURST method is that it produces images with a relatively low SNR. However, in its favour is that fact that it is much less demanding on the gradients than other techniques such as EPI, with the added benefit of being an acoustically quiet technique. The echoes are both T_2- and diffusion-weighted, but have zero (or otherwise equal) T_2^* weighting. This gives BURST a marked advantage over gradient-based techniques, for which distortion and signal dropout can be a problem, especially at high field. Also, BURST has potential as a volume imaging technique, given that the excitation is inherently volumar. All this suggests that BURST is best suited to high field work, however the majority of work published to date has been carried out at 1.5T. One issue affecting BURST at high fields is related to RF power requirements for excitation. BURST saturates spins over a wide bandwidth, which pushes up both the total power and the peak power. These are critical factors at higher fields, and hardware and SAR constraints can limit the flip angle that can be used.

3.7.5 BURST variations

The original description of BURST [30] was of a train of pulses followed by a train of echoes, all acquired under a constant gradient. Later, the signal was refocussed by

use of 180° pulses to give spin echoes [31, 32] and by a pair of 90° pulses to give stimulated echoes [33], or by gradient reversals [34, 35]. The efficiency of the technique was greatly improved with the introduction of phase modulation [20-24] and frequency switching [35]. The latter work also used double gradient reversal, which results in echoes with equal T_2 weighting. The BASE variant [36] improved on the SNR by using a shorter RF train, which is then multiply-refocussed by use of successive 180° pulses. Volume imaging was performed with the gradient-refocussed URGEVI [37], and a multislice variant STEAM-BURST [33] used stimulated echoes to recall each slice of spins in turn. The latter work was carried out at 3T, whereas the other work was mainly carried out at 1.5T.

The intrinsic diffusion weighting of the BURST echoes has been explored [38, 39] and used in acquiring rapid diffusion weighted images [40]. fBURST is the name given to the functional imaging method carried out with asymmetric spin echoes [41], in which all echoes have equal T_2^* weighting. Other methods include radial BURST[42], in which the excitation gradient is rotated during excitation, and half-Fourier BURST [43], which showed an improvement in SNR under certain conditions.

3.8 References

1. Morris, P.G., *Nuclear Magnetic Resonance in Medicine and Biology*. 1990: Clarendon Press, Oxford.

2. Damadian, R., L. Minkoff, M. Goldsmith, et al., Science, 1976. 194: p. 1430.

3. Damadian, R., L. Minkoff, M. Goldsmith, et al., Physiol. Chem. Phys., 1976. 8: p. 61.

4. Hinshaw, W.S. in *Proc. Ampere Congr. 18th, Nottingham*. 1974.

5. Hinshaw, W.S., Phys. Lett., 1974. 48A: p. 87.

6. Maudsley, A.A., J. Magn. Reson., 1980. 41: p. 112.

7. Sutherland, R.J. and J.M.S. Hutchison, J. Phys. E.: Scient. Instrum., 1978. 11: p. 79.

8. Hounsfield, G.N., *Computerized axial transverse scanning (tomography).* Br. J. Radiol, 1973. 46: p. 1016-1022.

9. Lauterbur, P.C., Nature, Lond., 1973. 242: p. 190.

10. Mansfield, P. and P.K. Grannell, *'Diffraction' in Solids?* Journal of Chemical Physics, C, 1973. 6: p. L422.

11. Edelstein, W.A., J.M.S. Hutchison, G. Johnson, et al., Phys. Med. Biol., 1980. 25: p. 751.

12. Mansfield, P., *Multi-Planar Image Formation using NMR Spin Echoes.* Journal of Chemical Physics, C, 1977. 10: p. L55.

13. Mansfield, P. and I.L. Pykett, J. Magn. Reson., 1978. 29: p. 355.

14. Haase, A., J. Frahm, D. Matthaei, et al., *FLASH imaging. Rapid NMR imaging using low flip-angle pulses.* J. Magn. Reson., 1986. 67: p. 258-266.

15. Hennig, J., A. Nauerth and H. Friedburg, *RARE imaging: a fast imaging method for clinical MR.* Magn. Reson. Med., 1986. 3: p. 823-833.

16. Ahn, C.B., C.Y. Rew, J.H. Kim, et al. *A new high speed spiral scan echo-planar (SEPI) NMR imaging*. in *4th SMRM, London*. 1985.

17. Heid, O., M. Deimling and W. Huk, *QUEST - a quick echo split NMR imaging technique.* Magn. Reson. Med., 1993. 29: p. 280-283.

18. Hennig, J., *Echoes - How to generate, recognize, use or avoid them in MR-imaging sequences, part 1.* Concepts Magn. Reson., 1991. 3: p. 125-143.

19. Jerecic, R., M. Bock and L.R. Schad, *An amplitude optimized single-shot hybrid QUEST technique.* Magn. Reson. Imag., 2000. 18: p. 23-32.

20. Zha, L. and I.J. Lowe, *Optimised ultra-fast imaging sequence (OUFIS).* Magn. Reson. Med., 1995. 33: p. 377-395.

21. Cho, Z.H., Y.M. Ro and I.K. Hong, *FM DANTE fast imaging and variations: emerging rf-based ultrafast imaging techniques.* Concepts Magn. Reson., 1998. 10(1): p. 33-54.

22. Gelderen, P.v., J.H. Duyn and C.T.W. Moonen, *Analytical solution for phase modulation in BURST imaging with optimum sensitivity.* J. Magn. Reson. Series B, 1995. 107: p. 78-82.

23. Heid, O., *BURST excitation pulses.* Magn. Reson. Med., 1997. 38: p. 585-590.

24. Roux, P.L., J. Pauly and A. Macovski, *BURST excitation pulses.* in 'Proc., SMRM, 10th Annual Meeting', 1991: p. 269.

25. Freeman, R., in *Spin choreography: basic steps in high resolution NMR*. 1997, Oxford: Spektrum. p. 156-158.

26. Morris, G.A. and R. Freeman, *Selective excitation in Fourier transform nuclear magnetic resonance.* J. Magn. Reson., 1978. 29: p. 433-462.

27. Taniguchi, Y., H. Ochi and K. Okajima. *3D Burst microscopic imaging*. in *9th ISMRM*. 2001.

28. Mansfield, P. and A.A. Maudsley, *Planar spin imaging by NMR.* J. Magn. Reson., 1977. 27: p. 101-119.

29. Matsuda, T., M. Koromi, H. Inoue, et al., *Another interpretation of BURST imaging as a variation of line projection imaging.* Magn. Reson. Med., 1996. 36: p. 796-799.

30. Hennig, J. and M. Mueri, *Fast imaging using Burst excitation pulses.* in 'Proc., SMRM, 7th Annual Meeting', 1988: p. 238.

31. Hennig, J. and M. Hodapp, *Burst imaging.* MAGMA, 1993. 1: p. 39-48.

32. Lowe, I.J. and R.E. Wysong, *DANTE ultrafast imaging sequence (DUFIS).* J. Magn. Reson. Series B, 1993. 101: p. 106-109.

33. Cremillieux, Y., C.A. Wheeler-Kingshott, A. Briguet, et al., *STEAM-BURST: A single-shot, multi-slice imaging sequence without rapid gradient switching.* Magn. Reson. Med., 1997. 38: p. 645-652.

34. Heid, O., M. Deimling and W.J. Huk, *Ultra-rapid gradient echo imaging.* Magn. Reson. Med., 1995. 33: p. 143-149.

35. Duyn, J.H., P.v. Gelderen, G. Liu, et al., *Fast volume scanning with frequency shifted BURST MRI.* Magn. Reson. Med., 1994. 32: p. 429-432.

36. Gelderen, P.v., C.T.W. Moonen and J.H. Duyn, *Susceptibility insensitive single-shot MRI combining BURST and multiple spin echoes.* Magn. Reson. Med., 1995. 33: p. 439-442.

37. Heid, O. *Ultra rapid gradient echo planar / volumar imaging*. in *3rd SMRM*. 1995. Nice.

38. Doran, S.J. and M. Décorps, *A robust, single-shot method for measuring diffusion coefficients using the "BURST" sequence.* J. Magn. Reson. Ser. A, 1995. 117: p. 311-316.

39. Doran, S.J., P. Jakob and M. Décorps, *Rapid repetition of the "Burst" sequence: The role of diffusion and consequences for imaging.* Magn. Reson. Med., 1996. 35: p. 547-553.

40. Wheeler-Kingshott, C.A., D.L. Thomas, M.F. Lythgoe, et al., *Burst excitation for quantitative diffusion imaging with multiple b-values.* Magn. Reson. Med., 2000. 44(5): p. 737-745.

41. Jakob, P.M., G. Schlaug, M. Griswold, et al., *Functional BURST imaging.* Magn. Reson. Med., 1998. 40: p. 614-621.

42. Jakob, P.M., F. Kober and A. Haase, *Radial BURST imaging.* Magn. Reson. Med., 1996. 36: p. 557-561.

43. Jakob, P.M., M. Griswold, K.O. Lovblad, et al., *Half-Fourier BURST imaging on a clinical scanner.* Magn. Reson. Med., 1997. 38: p. 534-540.

4 Instrumentation & Control

A brief overview is presented of the layout and specification of the imaging system used for this work. Then the developmental work in implementing BURST on the system is outlined, followed by details of the processing and simulation software which has been written.

4.1 The imaging system

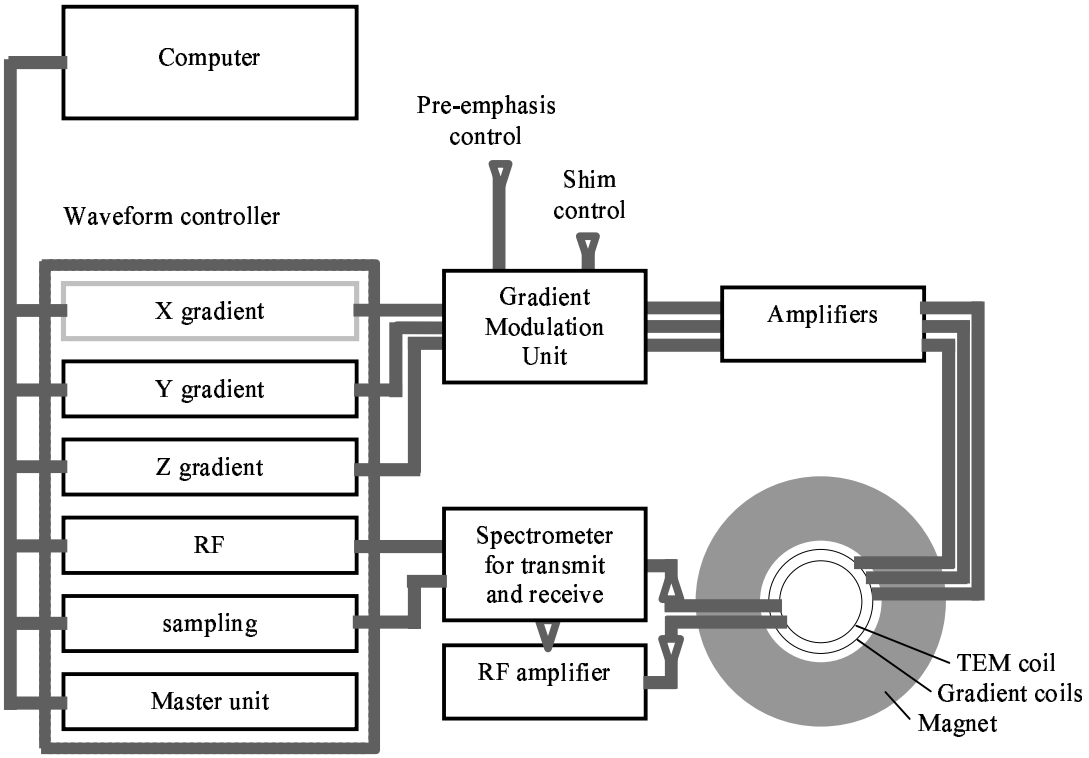

Figure 15 Structural overview of the relevant hardware of the Nottingham 3T system.

The 3T whole body EPI system in Nottingham [1] was used for all the experiments. It houses a superconductive magnet fitted with both passive shims and resistive shim coils. It has a homogeneity of 200ppm over a 30cm dsv without shimming, and of 10ppm over a 50cm dsv following shimming. The field is stable to 0.1 ppm per hour. It is used primarily for EPI. Home-built gradient coils are installed in the bore together with a 27cm diameter TEM coil, which provides quadrature transmission

and reception. The rest of the hardware sits outside the RF-screened room housing the magnet.

The computer provides overall control of the system. The sequence code is written in a combination of c and assembler macro instructions, which is then compiled into assembler code before being downloaded to the waveform controller. This consists of several independent processors which control and generate the gradient and RF waveforms (four processors for the gradients (one is spare), two for the RF, one for sampling and one master unit to provide overall control). A user interface on the computer allows for adjustment of sequence parameters in these modules after compilation. The modules can generate waveforms with a resolution of 1μs and the signal is sampled with a 1/16 μs resolution. The analogue outputs from the gradient modules are passed first to the GMU (Gradient Modulation Unit) which provides pre-emphasis correction. This adjusts the gradient profile to compensate for eddy currents which arise in the structures of the magnet. The output is then passed through a series of power amplifiers on its way to the gradient coils. The RF module output is fed to a 2 kW power amplifier and then onto the TEM coil.

4.2 BURST coding

The scanner had not been previously coded for BURST. The sequence has been implemented as shown in Figure 16 below. A slice-selective 180° pulse, sandwiched between two spoiler gradient lobes, is used to refocus the echoes. The phase encoding is achieved with a constant gradient during acquisition. The user interface provides full control over all amplitudes and timings (see Figure 17).

The basic BURST sequence implementation uses on/off rectangular pulses in the DANTE train. The durations and spacings of the pulses, as well as the gradient amplitudes, can all be altered at runtime. The conventional user interface has been altered to incorporate the BURST parameters.

The RF gating for the DANTE pulses is enabled at the start of the train and disabled at the end, rather than switched on and off for every pulse, as is normally the case. This otherwise would lead to problems when implementing longer pulses, such as the

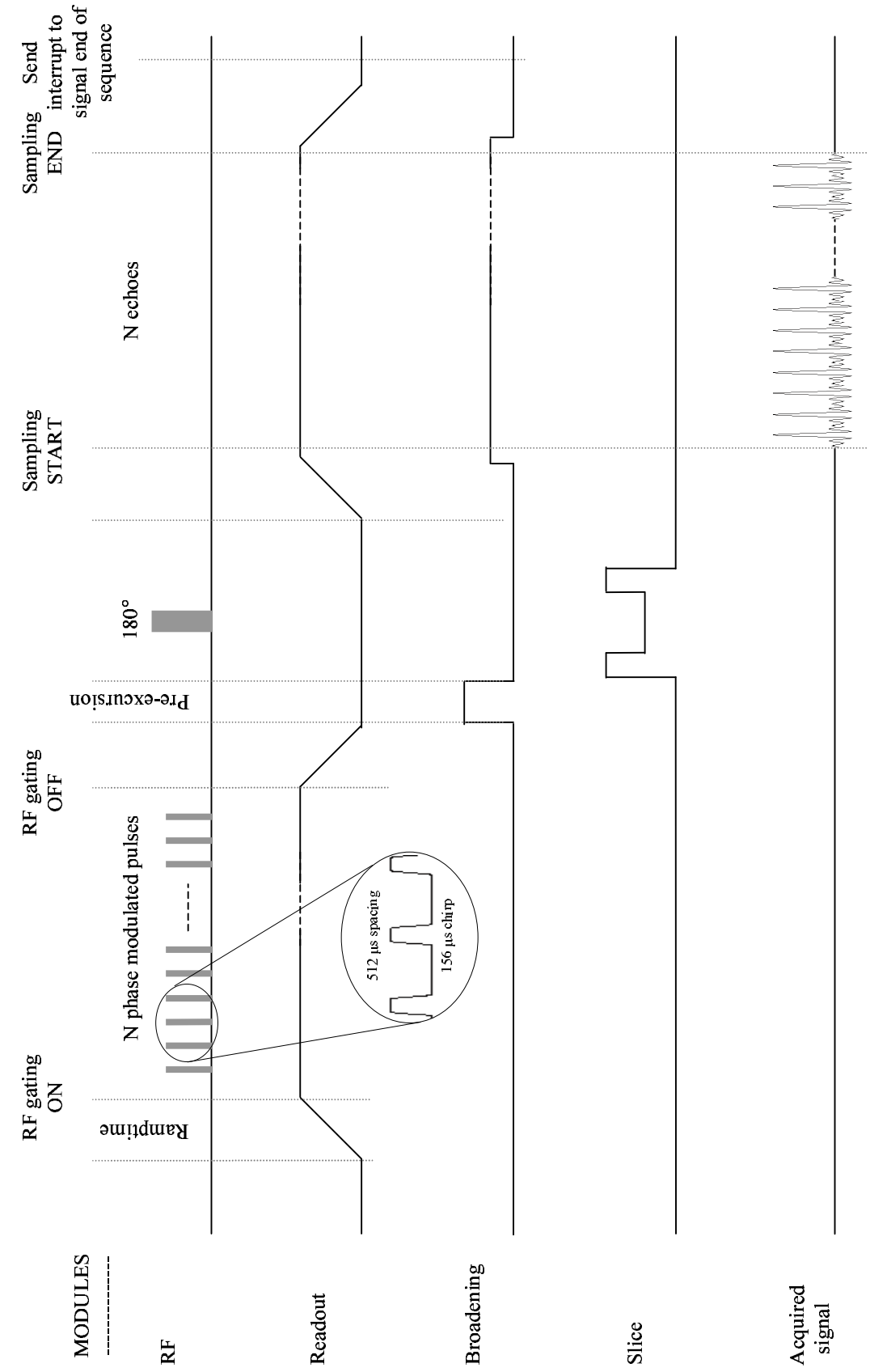

Figure 16 BURST sequence implemented on the 3T scanner. Typical DANTE parameters are indicated (the use of chirp pulses is explained in Chapter 7).

chirp pulses when the time between the pulses is short. The phase and amplitude data for the DANTE train is first written with 8-bit resolution to text files, which are read when the code is compiled. Several different modulation schemes at a time can be stored and each can be selected from the user interface.

One shortcoming of the system is the limited memory of the RF module. It is not possible to store 64 phase modulated pulses (such as chirp pulses). This is necessary if a different phase offset is required for each pulse. However, the multi-phase OUFIS phase modulation only requires eight different phase offsets in a 64 pulse train. This has been implemented by storing the basic set of eight pulses, and then redirecting between them as required. The order of the pulses is stored in a text file, which is read in when the code is compiled. The alternative to this would be to explicitly code for each pulse of the train, however this would be very cumbersome and inflexible. This method enables many, but not all, of the phase modulation techniques to be implemented. For instance, the FM-BURST technique [2] cannot be set up, since it uses a quadratic phase progression with 32 different phases of pulse.

Additional c macros have been written to handle the different RF requirements of the basic sequence and of the variations to the sequence described above.

An oscillatory gradient is required for the technique described in Chapter 6. For these experiments VERSE-transformed chirp pulses have been calculated for different sinusoidal gradient waveforms. A single period sinusoidal waveform has been written to file and is read in to the modules when the code is compiled. A train of gradient waveforms is applied in parallel with the train of RF pulses to give a long oscillatory gradient. The time constant of the gradient coil circuit was initially estimated, and then the amplitude of the oscillation was scaled up to take account of the reactance of the circuit. A further controllable time delay has been added to the sequence code to allow for compensation of any phase lag in the oscillatory gradient. In this implementation the interpulse spacing cannot be adjusted, since it is fixed by the period of the chosen oscillation.

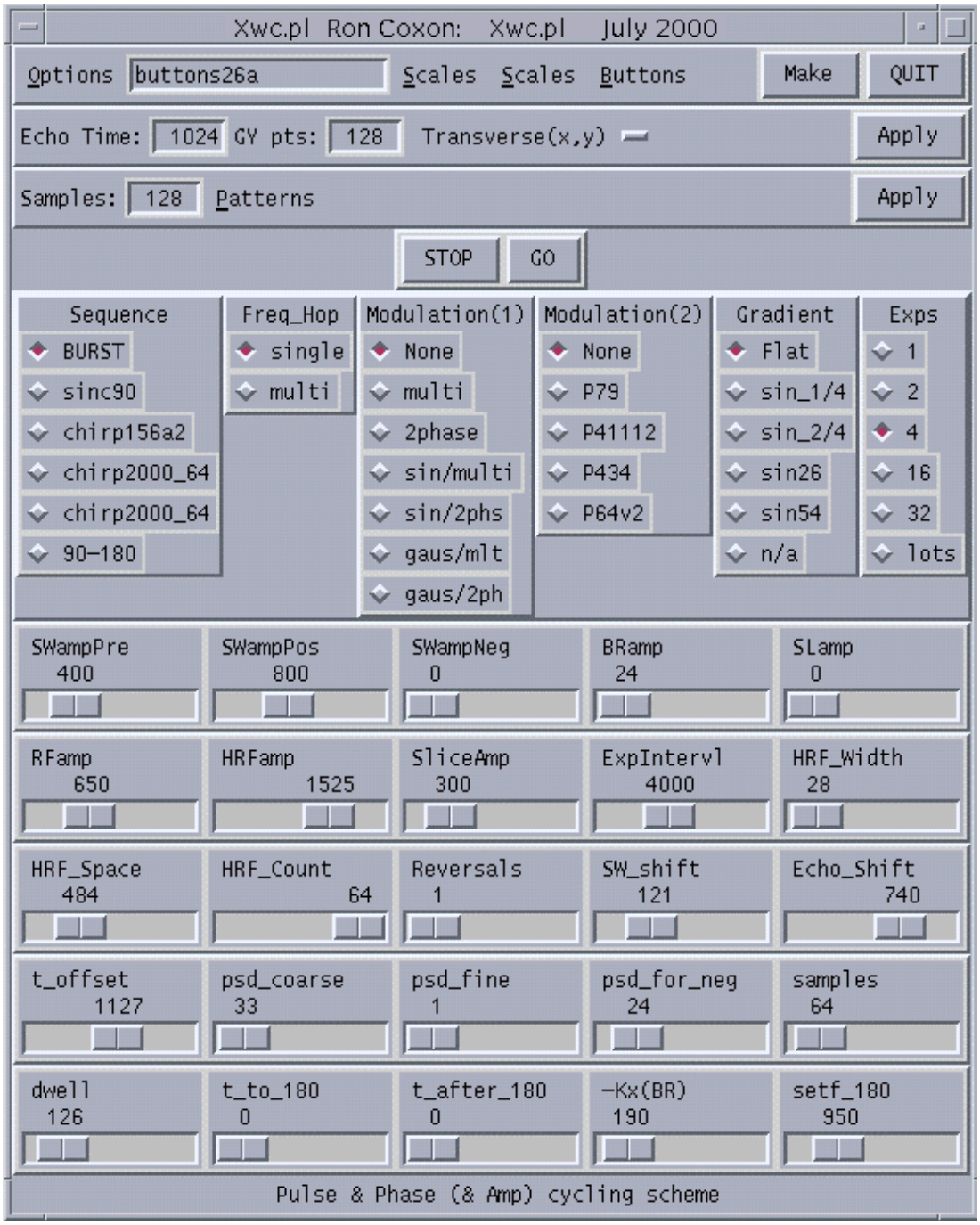

Figure 17 The user interface for controlling the BURST sequence

Further additions to the code have been made which allow for multiple gradient reversals to recall the echo train, for instance for 3DFT imaging, and which allow for additional gradient lobes to increase the diffusion sensitivity of the sequence.

4.3 Postprocessing

All the analysis of the data has been performed using the IDL application (*Interactive Data Language*, Research Systems, Boulder, Colorado). Once the echo train has been recorded the phase of each echo has to be corrected according to the phase of the generating pulse, otherwise severe artefacts will result. Programs have been written which read in the data and phase files, then firstly correct for DC offsets to the real and imaginary inputs and then correct the phases of the data. An additional option of using a separate data set to provide phase correction data (so-called 'navigator echoes' – see Chapter 6) has been incorporated in the code. In the same program the Fourier transform is performed to reconstruct the image. Further programs enable signal-to-noise calculations to be made for selected regions of interest.

4.4 Bloch Equation simulations

The effect of each of the different modifications to the BURST sequence are tested with a simulation of the Bloch Equations which has also been written using IDL. The simulation enables the calculation of the 1D response of spins of different frequencies and then the calculation of the echo train, with the option of including relaxation terms. It has been used extensively to test out different phase and amplitude modulations, different RF pulses and different gradient/RF combinations.

4.5 References

1. Glover, P.M., *High Field Magnetic Resonance Imaging*. 1993, Nottingham.

2. Cho, Z.H., Y.M. Ro and I.K. Hong, *FM DANTE fast imaging and variations: emerging rf-based ultrafast imaging techniques.* Concepts Magn. Reson., 1998. **10**(1): p. 33-54.

5 SNR and Resolution in BURST

5.1 Introduction

The signal amplitude in BURST is lower than that of other imaging sequences. Whereas in EPI the full magnetisation is refocussed for each echo, in BURST the magnetisation is split between the echoes. This division of magnetisation is an intrinsic quality of BURST and is a consequence of the multiple RF excitation at the heart of the technique. This results in a generally lower SNR, which is the most significant factor in the ultimate usefulness of the technique.

In addition, the attenuating effects of spin-spin relaxation and diffusion on the echo amplitudes further reduce the available signal. As with EPI, each echo is affected to a different degree; however, the exact form of the attenuation is a characteristic of the sequence itself. In the light of these factors the parameters of the sequence can be chosen to give the highest possible SNR.

5.2 Signal

In BURST the RF energy emitted by the precessing spins is distributed between all the acquired echoes. By contrast, EPI utilises all the instantaneous RF energy in each refocussed echo (as similarly does RARE). The amplitude of the echoes in BURST can be determined from one of two approaches: by considering the responses of the spins to the excitation, most simply with the linear approximation, and by considering the energy identity between the frequency and time (echo) domain (Parseval's Theorem).

In the previous chapter the linear approximation was used to describe the approximate response of the spins to a BURST excitation. In the next chapter the highly efficiency multi-phase OUFIS sequence will be shown to produce strips of excitation, with successive sub-trains exciting successive strips across each pixel. Then, according to the reciprocal Fourier relationship between the excitation and the subsequent echoes, this argument can be reversed: each strip results in a sub-train of echoes. Hence, each echo results from the refocussing of spins from only narrow

strips of the magnetisation, and this results in an inevitable reduction (compared to simultaneously refocussing all the magnetisation) in echo amplitude. This reduction is determined by the fractional width of the strips, which is given by $1/\sqrt{N}$, where N is the number of pulses in the excitation train. For instance, in a 64 pulse BURST excitation a signal 1/8 (=12.5%) that of the maximum possible is expected.

Alternatively, the same result can be obtained from an energy viewpoint. Consider the energy of a single echo resulting from the refocussing of all the spins (as in EPI). If that same energy (E_1) is distributed between N equal-amplitude echoes (each of energy E_i), then the amplitude of each echo (A_i) must scale down by a factor $\sqrt{N}$.

For N echoes,

$$E_1 \equiv NE_i$$

$$\Rightarrow \qquad A_1^2 \equiv NA_i^2,$$

where A_1 is the amplitude of the single echo resulting from the refocussing of all the spins.

Hence, $$A_1 \equiv \sqrt{N}A_i,$$

assuming that the echoes differ only in amplitude, and not in shape.

This analysis also assumes that the spins are excited equally well with both a single 90° pulse and a BURST excitation pulse, which in practice is the case when considering the optimised BURST sequences.

5.3 T_2 and Diffusion Attenuation

The signal is reduced by the dephasing of the spins and by the Brownian motion of the spins during the long gradient periods. Clearly, the later echoes will be more attenuated than the earlier ones, and this will limit the range of sequence parameters e.g. overall timing, which can be used before the attenuation is so great that the image deteriorates unacceptably.

For the conventional spin echo BURST experiment the diffusion attenuation can be modelled as for the PGSE sequence [1], assuming the linear approximation such that each pulse generates a coherence independently of the other pulses, as previously described by Doran and Décorps [2]. The effects of both the slice and phase encoding gradients are far less significant than that of the readout gradient, and so they are ignored in this calculation.

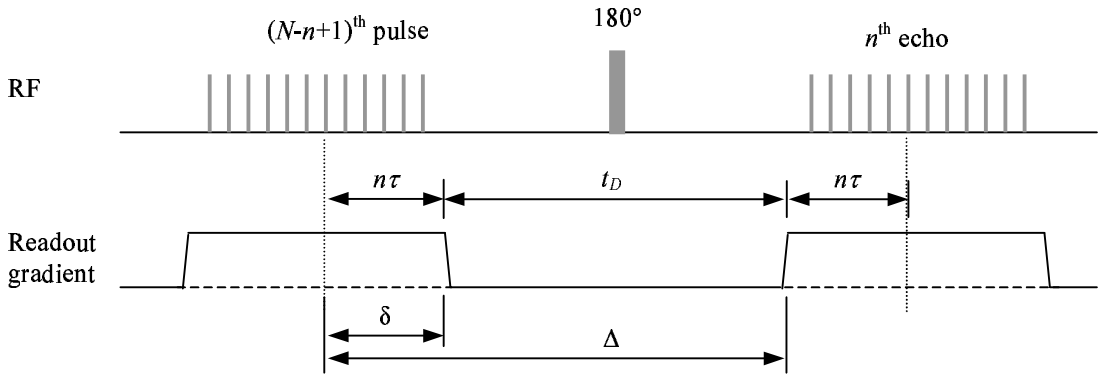

Figure 18 BURST pulse sequence indicating diffusion attenuation parameters

The Stejskal-Tanner parameters are related to the pulse timings as shown above.

The attenuated signal is given by

$$S_D = S_0 e^{-D\gamma^2 G^2 \delta^2 \left(\Delta - \frac{\delta}{3}\right)}, \tag{36}$$

where δ & Δ are the Stejskal-Tanner parameters, D is the self-diffusion coefficient, G is the readout gradient amplitude and S_0 is the amplitude of the signal in the absence of diffusion.

For the n^{th} echo

$$\Delta = n\tau + t_D \quad \text{and} \quad \delta = n\tau,$$

for an N pulse BURST sequence with pulse spacing τ. The pulse lengths and the rise and fall times of the gradients have been ignored here.

Hence,

$$S_D = S_0 e^{-D\gamma^2 G^2 (n\tau)^2 \left(\frac{2n\tau}{3} + t_D\right)}. \tag{37}$$

Additionally, the spatial resolution is given by

$$res = \frac{2\pi}{\gamma G \tau}. \tag{38}$$

Hence, for a fixed resolution expression (37) can be written as

$$S_D = S_0 e^{\frac{-4\pi^2 D n^2}{(res)^2}\left(\frac{2n\tau}{3} + t_D\right)}. \tag{39}$$

Using the same parameters, the T_2 attenuation is given by

$$S_{T_2} = S_0 e^{-\frac{t}{T_2}}$$

$$= S_0 e^{-\frac{2n\tau + t_D}{T_2}}. \tag{40}$$

The graph below shows the expected diffusion attenuation (black lines) and T_2 attenuation (blue lines) along the echo train for the brain (grey matter), with coefficients D ~ 0.8 x 10^{-9} m^2s^{-1}, assumed to be isotropic, and T_2 ~ 80 ms. Other parameters were: a resolution of 4mm, N=64 and t_D=7.7ms (as used in experiments). The pulse spacing, τ, is indicated next to each line.

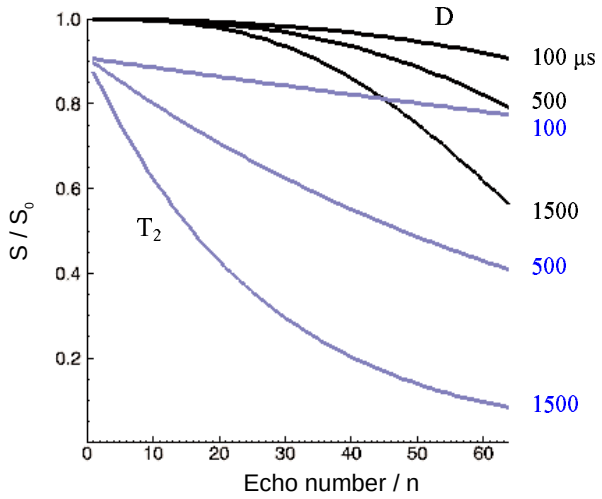

Figure 19 Diffusion (black) and T_2 (blue) attenuation for different pulse spacings.

For the parameters chosen here the T_2 attenuation is much greater than the diffusion attenuation, particularly for the earlier echoes. Therefore, single shot brain images will be predominantly T_2 weighted.

5.4 SNR and Resolution

One further step can be made which enables deductions to be made about the signal-to-noise. The amplitude of the central (k_0) echo can be used to give an estimate of the image signal. The earlier that this k_0 line can be encoded, the higher will be the echo amplitude and, by extension, the image signal too.

Hence, the image signal is given by

$$Signal \propto S_0 \, e^{\frac{-4\pi^2 D n_0^2}{(res)^2}\left(\frac{2n_0\tau}{3}+t_D\right)} e^{-\frac{2n_0\tau+t_D}{T_2}}, \tag{41}$$

where n_0 is the number of the echo encoded as k_0.

Additionally, the noise level is related to the acquisition bandwidth, which itself is related to τ, the spacing of the excitation pulses.

The noise is given by

$$noise \propto \sqrt{BW}\,. \tag{42}$$

Sampling each echo at N points, so that time between sample points is τ/N, the acquisition bandwidth is

$$BW = \frac{N}{\tau} \text{ Hz} \tag{43}$$

$$\Rightarrow \qquad noise \propto \frac{1}{\sqrt{\tau}}. \tag{44}$$

Hence, both the noise and the signal decrease with increasing τ.

Then, the SNR can be written

$$SNR \propto \frac{S}{noise} \propto S_0 \sqrt{\tau}\, e^{\frac{-4\pi^2 D n_0^2}{(res)^2}\left(\frac{2n_0\tau}{3}+t_D\right)} e^{-\frac{2n_0\tau+t_D}{T_2}} . \qquad (45)$$

As $\tau \to 0$, $\sqrt{\tau} \to 0$ and the exponential $\to 1$; hence $SNR \to 0$.

For $\tau \to \infty$, consider the power series expansion for the exponential, written as the reciprocal of a positive exponential,

$$SNR \propto \frac{\sqrt{\tau}}{1+x+x^2/2!+\cdots}$$, where x is a positive linear function of τ.

For large τ the higher power terms in the denominator dominate, and hence as $\tau \to \infty$, $SNR \to 0$. Between these limits the SNR will reach a maximum.

The SNR is plotted as a function of τ for two different n_0 values (=16,32) and for different resolutions (=2,4,10 mm). It should be noted that this calculation only considers attenuation and does not account for the differences in pixel volumes, and hence in the number of contributing spins, for different resolutions. Therefore, the graph below does not enable direct comparisons to be made between different resolutions, except in the positions of the maxima, since the curves only differ by an omitted resolution-related scaling factor.

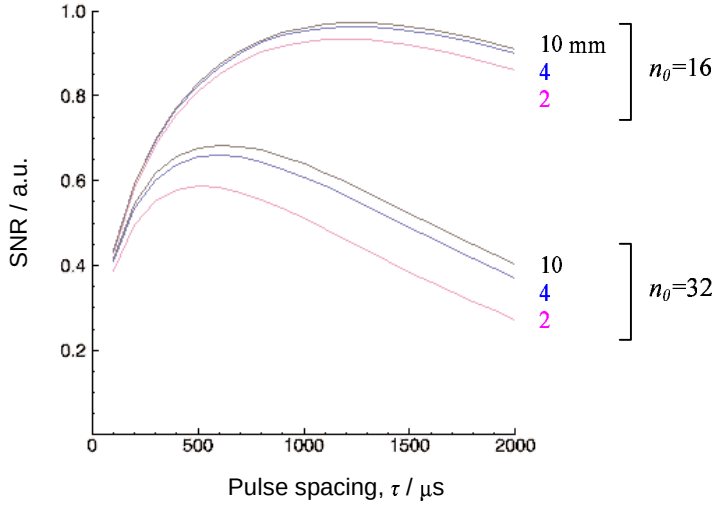

Figure 20 SNR (Equation(45)) as a function of τ for different resolutions and for different k_0 positions.

There is an interesting dependence of the maxima on τ. The SNR peak for 4mm occurs at $\tau \sim 600$ μs for $n_0 = 32$, and at $\tau \sim 1200$ μs for $n_0 = 16$. If the echo time TE is defined as the time between the $(N\text{-}n_0\text{+}1)^{th}$ pulse and the n_0^{th} echo i.e. $TE = 2n_0\tau + t_D$, it can be seen that this is the same in both these cases and, therefore, the T_2 attenuation is also. This suggests that the T_2 of the object alone determines the optimum TE, and thereby τ also. Figure 19 (on p.45) shows that diffusion contributes far less to the attenuation than T_2 relaxation: for n less than 32 the attenuation is very small and for high n the attenuation only increases significantly for longer pulses spacing (> 500 μs). Within these limits a good approximation for the SNR can be made by considering T_2 attenuation alone,

$$SNR \propto \sqrt{\tau}\, e^{-\frac{2n_0\tau + t_D}{T_2}}. \tag{46}$$

Then, differentiating this expression and setting it equal to zero shows that the maximum SNR occurs at

$$\tau = \frac{T_2}{4n_0}, \tag{47}$$

or, substituting for TE,

$$TE = 2n_0\tau + t_D = \frac{T_2}{2} + t_D. \tag{48}$$

Hence, the SNR maximum occurs at a fixed TE, independent of both n_0 and τ. For T_2=80ms, TE =48 ms (with t_D = 8 ms, as in experiments). For other tissues in the human body T_2 is shorter leading to more rapid signal attenuation and shorter TE times. At higher resolutions (< 4mm) the diffusion attenuation will be more significant (see Equation (39)); however, Figure 20 shows that this will lead only to a small shift (of ~100μs) in the position of the SNR maximum.

Figure 20 also shows the greater SNR that is obtained with smaller values of n_0. However, choosing to encode k_0 earlier on in the echo train will produce a more asymmetric sampling of k-space along the phase encoding direction. This can result in a decrease in the image signal and in the appearance of artefacts in the image. Additionally, this calculation relies on the simplifying assumption that the image signal can be predicted from the amplitude of the k_0 line. The above analysis

suggests that the SNR obtained with a small n_0 is maximised for a constant TE, and hence for a long τ, yet this would result in longer pulse and echo trains overall, with a correspondingly greater attenuation of the outlying echoes. This will lead to blurring in the phase encoding direction. A further point of note is that the overall duration of the sequence, including both excitation and acquisition, will be increased. Therefore, a practical working limit for n_0 has to be found. In general, for the data presented in this thesis k_0 was encoded one quarter of the way along the echo train i.e. n_0=16 for a 64 pulse train.

In conclusion, the SNR is indeed higher if the k_0 line is encoded early in the echo train. However, the gain is more than expected from attenuation considerations alone. A greater SNR gain can be made by reducing the noise (increasing τ) than by reducing the T_2 attenuation (keeping τ constant). There is further benefit to be gained from choosing to encode k_0 early on: the reduced bandwidth lowers the power deposition, an important factor in BURST and, furthermore, the lower gradient results in a lower RF peak power, another major issue in high field BURST imaging.

5.5 References

1. Stejskal, E.O. and J.E. Tanner, *Spin diffusion measurements: spin echoes in the presence of a time-dependent field gradient.* J. Chem. Phys., 1965. **42**: p. 288-292.

2. Doran, S.J. and M. Décorps, *A robust, single-shot method for measuring diffusion coefficients using the "BURST" sequence.* J. Magn. Reson. Ser. A, 1995. **117**: p. 311-316.

6 Phase and Amplitude Modulation of the RF Pulse Train

6.1 Introduction

The simple BURST excitation, with constant phase RF pulses, excites only a small fraction of the total magnetisation and results in images of comparatively low SNR. Subsequent developments of the BURST sequence introduced a varying phase along the pulse train, which led to a near complete excitation and hence a greatly improved SNR.

In 1991 Le Roux and Macovski [1] first demonstrated the possible improvements with phase modulation. Later, Zha and Lowe gave a broader description of the methods of phase modulation [2], and similar techniques have been developed by van Gelderen et al. [3] and by Cho et al. [4]. As a result, phase modulated BURST pulses can excite nearly all the magnetisation.

In the first BURST publication [5] it was suggested that amplitude modulation of the pulse train could be used to produce a more uniform echo train, thereby reducing the effects of T_2 and diffusion and of higher order echoes. The phase modulation schemes later developed also aimed to produce uniform echo trains. However, there may be advantages to having echo trains which are not uniform; redistributing the limited available signal can lead to differential weighting of k space lines, and hence affect SNR and resolution.

In this chapter some simple amplitude modulations are examined together with alternative phase modulations. Then, it is shown that an extension of the work of Zha and Lowe [2] leads to a method which gives greater control over the echo amplitudes and enables the design of alternative phase and amplitude modulations in BURST.

6.2 Theory and Methods

6.2.1 Previous developments

The original BURST sequence (with constant phase RF pulses), broadly speaking only excites spins on resonance and at harmonic sideband frequencies. Fourier analysis can be used to demonstrate this effect and also to show that the fraction of magnetisation excited is $\sim 1/N$, where N is the number of RF pulses in the train. Ultimately, low amplitude echoes are formed which lead to images of low SNR. However, phase modulation of the pulses changes this [6] - spins across the full frequency bandwidth can be excited.

Current phase modulation techniques are able to excite nearly all the magnetisation across the excitation bandwidth and to produce a highly uniform train of echoes. The Shinnar-Le Roux spinor formalism [7] has been used, first by Le Roux et al. and later, more comprehensively, by Heid [8], to develop very efficient phase modulations. The multi-phase OUFIS technique [2] was developed using Fourier analysis; another technique, frequency-shifted BURST [9], is based on the same principle; a different analytical approach has been used by van Gelderen et al. [3]; and the FM-DANTE technique [4] introduces a frequency modulated envelope, which has a well-understood frequency response. For each of these techniques a constant amplitude RF train is used, and a highly uniform amplitude echo train results, T_2 and diffusion attenuation aside. This leads to a theoretical $\sqrt{N}$ improvement in SNR over single phase BURST.

In their original abstract Hennig and Mueri [5] suggested that amplitude modulation of the pulse train could be used to produce a uniform amplitude echo train, taking into account the contributions of the different coherences, and possibly T_2 and diffusion effects also, using techniques based on the extended phase graph algorithm [10]. In the image domain this would result in a narrow and undistorted point spread function in the phase encoding direction. However, this technique involves dense calculations; also, it is an interesting question whether the gains to be made from correcting for all attenuation are worth the loss in SNR: any increase in amplitude in one echo must be met by a decrease in amplitude elsewhere. Also, echoes resulting from the superposition of several higher order echoes will have a more complicated

T_2 and diffusion weighting, which in turn will lead to images with more complicated contrast. Nonetheless, a technique which gives control over the amplitudes of the echoes would give an additional degree of freedom to the design of BURST sequences.

The work in this chapter seeks to develop control of the echo amplitude envelope and, hence, the most efficient use of the magnetisation. In the next section three variations to the BURST excitation are examined: simple amplitude modulations, alternative phase modulations and an extension of the method of Zha & Lowe [2] to produce combined amplitude and phase modulation schemes.

6.2.2 Alternative methods

6.2.2.1 Amplitude modulation

The first investigation of amplitude modulation was made without precise planning of the modulation. The amplitude envelope of the pulse train was modulated and combined with existing phase modulation schemes in a spin echo BURST sequence. At low flip angles, ignoring T_2 and diffusion, it would be expected that the amplitudes of the resulting echoes will reflect the amplitudes of the pulses. And, therefore, since each echo encodes successive lines in k space, this pulse amplitude modulation directly corresponds to the k space profile in the phase encoding direction and, hence, ultimately determines the resolution kernel in the image domain. On this basis different amplitude modulations were chosen which would give suitable resolution kernels.

At higher flip angles, where the linear approximation fails, this simple relationship does not hold. Indeed, it would be expected that these amplitude modulated pulses would have a poorer performance (as measured by the excitation efficiency) than constant amplitude trains, for which the existing phase modulations were designed. For instance, a simple explanation of the chirp-based phase modulations [1-4, 8] is that the spins are excited in a linear sweep across each pixel, as the effective frequency is incremented through the pulse train (see Section 7.2.1 for a fuller explanation). Now, if amplitude modulation is incorporated also, it will result in

regions of over- and under-nutation within each pixel. Hence, the magnetisation will not be excited as fully and the echo amplitudes will most likely deviate from their expected profile. Nonetheless, it is not clear how the sequence will perform, and in order to find out how much and in what ways the sequence has changed, whether for better or for worse, it is necessary to analyse the response of the spins.

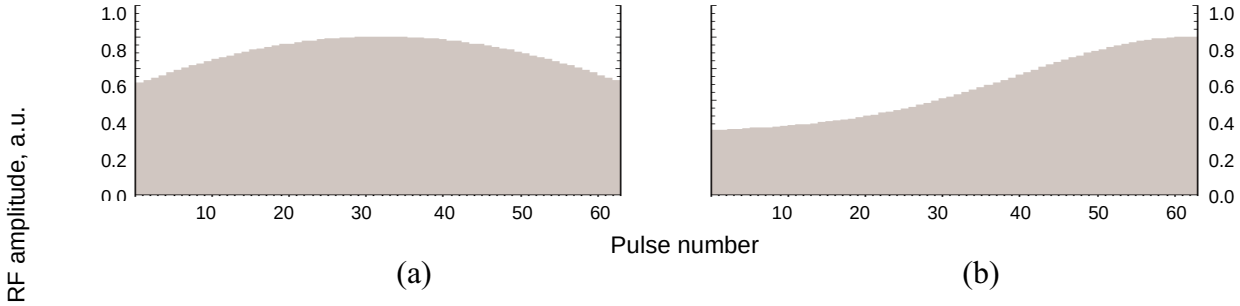

Figure 21 RF amplitude envelopes, (a) sinusoidal and (b) gaussian.

Simulations were performed to assess the different amplitude modulations and compare them to the current optimised phase modulation schemes.

6.2.2.2 Phase modulation

In another set of experiments alternative phase modulation schemes were implemented, this time in combination with uniform amplitude pulses. The existing optimised phase modulation schemes have an excellent performance, however it is interesting to observe how some different phase schemes perform. Can a random phase modulation of the pulses lead to an efficient excitation? And, following on from the linear and quadratic phases of OUFIS [2] and other methods [3, 4, 8], can a geometric progression of phase make efficient utilisation of the spins?

6.2.2.3 Combined amplitude and phase modulation

The challenge of developing an efficient amplitude modulated pulse train, which can give a useful and easily controllable modulation of the echoes, can be a lengthy numerical problem, as stated above (Section 6.2.1). The amplitude modulation above (Section 6.2.2.1) provides some scope for achieving this; however, greater control over the echoes can be obtained by examining the OUFIS technique [2]. Whilst amplitude modulation was not their goal, Zha & Lowe's technique gives a degree of

control over the echo amplitudes. A simple extension of this method allows the pulse amplitudes, and hence the echo envelope, to vary, thereby adding a new degree of freedom to the design of efficient pulse trains. The theory and its extension are described below.

The OUFIS approach

In the linear approximation the response of the magnetisation can be estimated from the Fourier transform of the RF function. For low flip angles this can very accurately determine the system response; for higher angles it becomes less accurate. The Fourier transform of a periodic train of RF pulses results in another periodic function, as shown below.

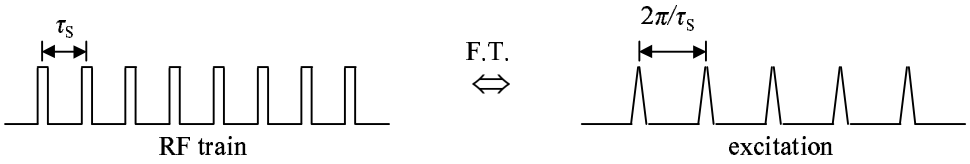

Figure 22 A schematic of a periodic train of RF pulses and its Fourier transform.

As described in Chapter 3, the pulse train can be most conveniently represented mathematically as an infinite train of periodically displaced δ functions, multiplied by a top hat function (to truncate the train to the required number of pulses), and then convolved with an individual pulse profile.

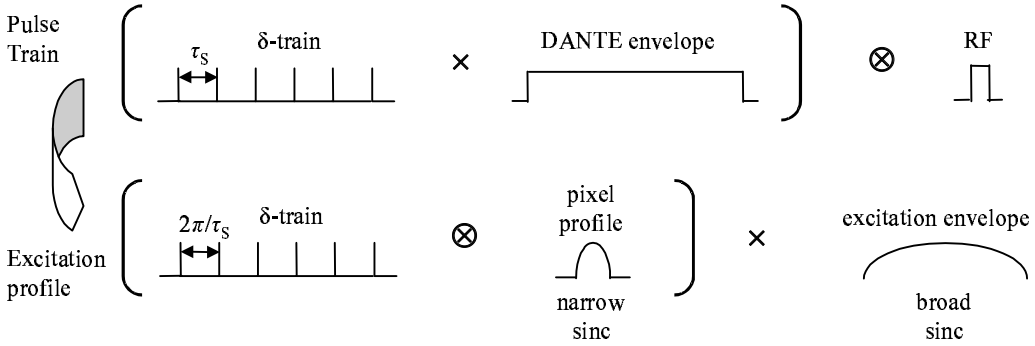

Figure 23 The DANTE pulse train and its Fourier transform

In BURST the period of the δ-train in the excitation profile corresponds to a single pixel's width. The strips of excitation each have a fractional width of ~1/*N* (of one

pixel), for a train of *N* pulses. Hence, in BURST (with constant phase) a 64 pulse train leads to the excitation of ~1/64 of the magnetisation and ultimately to low signal amplitudes.

The first observation to be made is that if the pulse train is shifted in frequency (by $\Delta\omega$), the excitation pattern will be displaced by an amount equal to this shift. This can be described in terms of a Fourier transform,

$$BURST \times e^{i\Delta\omega t} \overset{F.T.}{\Rightarrow} \delta(\omega - \Delta\omega) \otimes \hat{F}(BURST) \tag{49}$$

where $\hat{F}$ is the Fourier transform of the BURST excitation.

Hence, on successive applications of the BURST sequence different strips of spins can be excited, thereby removing the usual constraint on TR. This is the basis of the FS-BURST technique [9]. Alternatively, the same principle can be used to excite all the spins with a single BURST excitation. If the pulse train is divided into sections, each separately a short train of pulses, then the frequency can be stepped up between these successive sections. In this way different regions of spins will be excited by different sections of the pulse train, and with suitable choice of parameters a near-complete excitation can result. Zha & Lowe [2] instead introduced a linear phase progression, almost identical to a frequency shift, into each section, with the phase increment stepped up from one section to the next. Overall this results in an approximately quadratic phase roll over the whole pulse train. This method resulted in their multi-phase OUFIS phase schemes. A variation to this technique is FM-BURST [4], in which an exactly quadratic phase roll is applied. This is equivalent to stepping up the frequency between pulses, rather than between sections of the pulse train (see further discussion in next chapter).

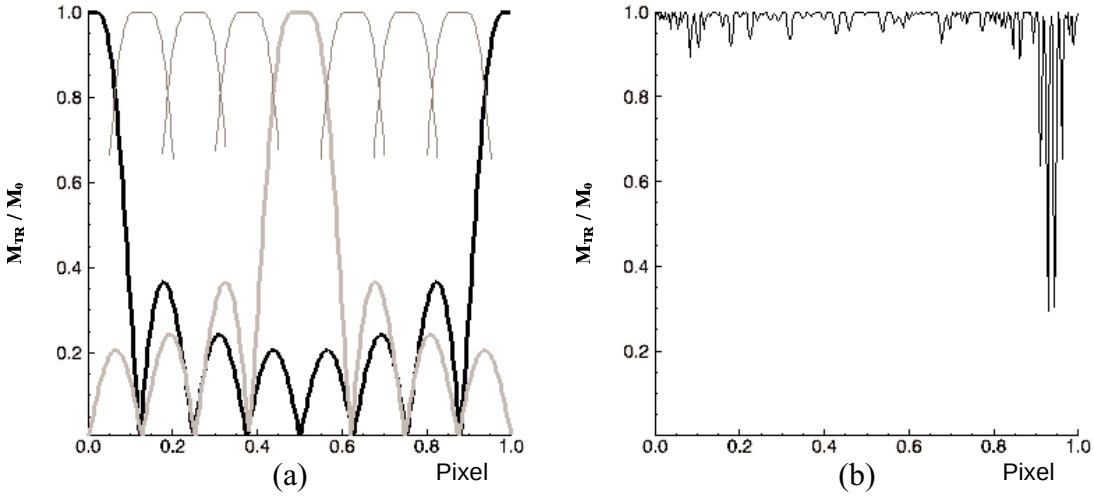

Figure 24 (a) Strips of excitation in a single pixel produced by each sub-train alone in 64 pulse, multi-phase OUFIS. The first and the fourth excitation profiles are shown in full, and the peak of the central lobe is shown for the others. (b) The full simulated excitation for the complete pulse train is shown.

Generalisation to an amplitude modulated pulse train

In general, an n pulse train will excite strips $1/n$ pixels wide and has an optimum flip angle $\pi/2n$. Its frequency response can be arbitrarily shifted by appropriate phase modulation. By piecing together pulse trains of different lengths amplitude modulation (varying the flip angle) can become an integral part of the design of the pulse train. The number of pulse trains and their phase modulations can be chosen so that a near-complete excitation results.

The constraints on the division of the entire pulse train into sections are described by,

$$\sum_{i=1}^{m} \frac{1}{n_i} \sim 1 \qquad \text{Sum of strip widths} \sim 1 \text{ pixel} \qquad (50)$$

$$\sum_{i=1}^{m} n_i = 64 \qquad \text{Total number of pulses in the excitation.} \qquad (51)$$

Subject to these constraints new pulse trains can be formulated which have an integral variation in amplitude along their length.

In multi-phase OUFIS, m=8 and n_i =8 for all i. In this case the first constraint is satisfied exactly, $\Sigma 1/n_i = 1$. In general, if a train of pulses is to be optimised to give a train of equal amplitude echoes, then it must be divided into sections of equal length

to excite strips of equal width. If a train of N pulses is divided into m sections each of n pulses, then from Equation (50) m/n=1, and from Equation (51) $m \times n = N$. Therefore, $m = n = \sqrt{N}$; the fractional width of each strip is $1/\sqrt{N}$, greater than for a constant phase train by a factor of $\sqrt{N}$. More generally, with sections of varying length, Equation (50) can only be approximately satisfied, but with careful choice of n_i this would lead to little, if any, loss in excitation efficiency.

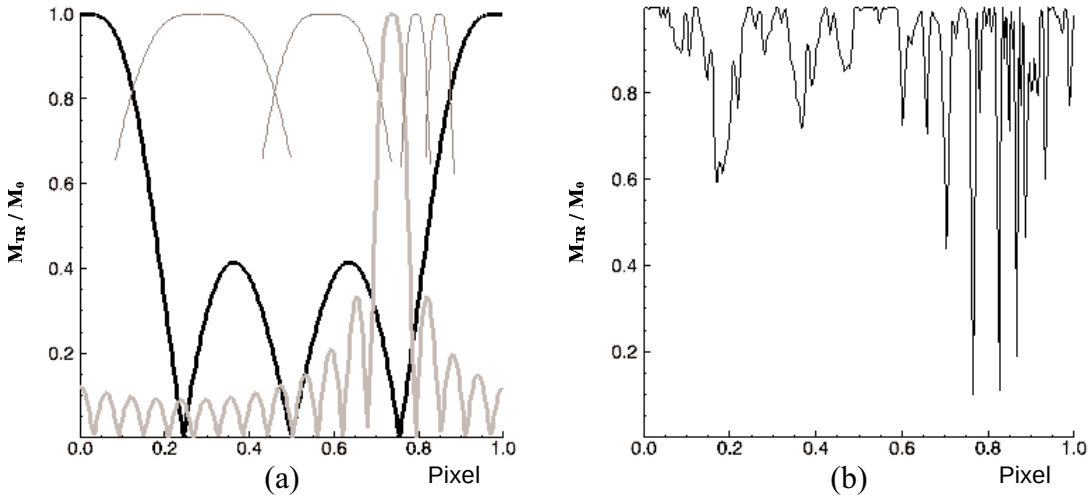

Figure 25 (a) Strips of excitation in a single pixel produced by each sub-train alone in the sequence (4,3,4,17,18,18). Two excitation profiles are shown in full, and the peak of the central lobe is shown for the others. (b) The full simulated excitation for the complete pulse train is shown.

In designing the pulse train a choice of an initial target envelope can be made. Then, through a trial and error approach the pulse train can be divided into sections, such that the flip angles (amplitude envelope) provide a discrete approximation to the target profile. In practice, only a very rough approximation can be made to a smoothly varying envelope. Also, as a guide an amplitude modulated pulse train should be divided into fewer sections than the corresponding constant amplitude pulse train (i.e. $m<\sqrt{N}$), otherwise overuse of magnetisation results ($\Sigma 1/n_i > 1$).

Below are shown the amplitudes of pulse trains produced with this technique. Figure 26 (a) & (d) show pulse trains with simple two-level amplitude modulations, the first showing only a small step in amplitude, and the second a more extreme stepping. The other two pulse trains, in Figure 26 (b) & (c), roughly mimic smoothly peaked modulations with multiply stepped amplitudes. In an experiment the peak amplitude

echoes would be used to encode the central k space lines. The sub-trains within each 64 pulse train can be switched around so as to allow the peak echoes to be shifted along the train.

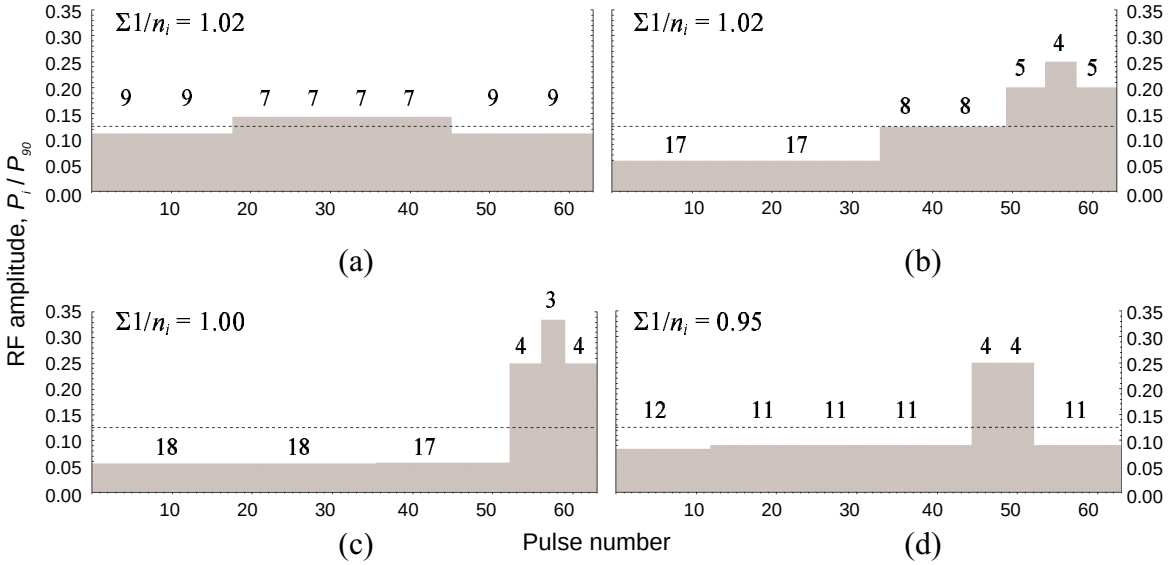

Figure 26 RF amplitude envelopes (shaded regions) produced with this technique; n_i = (9,9,7,7,7,7,9,9)[(a)], (17,17,8,8,5,4,5)[(b)], (18,18,17,4,3,4)[(c)], (12,11,11,11,4,4,11)[(d)]. Dashed lines show amplitudes of pulses in the OUFIS sequence. Amplitudes are given relative to that of a single pulse of 90° flip angle.

6.3 Results

The above techniques were used to develop sequences, each of which were evaluated using a number of figures of merit.

i) From the echo train a figure for the echo efficiency was found.

ii) The profile of the echoes was compared with that of the pulses to assess the techniques for controlling the amplitude envelope.

iii) Finally, the effect of any modulation on the final image resolution and signal was determined.

These performance measures were obtained initially from simulations of the Bloch Equations, and then compared with measures obtained from imaging experiments.

i) Echo efficiency

Previously Zha & Lowe assessed their modulation schemes using an efficiency measure given by

$$\eta = \sqrt{\sum_{i=1}^{m} \left(A_i^{norm}\right)^2} \times 100\% \qquad (52)$$

where A_i^{norm} is the amplitude of the i^{th} echo, normalised to the echo from a single 90° pulse of the same bandwidth.

This same figure of merit was used to evaluate modulation schemes in this work. However, their paper [2] does not give details of all the simulation parameters, and so firstly a suitable set of values had to be chosen. Typical BURST parameters of 8μs hard pulses and an interpulse spacing of 512μs were chosen. The simulations were performed over an offset frequency bandwidth of 125kHz, corresponding to a 64-pixel-wide field of view. The amplitudes of the echoes were each normalised to the peak echo amplitude obtained from a single 8μs pulse, with an on-resonance flip angle of 90°. The effects of T_2 and diffusion were not included. It was found that these parameters gave very similar, though not identical, figures for the efficiency, when comparisons were made with the results of Zha & Lowe. The discrepancy was less than 1%.

The efficiency is related to the energy of the echoes (proportional to $(A_i^{norm})^2$). For BURST simulations the RF amplitude was chosen in two ways: for the amplitude modulations the RF amplitude was varied to find the maximum possible efficiency that could be obtained (θ_{MAX}), whereas for the combined modulations the flip angles were calculated using the simplifying assumptions of the linear approximation to give saturation of each of the excited strips (θ_{FULL}). For the purposes of making comparisons with previous work both these methods were used to find the RF amplitude for the OUFIS phase modulation sequences.

For each modulation the analysis was repeated for excitation at a reduced flip angle, as done by Zha & Lowe. The deviation from the echo profile from the primary echo amplitude envelope can be attributed to higher order echoes, formed by the

interaction of the individual pulses of the pulse train. The contribution from these echoes will fall off more rapidly than the primary echoes as the flip angle is reduced. The flip angle was reduced by a factor of √2, the same as was chosen by Zha & Lowe.

ii) Amplitude modulation

Each different amplitude modulation of the pulse train led to a different amplitude modulation of the echo train. The closeness of the two profiles – of the pulse train and of the echo train – was an important quantity to assess. This reflected the success of the proposed techniques for controlling the echo amplitudes. To do this, firstly one profile was reversed, and then a least squares fit was performed to scale one profile to the other. The closeness of match (E) was measured by the square root of the least squares minimum value, and these values were normalised to the result for the well-established multi-phase OUFIS modulation with a 90° net flip angle,

$$\mathrm{E} \equiv \frac{\sqrt{\sum_{i=1}^{N} \left(A_i - P_{N-i}\right)^2}}{\sqrt{\sum_{i=1}^{N} \left(A_i^{OUFIS} - P_{N-i}^{OUFIS}\right)^2}} \tag{53}$$

where A_i is the amplitude of the i^{th} echo and P_{N-i} is the amplitude of the $(N-i)^{th}$ pulse, scaled one to the other, as described above. The expression in the denominator normalises the result to the OUFIS modulation.

An important requirement for any new modulation is that it produces an echo train of high efficiency, comparable to the established modulation schemes. The multi-phase OUFIS modulation scheme produces efficiencies of 97.6% at full (calculated) flip angle, falling to 84.0% for the 'reduced' flip angle.

*Simulation*μ**amplitude modulation, with existing phase modulations**

Amplitude modulation	Phase (OUFIS)	η (η_R) / %	E (E_R)
Constant	multi-phase	99.5 (91.4)	1.34 (0.68)
	2-phase	95.7 (88.1)	3.13 (1.42)
Sinusoidal	multi-phase	99.2 (91.1)	1.56 (0.71)
	2-phase	95.7 (88.2)	3.35 (1.52)
Gaussian	multi-phase	92.2 (86.4)	4.35 (2.03)
	2-phase	91.4 (84.6)	4.30 (1.90)

Table 1 Efficiencies and echo envelope deviations for the amplitude-only modulations. Bracketed figures show results for reduced flip angles.

Two alternative amplitude modulations, the sinusoidal (Figure 21(a), p.53) and the half-gaussian (Figure 21(b)), were examined in combination with multi-phase and two-phase OUFIS phase modulation schemes. These phase modulations were developed for use with constant amplitude pulse trains, and therefore the introduction of any amplitude modulation would be expected to produce strips of over- and under-nutation, and hence lead to a reduction in efficiency. The flip angle was varied to find the maximal value of the efficiency for each modulation, and compared with the maximal value obtained for the constant amplitude OUFIS modulation. The multi-phase OUFIS modulation resulted in a very high efficiency (99.5%), higher in fact than was found using a 90° flip angle (97.6%). The sinusoidal and gaussian modulations with maximal flip angles produced high excitation efficiencies of 99.2% and 92.2% respectively. This compares very well with the OUFIS efficiency and demonstrates that a modest degree of amplitude modulation need not be detrimental to the efficiency. With 'reduced' flip angles the efficiencies fell by ~7%, a noticeably smaller drop than is observed in the later results for the combined schemes (Table 3, p.64). This seems reasonable considering the different methods for choosing the flip angle in each case. For amplitude modulation alone the maximal efficiency was found, whereas for the combined schemes a 90° flip angle was chosen, which in general will lead to a less than maximal efficiency. As the maximum value is approached the efficiency value will plateau out, and hence there will be smaller variation in the efficiency in this region.

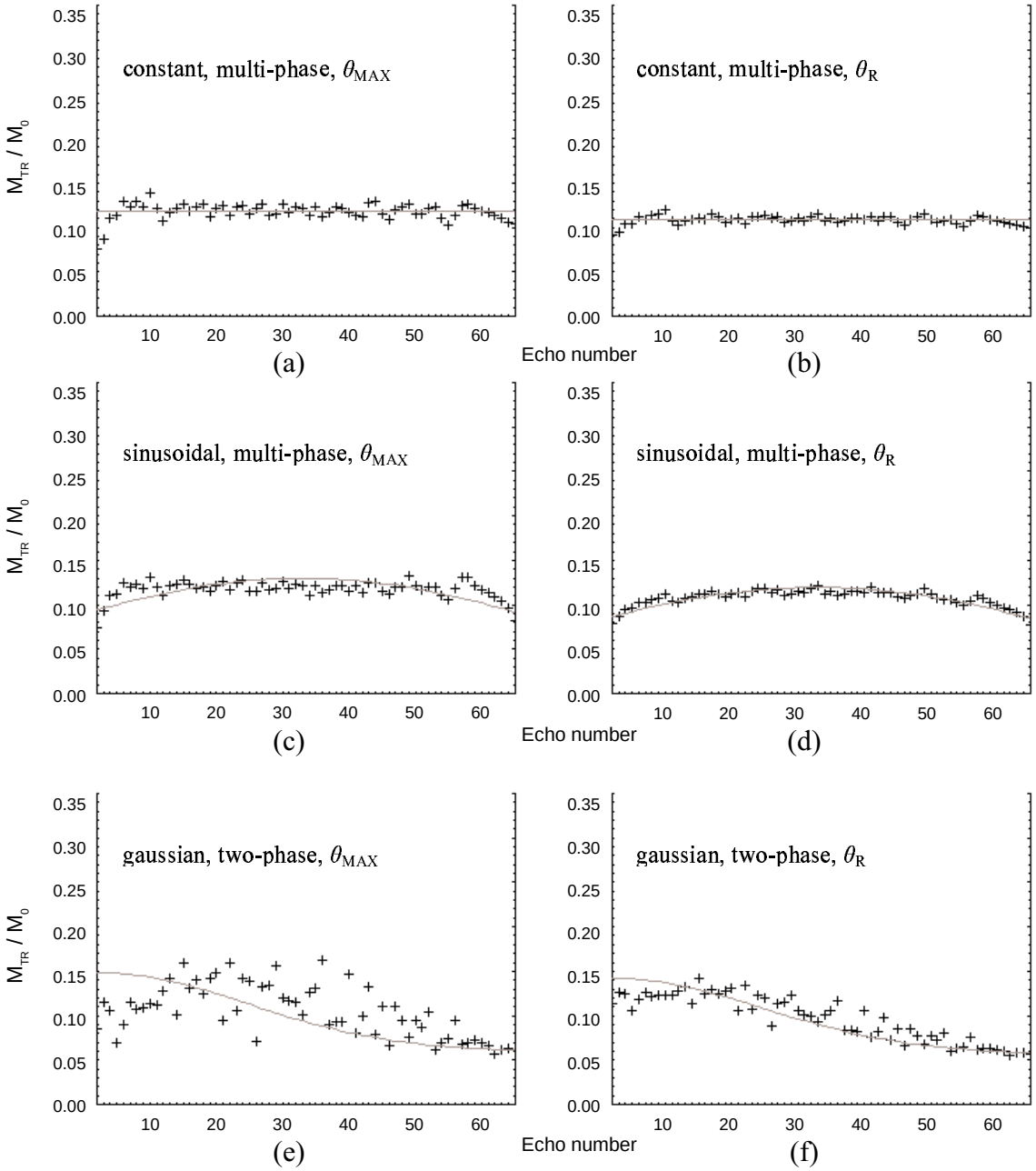

Figure 27 Simulated echo amplitudes (+) together with fitted lines showing expected profiles (grey lines). For each graph the label gives the amplitude modulation, the OUFIS phase modulation and the flip angle, whether optimised (θ_{MAX}) or reduced (θ_R).

While the results for the efficiencies were good, the results for the echo profiles were less promising. As can be seen in Table 1, three- and four-fold increases in this figure of merit were found. Figure 27 shows some of the expected echo amplitudes (proportional to the pulse amplitudes) fitted to the simulated echo amplitudes. Of these only the sinusoidal / multi-phase pairing with θ_R [(d)] shows a strong correlation with the expected data (E = 0.71); the other results [(c),(e) & (f)] show only little correlation (E > 1.0). These results suggest that this amplitude modulation

method can maintain the high utilisation of the magnetisation (high efficiency) of OUFIS, but in general leads to poorer correlations of the amplitude envelope, and hence less control over the echo amplitudes. The data presented here only covers a very limited set of amplitude modulations, however it does suggest that amplitude modulation alone provides only modest scope for controlling the echo train amplitudes.

***Simulation:* random & geometric phases**

Phase	η (η_R) / %	E (E_R)
multi-phase OUFIS	99.5 (91.4)	1.34 (0.68)
2-phase OUFIS	95.7 (88.1)	3.13 (1.42)
Random	80.1 (75.8) 76.6 (73.5)	4.56 (2.53) 4.14 (2.32)
geometric	49.2 (47.6)	5.31 (4.45)

Table 2 Efficiencies and echo envelope deviations for the random and geometric phase modulations

These schemes produced less promising results than the amplitude modulations. The efficiencies were significantly lower and the echo envelopes were less well fitted, particularly in the case of the geometric progression. Two different sets of random phase were generated (using the IDL function 'RANDOMU'). These both produced fair results for the efficiency, but this still fell short of that obtained for the OUFIS schemes. Notably, the fit of the echo amplitudes to the pulses was much worse than for any of the amplitude modulations in the previous section.

The geometric phase progression produced a 50% efficiency, worse than the random phase. This particular geometric progression used was chosen only to give a good spread of phases over 0-360° without excessive phase wrapping, so as not to lose the sense of the progression; there was no reason to believe it would perform well. In fact the phase increases very slowly over the first half of the pulse train, making it close to a constant or linear phase progression, and therefore more similar to the inefficient constant phase BURST. Also, the echoes resulting from these phase

schemes were very variable, poorly matched to the constant amplitude of the pulse train.

These modulations were not further investigated in experiments. As before, different parameters could be used to investigate a range of geometric progressions and hence to build a fuller picture of their performance. However, on the basis of these results this does not look to be a promising technique.

***Simulation:* combined amplitude and phase schemes**

Phase	η (η_R) / %	E (E_R)
multi-phase OUFIS	97.6 (84.0)	1.00 (0.47)
2-phase OUFIS	94.4 (82.5)	2.38 (1.03)
(9,9,7,7,7,9,9)	93.4 (82.1)	2.02 (0.97)
(12,11,11,11,4,4,11)	90.6 (79.2)	2.36 (1.08)
(18,18,17,4,3,4)	91.7 (80.8)	2.30 (1.13)
(17,17,8,8,5,4,5)	94.3 (82.7)	2.21 (0.94)

Table 3 Efficiencies and echo envelope deviations for the combined modulations. The phase schemes in the first column are defined in Figure 26 on p.58.

The combined phase and amplitude modulations performed well. The efficiencies were comparable with the best OUFIS efficiency: all were over 90%, compared with the 97.6% figure for multi-phase OUFIS. For these modulations the RF amplitude was chosen to give a 90° flip angle on resonance.

It is worth noting that previously the OUFIS sequences with fewer than 64 pulses were found to be less efficient ($\eta_{64} = 97.6\%$, whereas $\eta_{16} = 93.9\%$, see [2]). The new modulations, in effect, are made up of sections from these shorter pulse trains (exciting the greater part of the magnetisation) and sections from longer trains (exciting the lesser part of the magnetisation). For instance, the phase modulation (18,18,17,4,3,4) is composed of three short sections (4,3,4) which excite $^1/_4+^1/_3+^1/_4 = ^2/_3$ of the magnetisation, and three long sections (18,18,17) which excite the remainder. Hence, the low efficiency shown here ($\eta = 91.7\%$) is consistent with

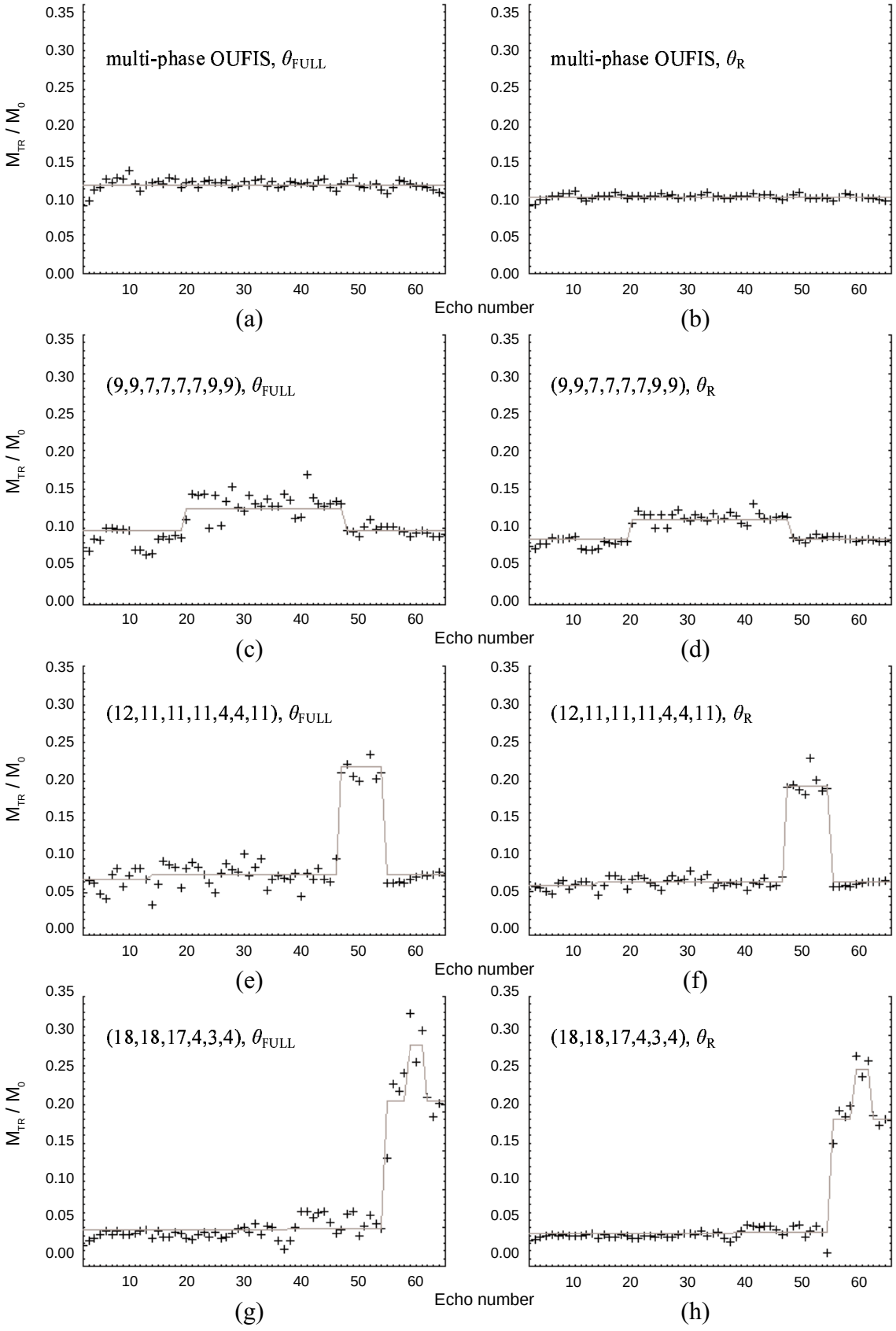

Figure 28 Simulated echo amplitudes (+) together with fitted lines showing expected profiles (grey lines).

these earlier results. It might be possible to improve on these efficiencies i) by varying the separation of the strips of excitation and ii) by changing the positions of the strips within each pixel i.e. rather than sequentially exciting the strips, do so in jumps.

The envelope profiles were a reasonably good match to the pulse profiles (E_R = 2.0-2.4), though not as good a match as obtained from multi-phase OUFIS (E_R = 1.0). As can be seen from the data plots above, the amplitudes broadly following the expected patterns, if with a fair bit of variability in places. However, reducing the flip angle by √2 reduced this variability markedly and produced much better fits ($E_R \sim 1.0$). These results show that this technique can produce high efficiency echo trains with profiles which match the expected profiles well.

iii) Resolution and SNR

The ultimate test of these techniques lies in the qualities of the images formed. These were assessed in simulations by estimating the expected changes in the signal and in the resolution (in the phase encoding direction). Later, experiments were carried out at 3T and the results compared. The image signal was estimated from the amplitude of the central k-space echo, which was assumed to be encoded a quarter of the way along the echo train for the amplitude modulations, and at the peak echo for the combined modulations. This was then normalised to the estimate for the multi-phase OUFIS sequence to give a value for the change in signal. The resolution estimate was obtained by calculating the Fourier transform of the echo train to obtain the resolution kernel and taking the FWHM value. Before calculating the Fourier transform the vector of 64 echo amplitudes was zero-filled to 1024 elements to provide finer discretisation of the resolution kernel.

Modulations (amplitude, phase)		Theoretical signal	Experimental signal
Constant (θ_{FULL})	multi-phase OUFIS	1.00	1.00
	2-phase OUFIS	1.00	0.97
Constant (θ_{MAX})	multi-phase OUFIS	1.17	1.11
	2-phase OUFIS	1.14	1.03
Sinusoidal (θ_{MAX})	multi-phase OUFIS	1.03	1.04
	2-phase OUFIS	1.00	0.95
Gaussian (θ_{MAX})	multi-phase OUFIS	1.26	1.14
	2-phase OUFIS	1.18	1.14
(9,9,7,7,7,7,9,9)		1.14	1.13
(12,11,11,11,4,4,11)		2.00	1.75
(18,18,17,4,3,4)		2.67	2.29
(17,17,8,8,5,4,5)		2.00	1.69

Table 4 Theoretical and experimental results for the signal changes for the different modulation schemes. Data is normalised to the constant amplitude multi-phase OUFIS result. In each case the *reduced* flip angle has been used, based on either the full or maximal (optimised) flip angle, as per the previous sections.

The table above shows that in experiments all the modulation schemes broadly follow the predicted signal increases. In most cases the results from experiments lag behind the theoretical estimates, with the discrepancy being greater for the higher performing sequences. Of the amplitude modulations, the shallow, sinusoidal modulation shows a modest signal improvement, while the steeper gaussian modulation performs better, if only giving ½- ¾ of the predicted increase. The combined amplitude and phase modulations also perform well. The simplest (9,9,7,7,7,7,9,9) modulation gives a very similar signal to that predicted, while the other more varying schemes show signal increases ¾ of that predicted.

Simulation

Modulations (amplitude, phase)		FWHM / pixels
Constant (θ_{FULL})	multi-phase OUFIS	1.1875
	2-phase OUFIS	1.1875
Sinusoidal (θ_{MAX})	multi-phase OUFIS	1.2500
	2-phase OUFIS	1.3125
Gaussian (θ_{MAX})	multi-phase OUFIS	1.2500
	2-phase OUFIS	1.3125
(9,9,7,7,7,7,9,9)		1.3125
(12,11,11,11,4,4,11)		1.2500
(18,18,17,4,3,4)		1.2500
(17,17,8,8,5,4,5)		1.3125

Table 5 Theoretical results for the resolutions for the different modulation schemes

Table 5 shows the results from simulations. Interestingly, the resolution does not vary much between the different modulations. However, it was apparent that the shape of each resolution kernel varied, with some having higher amplitude than others outside of the central peak. This may result in more noise in the image.

Experiments

The images of a complex-structured phantom, obtained with each of these modulations, are shown below. The phase encoding direction is along the vertical axis in each case. The image fade-out along the horizontal direction reflects the narrow bandwidth of the 28 μs RF pulses. This duration was chosen to fit in with the peak power capabilities of the amplifier, so as to enable high enough flip angles to be reached. The alternative technique using chirp pulses was difficult to implement on the 3T scanner at Nottingham for some of these modulation schemes.

RF	28 μs rectangular pulses
τ_S	512 μs
TE	28 ms
BW $_{acquistion}$	100 kHz
Matix	64 x 64
Resolution	2.9 x 3.2 mm
Slice thickness	9.8 mm

Figure 29 Phantom image obtained with 2 phase OUFIS, full flip angle (no amplitude modulation). The fall-off in intensity in the horizontal (frequency encoding) direction is due to the narrow bandwidth of the pulses used.

The amplitude modulation images show little, if any, blurring in the phase encoding direction, even in the case of the gaussian modulation. The images from the combined amplitude and phase modulations show varying degrees of blurring, from very little in the case of the (9,9,7,7,7,9,9) modulation, increasing to severe blurring for the (18,18,17,4,3,4) modulation.

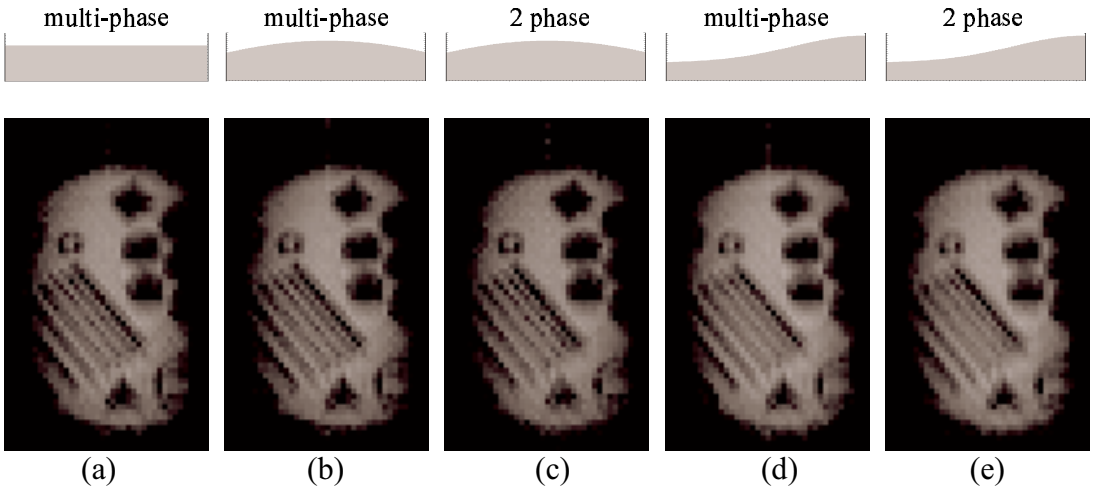

Figure 30 Segmented phantom images acquired with different amplitude and phase modulations. The amplitude and OUFIS phase modulations are shown above each image. The optimal flip angle θ_{MAX} was used in each case.

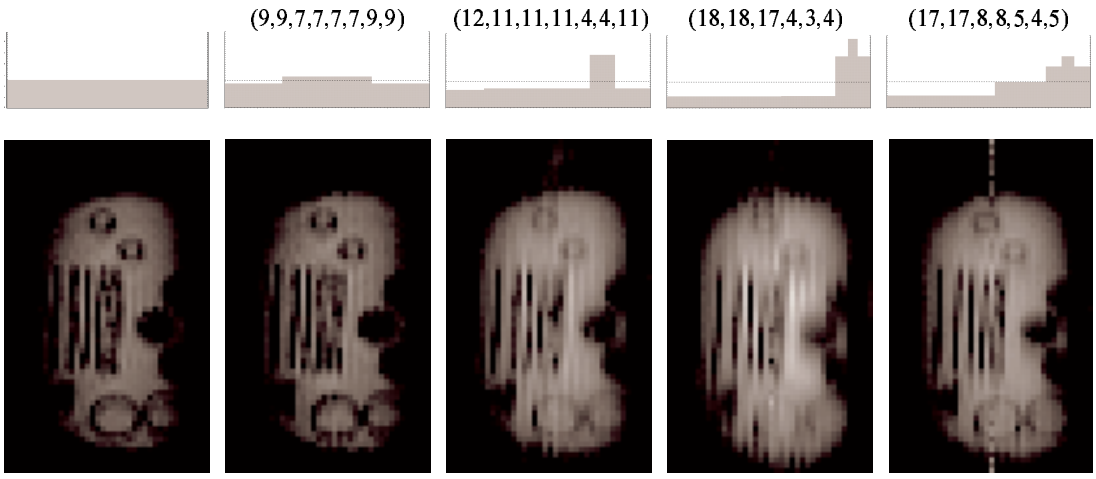

Figure 31 Segmented phantom images acquired with different combined amplitude and phase modulations. The modulations are shown above each image.

The position of the k_0 central echo varied between these images. The idea of the amplitude modulation was to encode one of the highest amplitude echoes as the k_0 echo. The position of the peak echoes can be changed simply by reordering the sub-trains of pulses. However, in general it will not be possible to position the peak pulses at any point of choosing along the pulse train, since the lengths of the sub-trains limit the possibilities for reconfiguring the overall train. This k_0 requirement can be built into the design of the modulations; however, with the example modulations examined here it was not possible to encode the echoes in the same manner for all of the schemes. For the OUFIS, (9,9,7,7,7,7,9,9), (12,11,11,11,4,4,11) modulations the k_0 echo was positioned at the 16^{th} echo, a quarter of the way down the k-space matrix, whereas for (18,18,17,4,3,4) and (17,17,8,8,5,4,5) the k_0 line was encoded at the 6^{th} echo. The same processing was carried out on all data sets. The errors resulting from different T_2 relaxation was assumed to be small, since the phantom had a long relaxation time.

The effects on resolution clearly vary widely, far more than is suggested by the predicted figures in Table 5. Indeed, these figures do not reflect the observed blurring, particularly in the most degraded images. Broadly speaking, this blurring tallies with the amplitude modulations: the more steeply-peaked the modulation, the more the image is blurred.

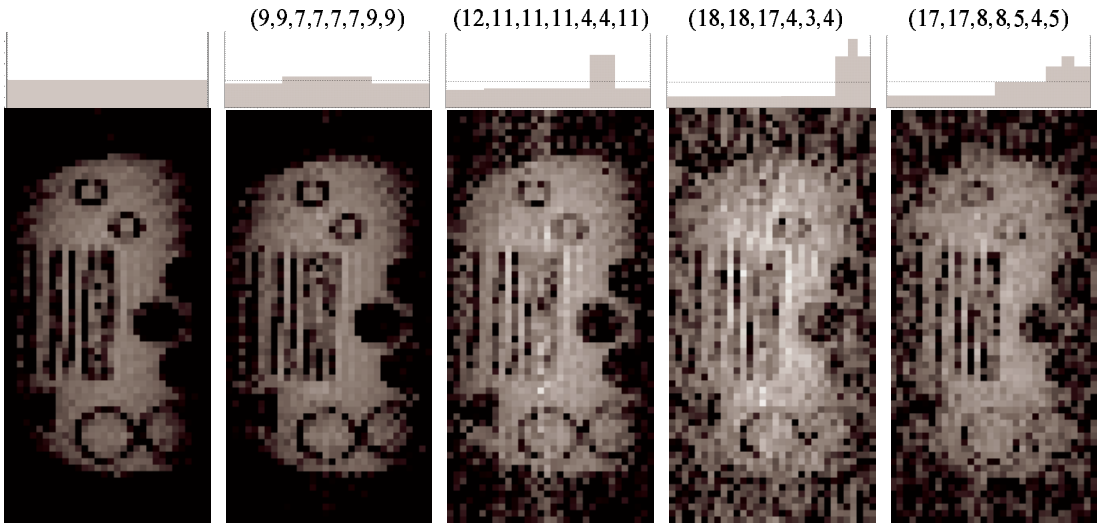

Figure 32 Images after correction with navigator echoes. All images displayed to the same scale. The modulations are shown above each image.

Modulations	SNR
Constant amplitude	25
(9,9,7,7,7,7,9,9)	16
(12,11,11,11,4,4,11)	14
(18,18,17,4,3,4)	9
(17,17,8,8,5,4,5)	13

Table 6 SNRs for the 'navigator echoes' corrected data sets.

The images were processed again, but now using a calibration data set acquired with no phase encoding gradient. These so-called 'navigator echoes' [11] were used to provide phase values to correct for any residual phase variation and amplitude values to rescale the echoes prior to processing. Figure 32 above shows the same images as Figure 31, but with the data first corrected. It is clear that the blurring in the phase encoding direction has been reduced, but at a cost of increased noise. The SNRs for the images show that the modulation schemes attempted lead to a reduction in image quality. Indeed, the more exaggerated is the modulation, the lower is the SNR.

6.4 Conclusions

This chapter has demonstrated that different modulations can be used in BURST, which can give control over the image signal and resolution.

Amplitude modulation in combination with OUFIS phase modulation can give moderate, but limited, signal improvements with little, if any, loss of image quality. Similar signal and image improvements are obtained with combined amplitude & phase modulations; however, greater signal increases are possible, at a price of lower resolution. In effect, there is a trade off of signal between inner and outer k-space. The limit of this compromise will depend on the application in question. In general, these schemes give up to 10% lower efficiencies, but the final image signals are still improved. The random and geometric phase modulations, to the very limited extent to which they were investigated, were shown to be ineffective.

The combined amplitude & phase method provides a straightforward way of producing new modulations which can be matched to requirements. Used judiciously it can provide moderate signal gains with only little detriment to the image resolution.

Further refinement to the technique might allow for more smooth variation in amplitude along the pulse train. Also, a simpler and more flexible way of generating the modulations could be investigated, which would do away with the trial and error approach.

The total RF power required for optimal excitation is fairly constant for all these modulations. However, the peak RF power required will increase with any amplitude modulation, particularly for the more extreme modulations (a seven-fold increase was required for one of the schemes described in this chapter). This is problematic for high field BURST imaging, but with the introduction of chirp pulses and, more importantly, an oscillatory gradient this will be less of an issue.

6.5 References

1. Roux, P.L., J. Pauly and A. Macovski, *BURST excitation pulses.* in 'Proc., SMRM, 10th Annual Meeting', 1991: p. 269.

2. Zha, L. and I.J. Lowe, *Optimised ultra-fast imaging sequence (OUFIS).* Magn. Reson. Med., 1995. **33**: p. 377-395.

3. Gelderen, P.v., J.H. Duyn and C.T.W. Moonen, *Analytical solution for phase modulation in BURST imaging with optimum sensitivity.* J. Magn. Reson. Series B, 1995. **107**: p. 78-82.

4. Cho, Z.H., Y.M. Ro and I.K. Hong, *FM DANTE fast imaging and variations: emerging rf-based ultrafast imaging techniques.* Concepts Magn. Reson., 1998. **10**(1): p. 33-54.

5. Hennig, J. and M. Mueri, *Fast imaging using Burst excitation pulses.* in 'Proc., SMRM, 7th Annual Meeting', 1988: p. 238.

6. Freeman, R., in *Spin choreography: basic steps in high resolution NMR*. 1997, Oxford: Spektrum. p. 156-158.

7. Pauly, J., P.L. Roux, D. Nishimura, et al., *Parameter relations for the Shinnar-Le Roux selective excitation pulse design algorithm.* IEEE Trans. Med. Imaging, 1991. **10**(1): p. 53-65.

8. Heid, O., *BURST excitation pulses.* Magn. Reson. Med., 1997. **38**: p. 585-590.

9. Duyn, J.H., P.v. Gelderen, G. Liu, et al., *Fast volume scanning with frequency shifted BURST MRI.* Magn. Reson. Med., 1994. **32**: p. 429-432.

10. Hennig, J., *Multiecho imaging sequences with low refocussing flip angles.* J. Magn. Reson., 1988. **78**: p. 397-407.

11. Doran, S., *Private Communication*.

7 Reducing Peak Power with Frequency Modulated Pulses

7.1 Introduction

Previous developments in BURST imaging have led to highly efficient phase modulation schemes, which excite almost all the magnetisation and produce near-optimal echo trains [1-3]. These schemes have been successfully implemented by other researchers at 1.5T, however in our experiments at 3T it was found that the peak power levels required were not obtainable with our 2 kW RF amplifier. BURST imaging, by its nature, is a relatively high bandwidth technique and, as such, it requires short duration RF pulses to excite the full FoV. As a consequence a relatively large pulse amplitude is required in order to obtain high enough flip angles, and this has led to the hardware-imposed limit.

A typical RF bandwidth in BURST is 125 kHz (corresponding to a 256 mm wide FoV with a 11.5 mT/m excitation gradient) compared with an RF bandwidth of 2 kHz (corresponding to a 4 mm slice and 11.7 mT/m gradient) for a slice selective excitation pulse in other imaging techniques, such as EPI. Pulse durations scale with the reciprocals of their bandwidths for an equivalent flip angle. Therefore, the duration of BURST RF pulses will be shorter by a factor of $^{2}/_{125}$, and the reciprocal of this ratio gives the factor by which the amplitude of the BURST pulse must be greater than that of a conventional excitation pulse.

In 64 pulse OUFIS the optimum flip angle is equal to $^{1}/_{8}\times^{\pi}/_{2}$. Hence, the amplitude required of the RF pulses in BURST will be greater than that of a conventional excitation pulse by a factor $^{1}/_{8}\times^{125}/_{2} \sim 8$. This corresponds to an increase in peak RF power by a factor of $8^2 = 64$. On our 3T machine a peak transmitted power of 320 W was recorded for a 1.7 kHz bandwidth 90° pulse – the peak power of a BURST RF pulse would be approximately 20 kW, far outside the range of the 2 kW amplifier.

This left us with only the option of using longer duration pulses of narrower bandwidth if the optimum flip angle was to be reached. This resulted in a localised imaging technique in which a narrow band of spins was fully excited, whilst the remainder of the desired FoV was left unexcited. It was then realised that this gave

us the means to excite the full FoV with a minor modification to the sequence. If each individual RF pulse were replaced by a short series of pulses, each of optimum flip angle but of narrow bandwidth, then by stepping the frequency of successive pulses in the series the full FoV could be excited, band by band. This then led to the idea of a single long pulse in which the frequency was increased continuously through its duration i.e. a frequency modulated (FM) pulse.

FM pulses can be used to reduce the peak power required. The bandwidth of these pulses is related to the frequencies within the pulses rather than the pulse duration (as is the case with AM pulses). Hence, a chosen bandwidth can be excited by pulses of longer duration and lower amplitude than is possible using amplitude modulation alone. One consequence of FM pulses is that they produce a quadratically varying phase in the magnetisation, which leads to a residual dephasing and, ultimately, to a loss of signal. However, it will be shown that for the particular case of the BURST imaging sequence there is no loss in signal.

7.2 Theory of FM pulses

7.2.1 Chirp pulses and their frequency response

Conventional RF pulses used in MRI are amplitude modulated, where the modulation envelope of the pulse determines the range of frequencies excited by the pulse. An additional degree of freedom can be obtained by modulating the frequencies, or more generally the phase, within a pulse also. An FM pulse of constant amplitude in which the frequency is swept linearly through the duration of the pulse is called a *chirp* pulse. The instantaneous frequency of a chirp pulse is given by $\omega = \alpha t$, where α (in rad s^{-2}) is a constant equal to the rate of frequency sweep within the pulse.

The phase of such a pulse varies as,

$$\varphi = \int_0^t \alpha t' \cdot dt' = \frac{\alpha}{2} t^2 \qquad (54)$$

Hence, the phase is quadratic and the chirp pulse can be described as,

$$S(t) = A(t) \cdot e^{i \cdot \frac{\alpha t^2}{2}} \tag{55}$$

where $A(t)$ defines the amplitude modulation envelope

The response of the magnetisation to such a pulse is well-approximated at low flip angles by its Fourier transform. For the case $A(t) = A_0^{FM} = constant$, i.e. a pulse of constant amplitude and infinite duration, the Fourier transform can be calculated as follows,

$$\hat{S}(\omega) = \frac{A_0}{2\pi} \int_{-\infty}^{\infty} e^{i \cdot \frac{\alpha t^2}{2}} e^{-i\omega t} dt \tag{56}$$

$$= \frac{A_0}{2\pi} \int_{-\infty}^{\infty} e^{i \cdot \frac{\alpha}{2}(t-\omega/\alpha)^2} e^{-i\frac{\omega^2}{2\alpha}} dt$$

$$= \frac{A_0}{2\pi} e^{-i\frac{\omega^2}{2\alpha}} \int_{-\infty}^{\infty} e^{i \cdot \frac{\alpha}{2}(t')^2} dt' \tag{57}$$

where $t' = t - \omega/\alpha$.

It is not obvious how this integral can be evaluated, nor indeed whether or not it converges at $\pm\infty$ at all. However, by introducing an additional exponential factor ($e^{-\beta t^2}$, where the positive, real parameter β can be chosen at will) into the integrand, the function can be made to converge and it can then be treated as a standard integral, that of a gaussian.

The integral becomes

$$\hat{S}'(\omega) = \frac{A_0}{2\pi} e^{-i\frac{\omega^2}{2\alpha}} \int_{-\infty}^{\infty} e^{-\beta(t')^2} e^{i \cdot \frac{\alpha}{2}(t')^2} dt'$$

$$= \frac{A_0}{2\pi} e^{-i\frac{\omega^2}{2\alpha}} \int_{-\infty}^{\infty} e^{-\left(\beta - i\frac{\alpha}{2}\right)(t')^2} dt' . \tag{58}$$

The integrand now converges at the upper and lower limits and the following result for a gaussian function ($e^{-\varepsilon x^2}$, where ε is real and positive) is valid,

$$\int_{-\infty}^{\infty} e^{-\varepsilon x^2} dx = \sqrt{\frac{\pi}{\varepsilon}} . \tag{59}$$

Substituting this result into Equation (58) above yields

$$\hat{S}'(\omega) = \frac{A_0}{2\pi} \sqrt{\frac{\pi}{\beta - i\alpha/2}} \cdot e^{-i\frac{\omega^2}{2\alpha}} . \tag{60}$$

Then, by reducing β the attenuation can be reduced,

$$\text{as } \beta \to 0,\ e^{-\beta t^2} \to 1 \text{ and } \hat{S}'(\omega) \to \hat{S}(\omega) .$$

In this case,

$$\hat{S}'(\omega) \to \frac{A_0}{\sqrt{2\pi}} \frac{1}{\sqrt{2\alpha}} (i+1) e^{-i\frac{\omega^2}{2\alpha}} . \tag{61}$$

Therefore, the Fourier transform of an infinite duration, constant amplitude chirp function is given by,

$$\hat{S}(\omega) = A_0^{FM} \frac{1}{\sqrt{2\pi}} \frac{1}{\sqrt{2\alpha}} \cdot (1+i) \cdot e^{-i\cdot\frac{\omega^2}{2\alpha}} . \tag{62}$$

To provide a practical RF pulse the chirp function must be truncated. It is found that the bandwidth of response of a truncated pulse is approximately given by the range of frequencies swept out by the pulse. Hence, the bandwidth of a chirp pulse can be controlled, unlike that of an AM pulse, so that a longer duration pulse of the same bandwidth can be produced.

For pulse of duration τ_{FM}, bandwidth of response $\quad \mathbb{BW} \sim \alpha\tau_{FM}$	(63)

This approximation has been found to be very accurate for pulses with a sharp rectangular envelope and for full bandwidths measured at half maximum values.

Example: A chirp pulse extending from t=-50 to t=+50 μs with α=6.3x10^9 r s^{-1} sweeps out frequencies from –50 to +50 kHz. Hence, its bandwidth is ~100 kHz.

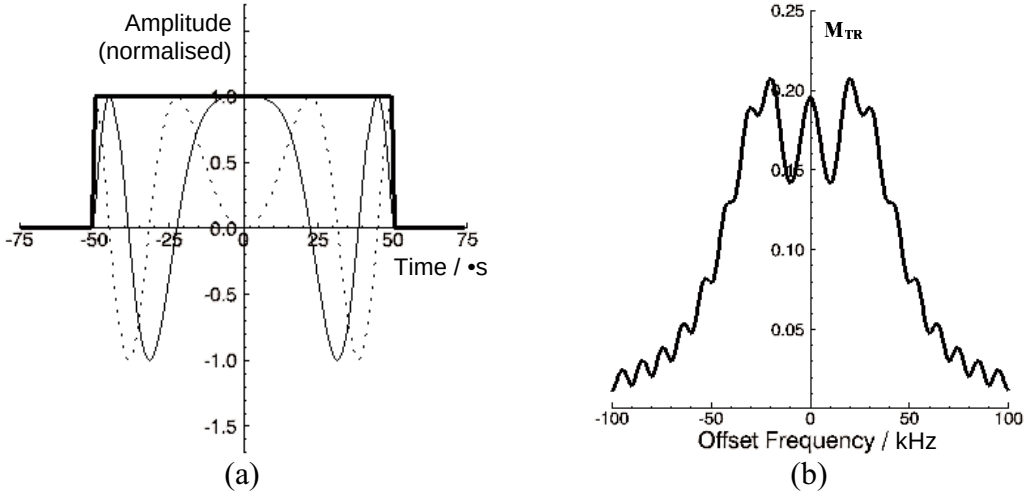

Figure 33(a) Chirp pulse. Solid line – real component, dotted line – imaginary component, bold line – pulse amplitude. (b) Simulated response for flip angle π/16 on resonance.

The choice of windowing function affects the uniformity of the in-band excitation and the out-of-band ripple, as well as the sharpness of the cut-off inbetween. This is described further in Section 7.2.2 below.

Furthermore, on resonance the flip angle of a truncated pulse can be well-approximated by the above Fourier transform if sufficiently wide a truncation envelope is chosen. This can be shown as follows.

A pulse truncated to a width τ is described by

$$S(t) = \begin{cases} A_0^{FM} \cdot e^{i\cdot\frac{\alpha t^2}{2}} & -\tau/2 < t < +\tau/2 \\ 0 & \text{otherwise.} \end{cases} \qquad (64)$$

In the frequency domain this corresponds to a convolution by a sinc function,

$$\hat{S}(\omega) = A_0^{FM} \frac{1}{\sqrt{2\pi}} \frac{1}{\sqrt{2\alpha}} (1+i) \cdot e^{-i\cdot\frac{\omega^2}{2\alpha}} \otimes \frac{\tau}{\sqrt{2\pi}} \cdot \mathrm{sinc}(\omega\tau/2). \qquad (65)$$

Evaluating $\hat{S}(0)$,

$$\hat{S}(0) = A_0^{FM} \frac{\tau}{2\pi} \frac{1}{\sqrt{2\alpha}} (1+i) \cdot \int_{-\infty}^{\infty} e^{-i \cdot \frac{\omega'^2}{2\alpha}} \mathrm{sinc}(\omega' \tau / 2) d\omega' . \quad (66)$$

The phase of the integrand at the first zero of the sinc ($\omega=2\pi/\tau$) is given by $\varphi_1=2\pi^2/\alpha\tau^2$. For a pulse bandwidth of 100kHz and a pulse duration of 500μs, and using the approximation given in Equation (63), $\varphi_1 \sim \pi/50$ (~ 1°). This dephasing would have a negligible effect on the value of the integral within the central lobe. Outside of the central lobe the value of the sinc function is much smaller and the contribution to the integral from this region is much less. Indeed, when the phase of the integrand has reached $\pi/2$, the sinc function has reached the 5th zero crossing (see Figure 34 below). Therefore, at $\omega=0$ the phase term in the integrand has very little effect on the integral, which can then be approximated by the integral of the sinc alone. The value of the expression is then

$$\hat{S}(0) \approx A_0^{FM} \frac{\tau}{2\pi} \frac{1}{\sqrt{2\alpha}} (1+i) \cdot \int_{-\infty}^{\infty} \mathrm{sinc}(\omega' \tau / 2) d\omega' \approx A_0^{FM} \frac{1}{\sqrt{2\pi}} \frac{1}{\sqrt{2\alpha}} (1+i) . \quad (67)$$

Hence, on resonance the response of the spins is approximately the same as for the infinite function.

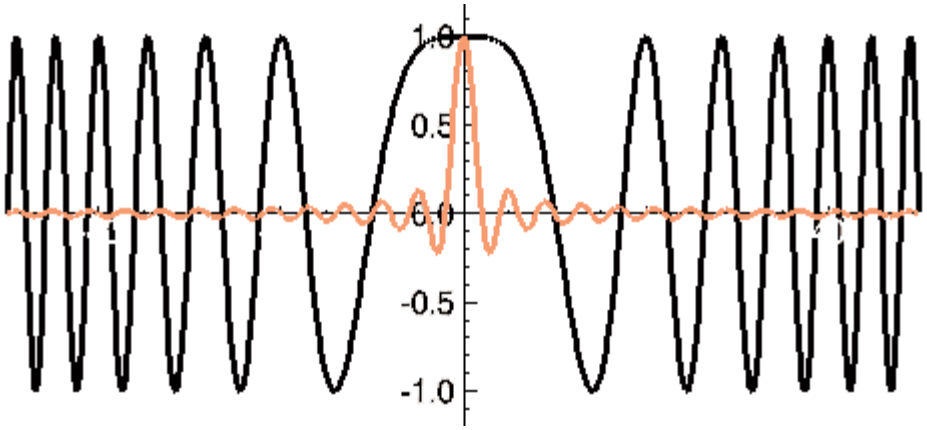

Figure 34 Plot showing the centre of the quadratic phase function (black line – real component) and the sinc function (red line) in the integrand of Equation (66).

The Fourier transform shows that the chirp pulse leads to a quadratic dephasing across the FoV. The total dephasing produced by the pulse can be obtained from Equation (62) above.

The phase is conjugated by the 180° refocussing pulse.

$$\varphi_\omega = \omega^2 / 2\alpha$$

At the edge of the FoV, $\omega = \pm BW / 2$

$$\Rightarrow \varphi_{BW/2} = BW^2 / 8\alpha$$

Then, substituting for BW and α,

$$BW = \alpha\tau_{FM} = 2\pi / \tau_{AM}$$

where τ_{AM} is the duration of a comparable sinc pulse.

$$\Rightarrow \varphi_{BW/2} = \alpha\tau_{FM}^2 / 8 = \pi / 4 . \tau_{FM}/\tau_{FM}$$

At centre of the FoV, $\omega = 0, \varphi_0 = 0$

$$\text{Phase difference across FoV} = \frac{\pi}{4} \cdot \frac{\tau_{FM}}{\tau_{AM}} \qquad (68)$$

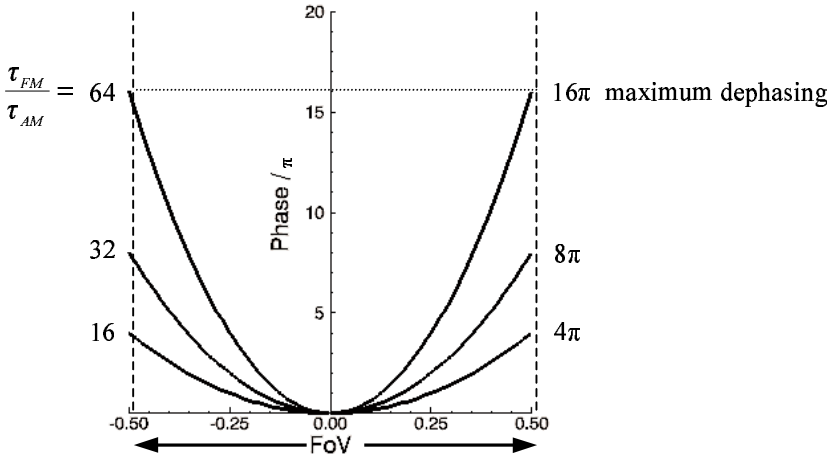

Figure 35 Dephasing across the field of view for different chirp pulse durations

The earlier description of the development of the idea of FM pulses gives an intuitive insight into the behaviour of the spins under a chirp pulse. A chirp pulse with modulation $A(t) = A_0 = constant$ is given by,

$$S(t) = A_0 \cdot e^{i \cdot \frac{\alpha t^2}{2}} \tag{69}$$

This signal shows a degree of symmetry in time with respect to different offset frequencies. This can be seen by rewriting this expression for spins in a frame rotating at offset frequency Δ, as shown by Kunz [4].

$$S_\Delta(t) = S(t) \cdot e^{-i\Delta t} = S_0 \cdot e^{i \cdot \frac{\alpha t^2}{2}} e^{-i\Delta t} = \underline{S_0 \cdot e^{i \cdot \frac{\alpha}{2}(t - \Delta/\alpha)^2} e^{-i \cdot \frac{\Delta^2}{2\alpha}}} \tag{70}$$

Therefore, the response of a spin rotating at offset frequency Δ is the same as that of a spin on resonance, but shifted later by a time Δ/α and phase shifted by $-\Delta^2/2\alpha$, which is equal to the phase of the pulse at $t = \Delta/\alpha$. Windowing of this function to produce a truncated pulse produces a very similar response over the pulse bandwidth, with a highly quadratic phase. In MRI such a pulse would excite spins sequentially across the FoV, from the lowest frequencies up to the highest in the pulse bandwidth. In this way the energy of the pulse is distributed in time, resulting in a reduced peak power.

7.2.2 Windowing of pulses

The windowing function $A(t)$ determines the shape of the excitation profile, and the bandwidth of the response is determined by the range of frequencies swept out by the windowed pulse. However, a sharp rectangular truncation envelope produces a pulse which gives a highly rippled excitation profile with moderate out-of-band excitation. A smoother truncation can be obtained by applying a Hamming window to the pulse. Different widths of Hamming window were investigated to determine the envelope which gave the best profile, as measured by the excitation bandwidth per unit pulse power.

7.2.3 Peak power

The amplitude of a chirp pulse can be compared with that of a sinc pulse of the same bandwidth through the Fourier transform. This is a good approximation for the low flip angle pulses required in BURST. For higher pulse amplitudes, beyond the Fourier regime, the flip angle of the chirp pulse increases more slowly (less than linearly) and it ultimately tends towards 180° in a similar fashion to adiabatic pulses [4].

An infinite duration sinc pulse of bandwidth BW is given by

$$S(t) = A_0^{AM} \cdot \mathrm{sinc}(BW \cdot t/2) \tag{71}$$

Its Fourier transform is, A_0^{AM}

$$\hat{S}(\omega) = \begin{cases} A_0^{AM} \cdot 1/BW & -BW/2 < \omega < +BW/2 \\ 0 & \text{otherwise} \end{cases} \tag{72}$$

In practice the sinc pulse will be truncated. However, if the total duration of the sinc pulse is made the same as the chirp pulse, and if $\tau_{FM} >> \tau_{AM}$, where τ_{AM} is the FWHM of the central sinc lobe, then the excitation profile would be largely similar to the infinite sinc pulse. The truncation envelope in the time domain leads to a narrow sinc convolution kernel in the frequency domain, which in turn would produce only small ripples on the excitation profile.

For pulses of the same flip angle equations (62) & (72) can be compared.
Equating the modulii of the frequency responses,

$$\left|\hat{S}(\omega)\right| = \frac{A_0^{FM}}{\sqrt{2\pi} \cdot \sqrt{\alpha}} = \frac{A_0^{AM}}{BW} \tag{73}$$

Substituting $\alpha \sim BW / \tau_{FM}$, from Equation (63), and $BW = 2\pi / \tau_{AM}$ gives,

$$\frac{A_0^{FM}}{A_0^{AM}} = \frac{\sqrt{\alpha} \cdot \sqrt{2\pi}}{BW} \approx \frac{\sqrt{2\pi}}{\sqrt{BW \cdot \tau_{FM}}} \approx \sqrt{\frac{\tau_{AM}}{\tau_{FM}}} \tag{74}$$

Hence, the ratio of peak powers is given by,

$$\frac{P_{pk}^{FM}}{P_{pk}^{AM}} = \left(\frac{A_0^{FM}}{A_0^{AM}} \right)^2 \approx \frac{2\pi}{BW \cdot \tau_{FM}} \approx \frac{\tau_{AM}}{\tau_{FM}} \tag{75}$$

For FM pulses of constant bandwidth the peak power approximately scales inversely with duration. This approximation holds best for rectangular chirp pulses where $\tau_{FM} >> \tau_{AM}$ and for FWHM bandwidth. In BURST, an upper limit to the pulse duration is set by the period of the pulse train, τ_s. As explained earlier (Section 3.7.3) the pulse spacing determines the image resolution, and since the pulse duration, τ_{AM}, determines the bandwidth of excitation, the maximum theoretical reduction in peak power is given by,

$$\left. \frac{P_{pk}^{FM}}{P_{pk}^{AM}} \right|_{MAX} \approx \frac{\tau_{AM}}{\tau_S} = \frac{resolution}{bandwidth} = \frac{1}{N_x} \tag{76}$$

where N_x is the number of pixels in the readout direction.

Therefore, a theoretical maximum N_x-fold reduction in peak power is possible. The total RF power is not affected.

7.2.4 Previous work using FM pulses

The quadratic phase of the RF pulses leads to a quadratic phase in the spins across the excitation bandwidth, as shown earlier in Equation (62). This characteristic of FM pulses has limited their use for slice selective excitation in MRI previously. The quadratic phase cannot be refocussed by the action of linear gradients and this leads to a reduction in signal amplitude. A technique for refocussing the spins was developed by Kunz, who used a 90° FM pulse in combination with a 180° refocussing FM pulse for slice selection [5]. The 90° pulse alone, or with a conventional refocussing pulse, would lead to a greatly reduced signal. However, Kunz demonstrated that a 180° refocussing FM pulse would also produce a quadratic phase variation, and that with suitable choice of gradient and frequency sweep parameters the effects of one pulse could be made complementary to the other, resulting in a constant phase of the spins through the slice. In BURST imaging the

excitation component of the sequence is different in that the RF excitation pulse is applied in the presence of a gradient in the frequency-encoding direction producing a many-pixel wide excitation, rather than a single pixel deep slice selective excitation.

Maudsley [6] investigated the use of 'phase scrambled' RF pulses and non-linear gradients as two independent methods for producing a variation in the phase over the FoV, thereby reducing the peak echo amplitude of Fourier encoded data, and so increasing the dynamic range of the acquired signal. He noted that greater reductions in the signal peak resulted from chirp pulses rather than from random phase pulses. Also, his pulse sequence generated a 2D phase variation over the imaged slice and no phase variation through the slice.

Johnson et al. [7] used a discontinuous phase scrambling technique, which produced a constant phase within each pixel, but a scrambled phase between pixels. This was developed for application in combination with RF phase encoding for spectroscopic imaging. A rectangular PSF can be obtained, which reduces contamination of the signal from nearby pixels. This technique also removes the dephasing within individual pixels which otherwise would reduce the signal. Again, both random phase and chirp pulses were examined and a greater reduction in signal was noted for the chirp pulses. However, to generate a rectangular PSF would require a sinc pulses of duration > $4\tau_S$ (to include 1st side lobes), which is clearly not possible in BURST.

7.2.5 Consequences of quadratic phase in BURST

The implications of a quadratic phase in the magnetisation depend on the parameters of the excitation and the acquisition. However, frequency modulation in BURST can be introduced on two levels: for individual RF pulses and for the pulse train envelope.

7.2.5.1 Chirp pulses

The BURST excitation is volumar and the quadratic phase is produced along the readout direction. Across the whole FoV the spins are totally dephased, but within each pixel there is only a small phase variation and therefore only a small degree of signal dropout. This intra-pixel dephasing is least at the centre of the FoV and

gradually increases with distance outwards in the readout direction. The signal from individual pixels can be precisely determined by integrating the magnetisation profile over each pixel.

$$P(i) = \int_{i^{th}\,pixel} I(\omega) \circ \hat{S}(\omega) \circ d\omega \tag{77}$$

where $I(\omega)$ is the spin density.

The greatest dephasing, which will be in the outermost pixels, can be estimated as follows. From Equation (62) the phase of the magnetisation at t =0, the centre point of the refocussing, is given by,

$$\varphi_{\omega} = \frac{\omega^2}{2\alpha} \tag{78}$$

(the sign is now positive following the 180° pulse).

If the frequency variable is now changed to $l = \frac{\omega}{\Delta\omega} = pixel\,number$, where $\Delta\omega$ is the resolution, and the following substitutions are made,

$$\Delta\omega = \frac{BW}{N_x} = \frac{2\pi}{\tau_S} \qquad \& \qquad \alpha \approx \frac{BW}{\tau_{FM}} \tag{79}$$

where N_x is the number of the pixels in the readout direction,
the phase can be written,

$$\varphi_l \approx l^2 \circ \frac{\pi}{N_x} \circ \frac{\tau_{FM}}{\tau_S} \tag{80}$$

The phase across the outermost pixel is,

$$\Delta\varphi_{\substack{outermost \\ pixel}} = \varphi_{Nx/2} - \varphi_{Nx/2-1} \approx \frac{(N_x - 1)\pi}{N_x} \circ \frac{\tau_{FM}}{\tau_S} \approx \pi \circ \frac{\tau_{FM}}{\tau_S} \tag{81}$$

In BURST the sampling window is equal in duration to the spacing of the RF pulses,

$$\tau_S = \tau_P \geq \tau_{FM} \tag{82}$$

$$\Rightarrow \quad \Delta\varphi_{\substack{outermost \\ pixel}} \leq \pi \tag{83}$$

The maximum possible dephasing across a pixel due to chirp pulses in BURST is ~π. This would lead to a decrease in pixel intensity of 35% (evaluated by numerical simulation) at the edge of the FoV (assuming a constant spin density). For shorter pulses the dephasing is much less. For a pulse spacing τ_S = 512 μs and a pulse length τ_{FM} ~ 128 μs, the dephasing is approximately π / 4 (= 45°) which would lead to only a 2% reduction in pixel intensity. However, BURST is a peculiar technique which results in a pixel excitation profile which might not be uniform in either amplitude or phase. In the next section the effect of the phase modulation of the pulse train on the magnetisation is examined, and it is shown that in BURST there is, in fact, no reduction in pixel intensity due to the chirp pulses.

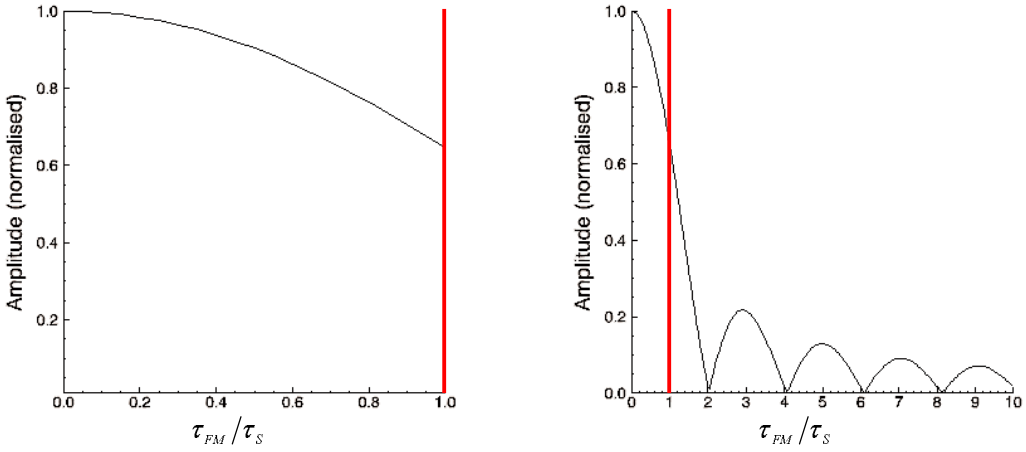

Figure 36 The net signal from the outermost pixels is shown for different sampling window durations. (a) shows the values encountered in BURST. The chirp pulse described above has τ_{FM}/τ_S ~0.25, which leads to only a 2% reduction in signal intensity in the outermost pixels.

7.2.5.2 OUFIS and FM-BURST

It is interesting to note the parallel between the use of chirp pulses in BURST and the phase modulation schemes of OUFIS [1] and FM-BURST [3], which use a similar principle to modulate the phases along the entire pulse train in order to excite all the magnetisation (as explained in Section 6.2.2.3). With no phase modulation, only a

narrow strip is excited within each pixel (of width $^1/_{N_P}$ of a pixel, where N_P is the number of pulses in the RF train), but with a quadratic phase modulation each pixel can be fully excited. And so, the width of the Fourier transformed envelope function is broadened to a full pixel's width, which leads to a $\sqrt{N_P}$ increase in signal [3]. However, the quadratic dephasing is now an important factor.

In contrast to the individual chirp pulses the frequency modulation of the entire pulse train leads to significant intra-pixel dephasing. The net signal is now small compared to a fully refocussed pixel. From Equation (80) it can be shown that the phase roll across a single pixel is 16π at the mid-point of the echo train (for $N_P = 64$).

Substituting $N_x = 1$ (since the bandwidth of the envelope alone is equal to one pixel) and $\tau_{FM} = N_P \cdot \tau_S$, where τ_S is the period of the pulse train.

$$\varphi_l = l^2 \cdot \frac{\pi}{N_x} \cdot \frac{\tau_{FM}}{\tau_S} = l^2 \cdot \pi \cdot N_P \tag{84}$$

Across this single pixel l varies from –½ to +½ and hence the phase at the pixel edges is equal to,

$$\varphi_{l=\pm 1/2} = \frac{\pi}{4} \cdot N_P \tag{85}$$

Hence, for 64 pulses the phase roll is 16π.

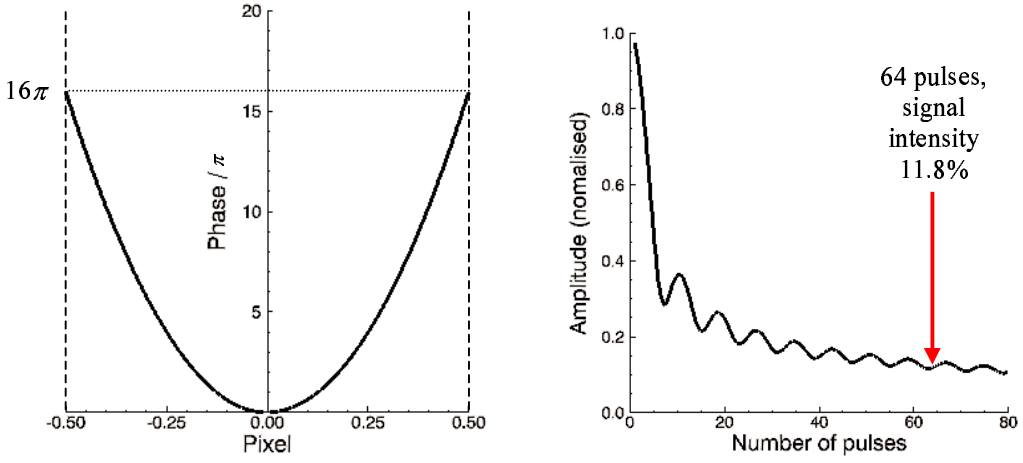

(a) (b)

Figure 37 (a) Dephasing across a single pixel from Equation (84) with $N_P = 64$, and (b) Net signal intensity from a single pixel for different N_P (c.f. [3])

As a result of this dephasing the net signal from each pixel is reduced to 11.8% of the full pixel signal, similar to that predicted from considerations of energy (12.5%, see Section 5.2). This dephasing explanation gives another angle on the low SNR of BURST.

Phase evolution and the formation of echoes

The BURST pulse train ({envelope x δ-train} ⊗ RF pulse) excites spins across the full bandwidth of the individual pulses. The periodic δ-train in the excitation function translates to a periodic δ-train in the magnetisation, so that the single pixel excitation above is aliased across the full bandwidth (see Section 3.7.3).

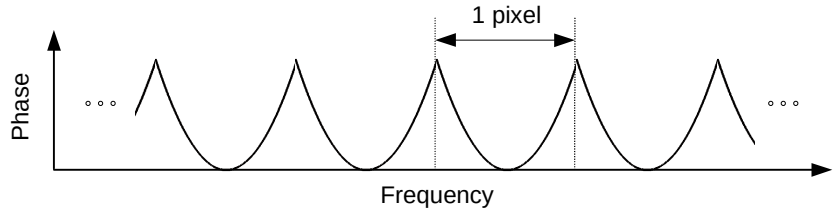

Figure 38 Schematic view of the phase variation across several pixels, extending over the full bandwidth

In the case of a quadratic phase function the effect of the refocussing gradient is to shift the parabola within each pixel.

For spins in the central pixel at time t in the presence of the readout gradient,

$$\varphi(t) = \frac{\omega^2}{2\alpha} + \omega t = \frac{1}{2\alpha} \cdot (\omega + \alpha t)^2 - \frac{\alpha t^2}{2} \qquad (86)$$

for $-BW/2 < \omega < BW/2$.

Hence, the linear gradient translates the parabola, but does not affect its shape (determined by the ω^2 coefficient). The turning point of the parabola follows the locus of points given by the parametric equations,

$$\omega = -\alpha t \qquad \varphi = -\frac{\alpha t^2}{2} \tag{87}$$

or alternatively,

$$\varphi = -\frac{\omega^2}{2\alpha} \tag{88}$$

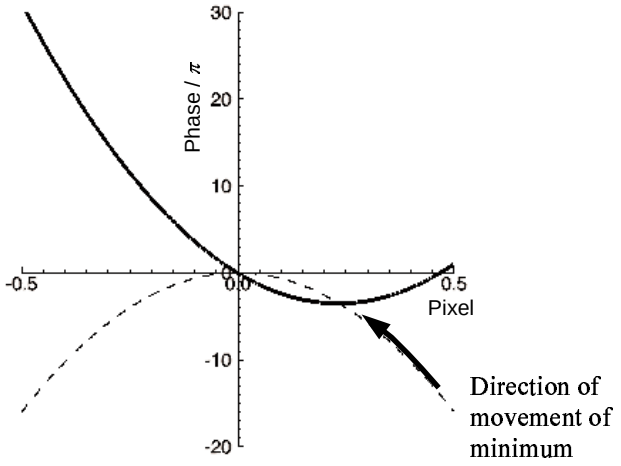

Figure 39 Phase evolution within a pixel. Dotted line – locus of the minimum, solid line – example phase distribution for t<0 i.e. before the mid-point of the echo.

This phase matches that of the resultant echoes ($-\alpha t^2/2$). This is a reasonable result given that the rate of change of phase within the pixel is least around the parabola minimum. Most of the resultant signal comes from spins around this point. Here the spins interfere constructively, away from this point the spins interfere destructively.

This picture of the evolution of phase across a single pixel can be extended across the whole image. More generally, outside of the central pixel, the phase evolution acquires a further term, which adds only a uniform amount across each pixel.

$$\varphi(t) = \frac{\omega'^2}{2\alpha} + \omega' t + \omega_0 t = \frac{1}{2\alpha} \cdot \left(\omega' + \alpha t\right)^2 - \frac{\alpha t^2}{2} + \omega_0 t \tag{89}$$

for $(\omega_0 - BW/2) < \omega < (\omega_0 + BW/2)$, where ω_0 is the offset frequency of the pixel centre, and $\omega' = \omega - \omega_0$

The minimum of the phase parabola within each pixel shifts from the right hand side (high frequency) to the left hand side (low frequency) under the action of the refocussing gradient (for positive α). In this way different parts of each pixel will contribute to each echo, and the echo phases will follow the phases of the minima. This localised contribution from each pixel is very similar to single phase BURST, in which a narrow strip of spins is excited within each pixel. As the spins in these periodically displaced strips move collectively into phase (by integer multiples of 2π) and out of phase, the characteristic train of echoes is formed. An identical interpretation can be used in the case of FM-BURST, as the phase of the periodically displaced minima are brought in to and out of phase (by integer multiples of 2π) by the action of the gradient.

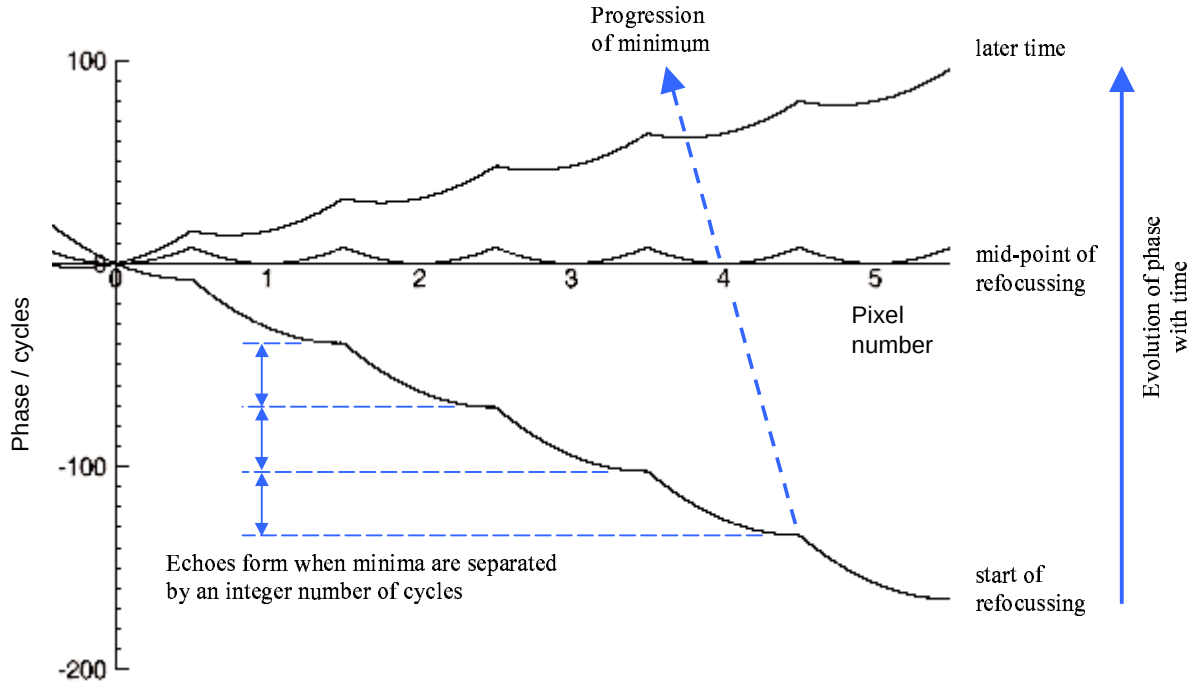

Figure 40 Phase evolution across pixels at the centre of the FoV. Bottom line – start of refocussing, middle line – mid-point of refocussing, top line – a later point in the refocussing.

7.2.5.3 Net signal loss resulting from quadratic phase

The combined effect of the chirp pulses and the phase modulation of the pulse train is to produce a superposition of the two quadratic phase variations. The OUFIS and FM-BURST phase modulations lead to a large intra-pixel dephasing, which leads to the characteristic reduced signal of BURST, whereas the chirp pulses lead to a

smaller dephasing across the whole FoV, which can itself lead to significant signal drop out. However, the addition of these two phase variations would not lead to a cumulative loss in signal. In fact, by reversing the directions of the frequency sweeps of the chirp pulses and pulse train modulations the net dephasing could be reduced; the two quadratic coefficients are of opposite sign and will result in reduced intra-pixel dephasing, with a slight shift of the parabolas' minima. However, in practice this is not necessary since the quadratic coefficients of the two phase variations are a few orders of magnitude apart (for $N_P = N_x = 64$; see equations (80) & (84)) and there is little net change in signal, for better or for worse, as a result. Therefore, the prediction of signal loss in the outer pixels made above is not valid in BURST.

Finally, the question of whether there will be any further reduction in signal from the cumulative dephasing can be avoided altogether. It is not, in fact, necessary to have any knowledge at all of the functional form of the phase variation. It can be simply demonstrated that the pixel intensity can be made to remain unchanged, regardless of the phase across the chirp pulse bandwidth. With a minor modification to the pulse train the inter-pixel phase variation can be changed from continuous to discrete, thereby separating out the two phase functions. The BURST excitation is shown in Figure 41(a). A frequency modulated DANTE envelope function produces a discrete stepping of the phase between successive pulses of the train. Fourier transform then shows that this results in the continuous superposition of the phases of the pixel profile and the excitation envelope. In Figure 41(b) the order of the multiplication and the convolution are reversed in the RF train. This effectively reverses the situation in (a); a continuous superposition of the phases of the pulse envelope and the chirp pulses results in a discrete stepping of the phase between successive echoes. Hence, within each pixel the phase is unchanged from that due to the DANTE envelope alone, apart from a constant offset.

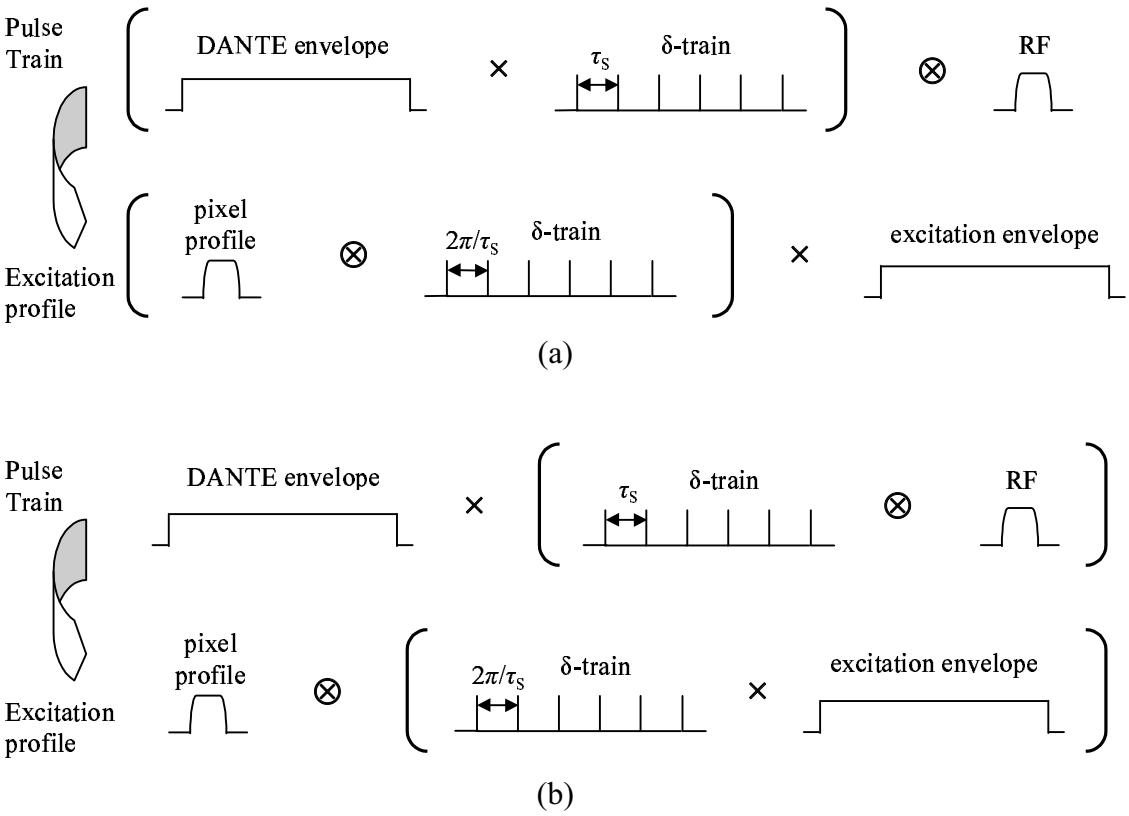

Figure 41 Mathematical description of the BURST pulse train, and its Fourier transform. (a) conventional, as previously described, and (b) modified to eliminate cumulative dephasing.

7.3 Results

7.3.1 Simulations

Simulations were performed on chirp pulses truncated with different windowing functions. For a selected bandwidth the different pulses were compared using the 'bandwidth per unit power' as the figure of merit. The bandwidth was measured as the full width at $^1/_{\sqrt{2}}$ of the mean value of the transverse magnetisation measured over the central ~50% of the excitation band. Also, the reduction in peak power obtained was compared with the theoretical prediction.

Two methods of simulation were considered: the Fourier transform and a numerical simulation of the Bloch equations. The pulses investigated were of the low flip angles (~π/16) typical in BURST. The two methods gave near-identical results for

these pulses, and therefore the simpler Fourier transform was sufficient for our optimisation purposes.

Chirp pulse	Windowing function	τ / μs	α / rad s^{-1}	Bandwidth / kHz
1	rectangular	128	6.1 x 10^9	106
2	40 % Hamming	156	6.1 x 10^9	106

Table 7 Chirp pulse parameters

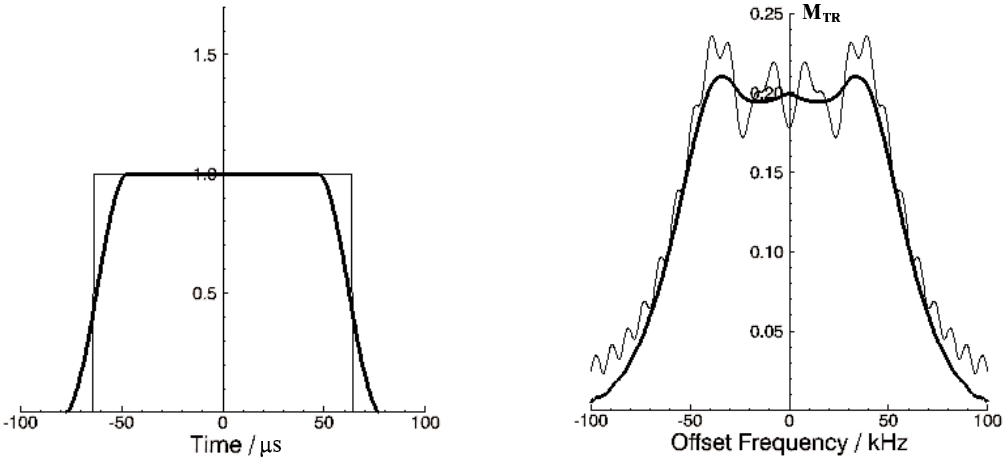

Figure 42 (a) Pulse profiles and (b) simulated responses for chirp pulses with a rectangular window (bold line) and a 40% Hamming window duration. The bandwidths are the same (106 kHz)

The rectangular windowed chirp pulse produces a broad but jagged excitation profile. A Hamming window (a cosine function, $0 \rightarrow \pi$) was used to smooth the pulse cut-off and, consequently, to smooth the excitation profile and reduce out-of-band excitation. The width of the window was varied in conjunction with the overall pulse duration to produce pulses of the same bandwidth, as observed in simulations. The performance of example pulses is given in Table 8 below. For comparison a truncated sinc pulse (not shown above) with a duration approximately equal to the rectangular chirp pulse (128μs) was used. The central lobe of the sinc was ~10μs in duration, much shorter than the truncation envelope. Consequently, the truncation envelope resulted in a narrow convolution kernel in the frequency domain (following Fourier transform), which led to some rippling across the excitation band, but did not otherwise significantly affect the excitation profile. The results show that the sinc

has a better performance than the chirp pulses, whilst the windowed chirp has a markedly improved performance over the rectangular chirp.

Another way to derive a pulse is to take the inverse Fourier transform of the desired excitation profile, as demonstrated by Kunz [4]. In his work a very narrow gaussian was used to smooth the edges of the excitation profile, and this was transformed into a chirp-like pulse with a similar envelope to the Hamming-windowed pulse above.

Pulse	BW / power (normalised)	Amplitude (normalised) – from simulation	Amplitude (normalised) – from theory
Truncated sinc	1.00	1.000	1.000
Rectangular chirp	0.82	0.299	0.295
Hamming chirp	0.92	0.295	

Table 8 Comparison of different pulses: a sinc pulse (not shown above), of the same duration as the rectangular chirp pulse, and the Hamming-windowed chirp pulse.

Table 8 also gives the relative amplitudes of the pulses, as determined both from simulation and from theory (Equation (74), exact expression). The simulation results agree very closely with the theory. Since the theory is only strictly accurate for the infinite chirp function, this shows that the truncation of the chirp pulses has negligible effect on the amplitude of the mean excitation across the centre of the bandwidth, despite the high non-uniformity of the profile in this region.

7.3.2 Experiments

k-space

The echoes produced in a chirp pulse BURST experiment are spread out in time, just as the energy of each chirp pulse is distributed over the longer pulse duration. To a first approximation the phase of each echo is expected to be quadratic, with a time-reversed phase in relation to the chirp pulse. This approximation holds best where the linear approximation applies and for a uniform phantom of infinite extent. Here the phantom (a spherical doped water phantom filling half the FoV) is clearly not uniform over the excitation bandwidth and also extends only over the central half of

the FoV. The phase of the above echoes was indeed found to deviate from this approximation. The source of this deviation was investigated.

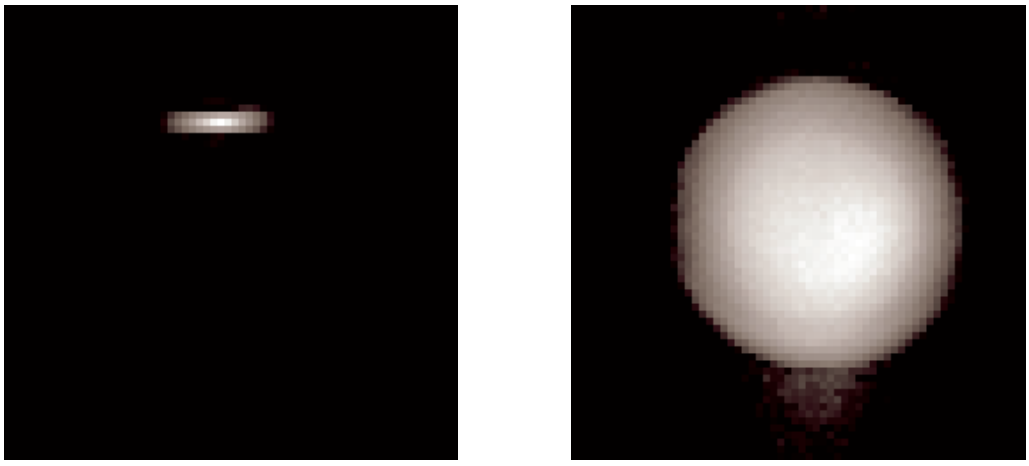

Figure 43 Data from 64-pulse BURST experiment, showing (a) k-space (horizontal readout, vertical phase encoding), and (b) reconstructed modulus image.

The phase of individual echoes from this data set shows a quadratic-like variation, but forming a broader than expected curve with one side steeper than the other. As well as the reasons stated above, another possible cause of the deviation of the phase is eddy currents. If eddy currents were decaying away through each echo, then this could result in the kind of effects observed. Additionally, any eddy currents would diminish significantly over the 30ms duration of the echo train, and this would in turn affect the phase from one echo to the next. However, when a train of BURST echoes (as in an imaging experiment) was examined, the same phase variation was seen over all echoes of the train. Therefore, since no change was seen from one echo to the next, this eddy current explanation was dismissed as a possible cause of the phase deviations.

The effect of the phantom profile was examined through simulations. For low flip angles the Fourier transform can be used to calculate the magnetisation profile and the resultant echoes. Initial simulations of a rectangular phantom showed that a narrow phantom would indeed broaden the phase variation of the echoes and, also, that an asymmetric phantom i.e. off-centre, would result in an asymmetric echo phase, similar to that observed in experiments. Following this, a more accurate

simulation was performed, which included both the profile of the spherical phantom in the imaging plane and the position of the phantom in the FoV.

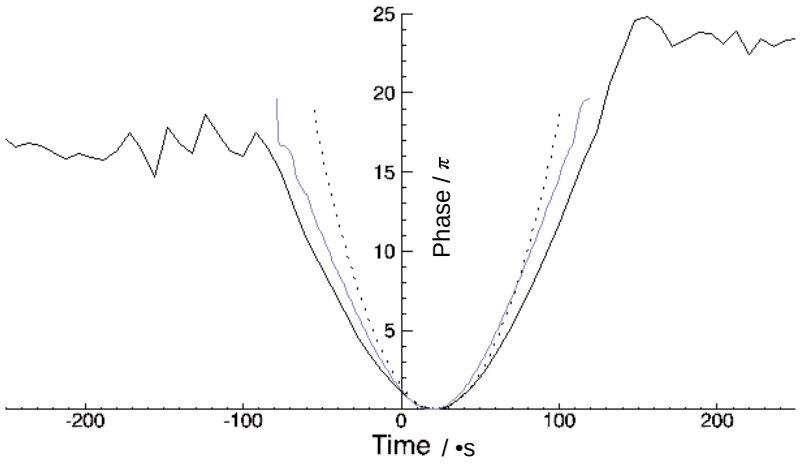

Figure 44 Phase of an echo (solid line) fitted by simulation (blue line) and by chirp phase (dotted line)

The simulated phase variation of the echoes more closely resembles that of the experimental data, but does not fit it well, as shown in Figure 44 above. The shapes of the simulated and experimental curves are similar, although the simulated curve is narrower. Clearly, the phantom shape and position affects the resultant echo phase, but other, unidentified, factors are present also.

Images

Multi-slice images through a human foot are shown below. A single foot was placed into a 27 cm diameter TEM head coil driven in quadrature mode and imaged 'coronally', as Figure 45 demonstrates. A reduction in peak power of over 90% was obtained. The full parameters, together with a set of images, are given below.

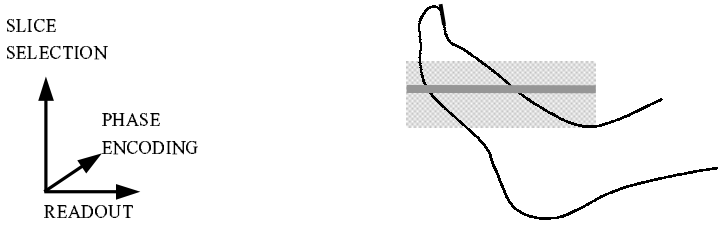

Figure 45 Sketch showing position and orientation of 'coronal' slices.

RF parameters
156 μs chirp pulse including 32 μs Hamming window 106 kHz BW

Peak Power / W	
Chirp	**540 ± 10**
Sinc (predicted)	**6200**

Phase modulation	multi-phase OUFIS
Flip angle	12°
τ_S	512 μs
$BW_{acquisition}$	100 kHz
TR	1 s
Slice thickness	10 mm
Resolution	3.1 x 3.6 mm

SNR = 30

Table 9 Experimental parameters

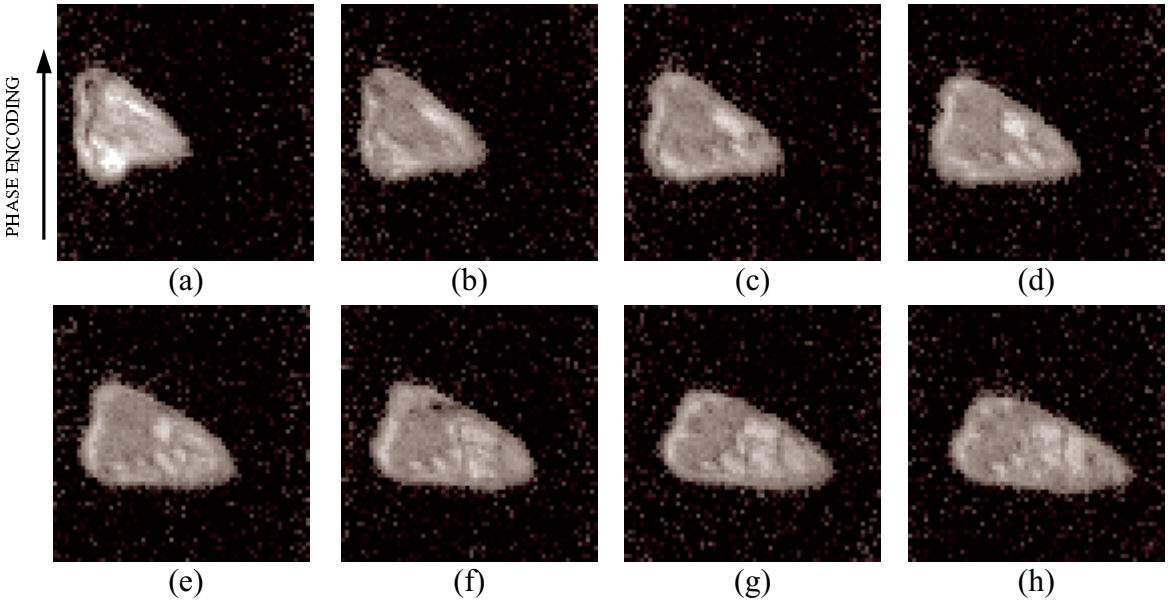

Figure 46 Multi-slice images of a human foot (readout gradient across the page). Images are shown from the top-most down [(a)-(h)].

7.4 Discussion

The peak power required in BURST can cause problems with conventional MR scanners, but with chirp pulses the sequence becomes practicable, especially at high fields and for microscopy systems. Frequency modulation can produce high bandwidth pulses with greatly reduced amplitudes compared to amplitude modulation alone. In previous work the application of FM pulses has been restricted by the dephasing of the spins, which decreases the net signal. In BURST, however, this dephasing is of no consequence – the net signal is unchanged. The use of chirp pulses does not itself reduce the total RF power, however it does lend itself to the possibility of making some reductions through refinement of the pulses.

Conventional high bandwidth (100 kHz) AM pulses are very short (~10 μs), and such short pulses cannot easily be precisely shaped, and hence cannot be designed to have optimum excitation profiles. By contrast the longer chirp pulses can be precisely shaped and this allows for the possibility of improved excitation profiles.

The quadratic phase of the RF pulse transforms into a quadratic phase of the magnetisation for a pulse of infinite duration. However, the truncation and windowing of the pulse leads to a quadratic-like phase across the excitation bandwidth, and only little excitation outside of this region. Likewise, the phantom 'windows' the excitation function, and this results in echoes with quadratic-like phase, rather than returning the phase of the RF pulse. However, even with all these parameters included in the simulations the calculated phase did not match the actual echo phase.

The most notable feature of the images is the quadratic-like phase variation along the readout direction. This could be corrected for if necessary, either by acquiring a reference image or by simulating the expected phase variation. The modulus images, however, showed no geometric distortion.

At lower fields chirp pulses will enable faster BURST imaging, which is limited by the high coil voltages required to generate very short RF pulses of the required flip angle [8]. These pulses will be of greater benefit still for multiply-refocussed BURST techniques e.g. [9] with higher flip angle pulses. At higher fields the peak power level will be greater, and the requirement for a technique to reduce it will be more urgent still.

7.5 References

1. Zha, L. and I.J. Lowe, *Optimised ultra-fast imaging sequence (OUFIS).* Magn. Reson. Med., 1995. **33**: p. 377-395.

2. Gelderen, P.v., J.H. Duyn and C.T.W. Moonen, *Analytical solution for phase modulation in BURST imaging with optimum sensitivity.* J. Magn. Reson. Series B, 1995. **107**: p. 78-82.

3. Cho, Z.H., Y.M. Ro and I.K. Hong, *FM DANTE fast imaging and variations: emerging rf-based ultrafast imaging techniques.* Concepts Magn. Reson., 1998. **10**(1): p. 33-54.

4. Kunz, D., *Use of frequency-modulated radiofrequency pulses in MR imaging experiments.* Magn. Reson. Med., 1986. **3**: p. 377-384.

5. Kunz, D., *Frequency-modulated radiofrequency pulses in spin-echo and stimulated-echo experiments.* Magn. Reson. Med., 1987. **4**: p. 129-136.

6. Maudsley, A.A., *Dynamic range improvement in NMR imaging using phase scrambling.* J. Magn. Reson., 1988. **76**: p. 287-305.

7. Johnson, G., E.X. Wu and S.K. Hilal, *Optimized phase scrambling for RF phase encoding.* J. Magn. Reson. Series B, 1994. **103**: p. 59-63.

8. Hennig, J. and M. Hodapp, *Burst imaging.* MAGMA, 1993. **1**: p. 39-48.

9. Gelderen, P.v., C.T.W. Moonen and J.H. Duyn, *Susceptibility insensitive single-shot MRI combining BURST and multiple spin echoes.* Magn. Reson. Med., 1995. **33**: p. 439-442.

8 Reducing SAR with an Oscillatory Gradient

8.1 Introduction

BURST is a technique requiring a high excitation bandwidth compared with other imaging sequences. Typically an RF bandwidth of 125 kHz is required in BURST, as opposed to 2 kHz for slice selective excitation in techniques such as EPI. There are two major consequences of this, both of which create problems, particularly at high fields. Firstly, a very high peak RF power is required which can put the technique outside the range of many RF amplifiers. The previous chapter addressed this with the use of chirp pulses. Secondly, the total RF power is large, which limits the use of the technique, putting constraints on the flip angle and the repetition time for human imaging. The maximum allowable SAR is 4 W/kg for brain excitation. This problem is tackled in this chapter through a modification to the excitation train, which can produce substantial reductions in SAR.

The BURST excitation is defined by a periodic train of RF pulses in the presence of a gradient across the FoV. This causes the spins to move in alternate steps of nutation and precession, and this leads to a cumulative tipping of the spins into the transverse plane for spins on-resonance and at a series of harmonic offset frequencies [1]. At in-between frequencies the overall flip angle is much smaller.

The basic components of this spin evolution are the nutation, driven by the transverse RF component, and the precession, driven by the longitudinal RF component i.e. the gradient. From this viewpoint it is clear that the gradient is not required during the RF pulse. Therefore, the gradient can be reduced during the application of the pulse, which will reduce the bandwidth requirement, and hence the total power, of the RF pulse. Also, the gradient between pulses can be increased and the inter-pulse duration decreased so that the original pulse train duration will be maintained. In practice it is easier to implement a smoothly varying gradient, to produce a partial reduction in bandwidth.

Each RF pulse of the train has to be altered to give as good a response with the time-varying gradient as with the constant gradient. This can be most simply achieved

using the VERSE transform [2]. In fact, the VERSE principle provides a more general explanation of the method of the oscillatory gradient in BURST: by viewing the technique as a transform of the entire pulse train, there need be no reference to the motion of the spins.

Additionally, the peak power is reduced by this technique. It can be used on its own or in combination with chirp pulses, so that a suitable set of parameters can be chosen to meet both the system i.e. peak power, and SAR constraints.

8.2 Theory

8.2.1 Time-varying gradient

A periodic train of RF pulses excites spins at periodically displaced frequencies, with a separation depending on the pulse spacing. Earlier, the motion of the spins under the alternate steps of nutation and precession of the RF train was described (see Section 3.7.3). Spins on resonance are tipped down to the transverse plane by the cumulative action of the pulses, and similarly at harmonic offset frequencies spins are also tipped fully down by the pulses. At in-between frequencies, where the precession is not a whole number of cycles, a reduced flip angle results.

In this idealised description of the spins' motion the periods of nutation and precession are separate, which would correspond to a train of instantaneous RF pulses. The spins can be made to trace out the same path if the gradient is switched on and off with finite RF pulses applied during the off periods. In this way the high bandwidth problem can be completely ameliorated. A constant gradient would still be used during the echo acquisition.

In practice the gradient need only be switched low, rather than off, during the RF pulses (as shown in Figure 47(ii) below) to give more than enough bandwidth reduction. The response of the spins to the RF pulses can be kept unchanged if the RF duration is scaled inversely with, and the amplitude scaled directly with, the gradient. A pulse of twice the duration and half the amplitude and gradient will produce the same response as the original pulse. Similarly, the precession in-

between RF pulses is determined by the time integral of the gradient, and so a higher gradient of shorter duration can be used. Hence, by switching the gradient low during and high in-between pulses the overall duration of the pulse train can be kept the same.

More useful would be a smoothly varying gradient, such as a sinusoidal waveform superimposed onto the constant gradient (as shown in Figure 47(iii)). This would be less demanding on the gradients, keep eddy currents to a minimum and reduce the contributions from higher harmonics to the acoustic noise. Each RF pulse is positioned over a gradient minimum and the period of the sine wave is equal to the pulse spacing. In this method the pulse cannot readily be stretched and scaled, as for a switched two-level gradient, however, a generalisation of this idea, the VERSE transform, describes a method for deriving a new pulse from the original pulse.

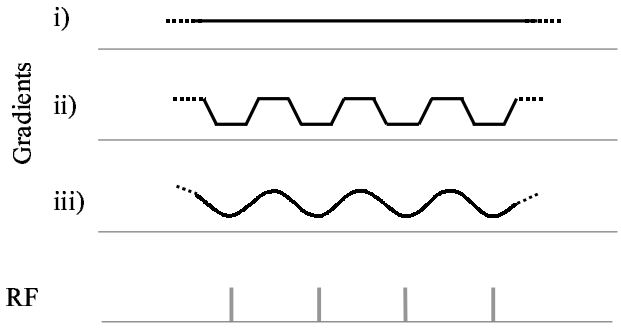

Figure 47 Segment of the BURST RF train shown with three possible gradients: i) constant, ii) switched and iii) oscillatory.

8.2.2 VERSE

VERSE (*v*ariable*-r*ate *s*elective *e*xcitation) [2] is the name of a straightforward technique for transforming a spatially selective pulse and gradient into an alternative pulse and gradient, which are typically chosen to have a lower SAR than the original sequence. It draws an additional degree of freedom into pulse development and it can be applied to any pulse. The derived pulse and gradient produce an identical response to the original pulse and gradient.

The basic idea is similar to that mentioned above – a pulse can be stretched and scaled in proportion to the gradient to yield another pulse and gradient with the same response. This works because the net B field is scaled inversely with the overall duration, so that the total rotation of the spins is the same. In this way the amplitude and total power of a pulse can be controlled. More generally, different portions of a pulse can be stretched and scaled by different amounts, which allows for a great deal of flexibility in transforming the pulse and enabling amplitude and duration constraints to be brought in. This is the basis of VERSE.

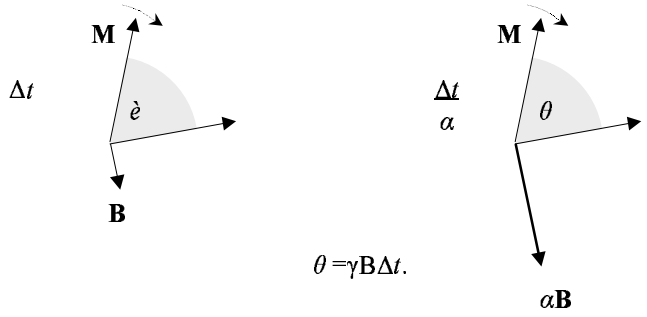

Figure 48 The path of the magnetisation is the same for different combinations of **B** and Δt

The rotation of the spins is described by the Larmor relation, $\omega = \gamma B$.
The transverse components of **B** are the applied RF, and the longitudinal component is proportional to the gradient. A single rotation (constant **B** over a time Δt) is given by $\theta = \omega t = \gamma B \Delta t$. The same rotation will be obtained if **B** is scaled up and Δt scaled down so that the product is unchanged. If the amplitude of the RF is lowered, the total power will also be lowered.

Starting with a piecewise definition of an RF pulse each element can be independently scaled together with the corresponding gradient element, which allows for the whole pulse to be transformed according to some pre-defined constraint e.g. minimum SAR for a fixed duration. In BURST the constant gradient is to be replaced with an oscillatory gradient, the amplitude and period of which will determine the transformation of individual RF pulses. The duration of each pulse will increase and, in general, the peak amplitude will decrease and, most importantly, so will the total power. This technique can be applied in combination with the chirp

pulses of the previous chapter, with the chirp pulse and the gradient oscillation chosen to meet the necessary peak power and SAR constraints. However, these two techniques put conflicting requirements on the RF pulses in one respect; longer chirp pulses have lower peak powers, yet shorter pulses (of a given shape) lead to greater reductions in SAR. If a transformed pulse fills only the minimum in the gradient oscillation, it will have a lower net power than a pulse which spills across the rising edges of the gradient, and hence, optimal gains result from the shortest pulses. The benefits of the two techniques can be set against one another to formulate a pulse meeting both the system and SAR constraints. In practice at 3T it was found that these requirements did not restrict the formulation of the pulses and there was ample scope in the possible choices of chirp and gradient parameters.

Connolly et al. [2] used VERSE to minimise the SAR of a pulse while keeping its duration constant. Such optimised pulses were shown to have constant magnitude. It is interesting to note, therefore, that the highly uniform chirp pulses are themselves almost minimum SAR pulses; that is, there can only be a small further reduction in SAR through an optimised VERSE transform subject to the constraint of a constant pulse duration. It might be expected that the switched gradient method (Figure 47(ii)) will result in a lower power deposition than the oscillatory gradient method (Figure 47(iii)) for a given duration of refabricated chirp pulse. VERSE transformation with the switched gradient will result again in chirp pulses, still uniform but of longer duration, whereas with the oscillatory gradient transformation will lead to a roughly sinusoidal pulse profile, reflecting the gradient envelope. However, it was observed that this was not necessarily correct. Indeed, the pulse shown in Figure 51 in Section 8.3.1 below has a lower power than a pulse derived for a switched gradient (not shown). In general, whether or not this is the case will depend on the truncation of the chirp pulse and its duration.

As a final comment, the VERSE principle provides a complete explanation of the oscillatory gradient method, without need to refer to nutation and precession. This modification to BURST can be viewed as a single VERSE transform of the entire pulse train, with the shape and amplitude of the gradient oscillation determining the transform of the RF pulses. The bandwidth of each pulse is reduced, and there are corresponding reductions in the SAR and peak power of each pulse.

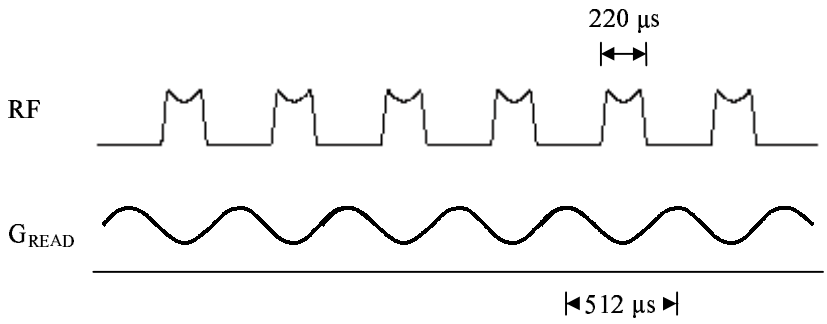

Figure 49 Section of a modified BURST sequence showing the profile of chirp pulses transformed to match the oscillatory gradient. Typical pulse and waveform parameters are given.

8.2.3 VERSE transform of chirp pulses with an oscillatory gradient

For an initial RF pulse defined piecewise in n elements with a constant time step Δt, the total duration is given by

$$T_1 = \sum_{i=0}^{n-1} \Delta t = n\Delta t \,. \tag{90}$$

If this pulse is applied under one gradient waveform (G_1), which is then replaced with another gradient waveform (G_2), each time step will be scaled by the ratio of the gradients at the corresponding points in time. The reformed pulse duration is given by

$$T_2 = \sum_{i=0}^{n-1} \frac{G_1(i\Delta t)}{G_2(t_i)} \Delta t \,, \tag{91}$$

where t_i is equal to the sum of the preceding time steps in the reformed pulse,

$$t_i = \sum_{j=0}^{i-1} \frac{G_1(j\Delta t)}{G_2(t_j)} \Delta t = t_{i-1} + \frac{G_1((i-1)\Delta t)}{G_2(t_{i-1})} \Delta t \,. \tag{92}$$

If one of the gradients is constant and the other time-varying, it is simpler to develop this expression for the reformed pulse duration by choosing a constant time step for the time-varying gradient; that is, with G_1 as the time-varying gradient and G_2 as the constant gradient (see Figure 50). Then, since the gradient in the denominator in Equation (91) is constant, this avoids the difficulty of evaluating t_i.

In which case,

$$\Rightarrow \qquad T_2 = \sum_{i=0}^{n-1} \frac{G_1(i\Delta t)}{G_2} \Delta t \,. \tag{93}$$

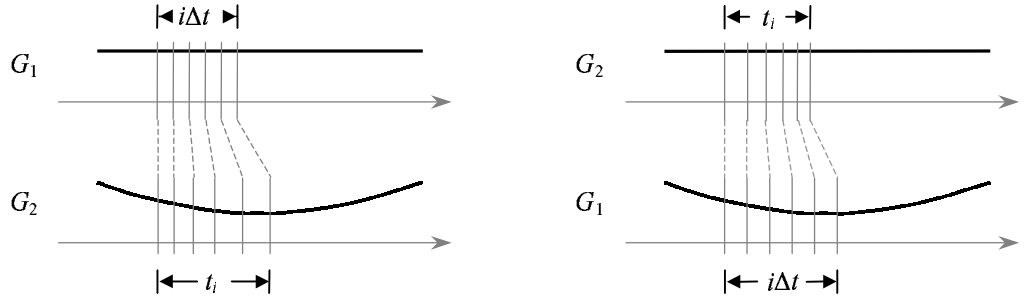

Figure 50 The constant time step can be applied either to the original pulse/constant gradient, as in (a), or to the refabricated pulse/time-varying gradient, as in (b). The calculation is simplified in (b) as the gradient G_2 does not need to be recalculated for different t_i.

In the limit as Δt→0 this summation becomes an integral,

$$T_2 = \int_0^{T_1} \frac{G_1(t)}{G_2} dt \,. \tag{94}$$

For $G_1 = G_0(1-\alpha(\cos(\omega t))$ and $G_2 = G_0$ (constant) for $-T_1/2 < t < T_1/2$, where α is the fractional amplitude of the oscillation,

$$T_2 = \int_{-T_1/2}^{T_1/2} 1 - \alpha\cos(\omega t)\ dt = T_1 - \frac{2\alpha}{\omega}\sin(\omega T_1/2), \tag{95}$$

where T_2 and T_1 are the durations of the original pulse and the reformed pulse respectively.

The energy of a pulse defined piecewise is given by

$$SAR = \sum_i I_i \Delta t_i \propto \sum_i A_i^2 \Delta t_i \,, \tag{96}$$

where I_i is the instantaneous power of the i^{th} element, proportional to the square of the amplitude (A_i), and Δt_i is the duration of the element.

As above, a constant time step (Δt_1) is chosen for the time-varying gradient (G_1) i.e. for the refabricated pulse. The time steps for the constant gradient (G_2) are given by

$$\Delta t_{2i} = \frac{G_1(i\Delta t_1)}{G_2}\Delta t_1, \tag{97}$$

and the pulse element amplitudes are given by

$$A_2(t_{2i}) = \frac{G_2}{G_1(i\Delta t_1)} A_1(i\Delta t_1), \tag{98}$$

where t_i is given by Equation (92) above.

Substituting for Δt_{2i} and A_1, the ratio of the SARs of the initial (SAR_2) and the reformed (SAR_1) pulses is

$$\frac{SAR_2}{SAR_1} = \frac{\sum_i A_{2i}^2 \Delta t_{2i}}{\sum_i A_{1i}^2 \Delta t_1} = \frac{\sum_i A_{2i}^2 \frac{G_1(i\Delta t_1)}{G_2}\Delta t_1}{\sum_i A_{2i}^2 \left(\frac{G_1(i\Delta t_1)}{G_2}\right)^2 \Delta t_1}. \tag{99}$$

For chirp pulses the amplitude A_2 is approximately constant. With this approximation and in the limit $\Delta t \to 0$ this expression becomes

$$\frac{SAR_2}{SAR_1} \approx \frac{\int_{T_1} \frac{G_1(t)}{G_2} dt}{\int_{T_1} \left(\frac{G_1(t)}{G_2}\right)^2 dt}, \tag{100}$$

where T_1 is the duration of the refabricated pulse.

This gives a useful approximation for the reduction in SAR which will arise from the use of VERSE-transformed chirp pulses in combination with a time-varying gradient.

8.3 Results

8.3.1 Calculation of transformed chirp pulses

Transformation of the chirp pulse in Figure 51 (black line) leads to predicted reductions in SAR of 18% and 32%, corresponding to gradient oscillations of 20% and 40% amplitude respectively. The approximation given by Equation (100) above, overestimated these SAR gains by a few percent. The table below gives further pulse details.

Oscillation amplitude	SAR reduction	Peak power reduction	Pulse duration
None (α=0)	-	-	156 µs
20 % (α=0.2)	18 %	28 %	186 µs
40 % (α=0.4)	32 %	43 %	220 µs

Table 10 Performance of VERSE-transformed chirp pulses evaluated by calculation. The reductions in power are given relative to the original pulse (top line).

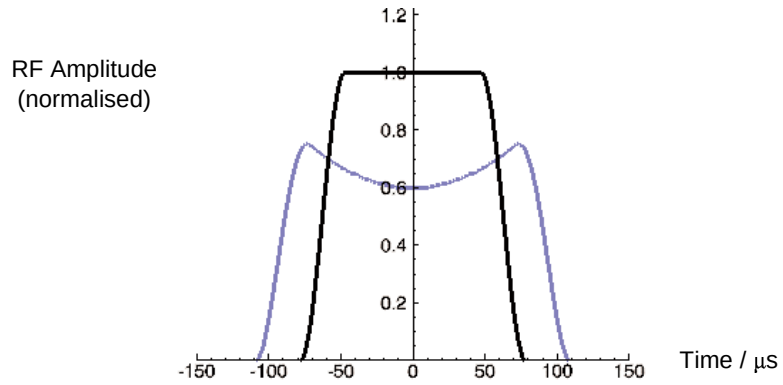

(a)

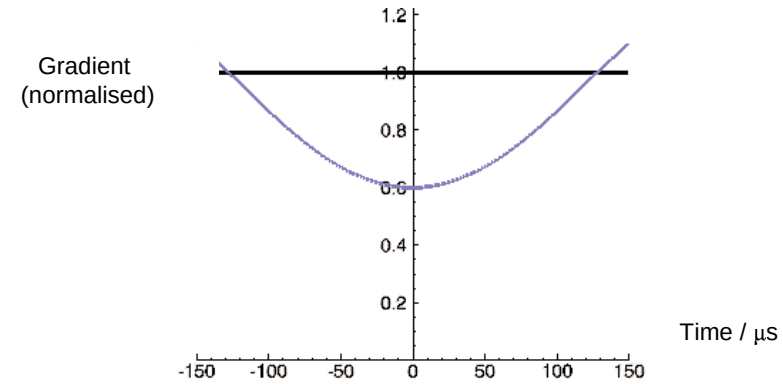

(b)

Figure 51 Corresponding RF and gradient profiles. Black line – chirp pulse and constant gradient, blue line – VERSE transformed pulse with 40 % (α = 0.4) gradient oscillation.

8.3.2 Experiments

Multi-slice images through a human foot are shown below. As previously, a single foot was placed into a 27 cm diameter TEM head coil driven in quadrature mode and imaged 'coronally'. The full parameters, together with a set of images, are given below.

Gradient and RF parameters	
40% gradient oscillation with VERSE-transformed 156 μs chirp pulse	
Peak Power / W	
VERSE'd chirp	**280 ± 10**
Chirp	**540 ± 10**

Phase modulation	multi-phase OUFIS
Flip angle	12°
τ_S	512 μs
$BW_{acquisition}$	100 kHz
TR	1 s
Slice thickness	10 mm
Resolution	3.1 x 3.6 mm

SAR reduction = **38 ± 2 %**	SNR = 35

Table 11 Experimental parameters

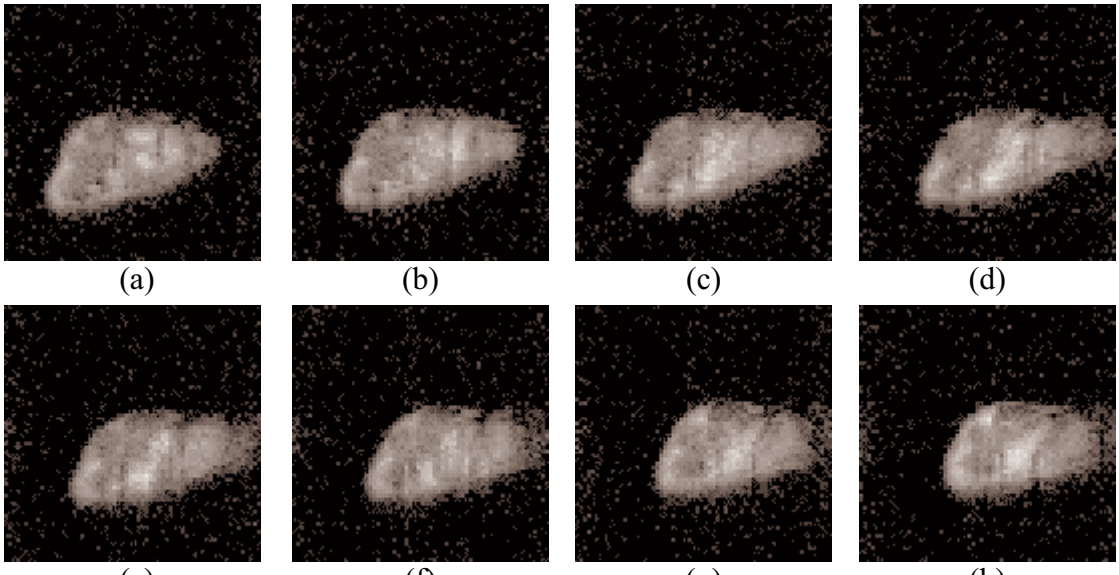

Figure 52 Multi-slice images of a human foot (readout gradient across the page).

The measured SAR reduction was greater than that predicted. The SAR figure in Table 11 is based on the difference in the measured peak powers of the two pulses. These were read from the digital display on the RF amplifier as the pulses were applied. The reading errors quoted on these measurements do not reflect the shot-to-shot fluctuations in the readings, and therefore are likely to underestimate the true

errors. This could explain the discrepancy between the SAR figures. No image artefacts were observed with this technique. However, the high frequency gradient oscillations introduce high pitch noise to the sequence. It was found that even for small amplitudes of oscillation the noise was moderate, and earplugs might be necessary.

8.4 Conclusions

This chapter has described a technique which can overcome the high SAR problems associated with high field BURST imaging. The reduction in total power can be controlled through the amplitude of the oscillation. A smoothly varying envelope is employed which minimises any eddy currents. Another benefit of this technique is that it reduces the peak pulse power, another constraining factor at high fields. Additionally, the chirp pulse of the previous chapter can be used in conjunction with this technique, which will give greater control still over the pulse SAR and peak power. The most notable drawback is the introduction of a moderate amount of acoustic noise to a sequence known for its quietness. The gentle 'clunk' is replaced by a marked high pitch noise, even for small oscillations.

8.5 References

1. Morris, G.A. and R. Freeman, *Selective excitation in Fourier Transform Nuclear Magnetic Resonance.* J. Magn. Reson., 1978. **29**: p. 433-462.

2. Conolly, S., D. Nishimura and A. Macovski, *Variable-rate selective excitation.* J. Magn. Reson., 1988. **78**: p. 440-458.

9 Conclusions

BURST has been implemented on a 3T whole body imaging system. It has produced images with little distortion and relatively free from artefacts. It has been shown that the sequence is sensitive to both T_2 and diffusion, and that with parameters typical to that of the human brain the T_2 attenuation is markedly greater than that due to diffusion. The work in this thesis has in part been limited by the constraints of the system, but it has also led to progress in some key areas.

SNR

BURST is hindered by a low SNR compared with other fast techniques, while suffering from the common problem of a high acquisition bandwidth. It was expected that the higher field in Nottingham would lead to improvements in SNR compared with that presented in publications of work at lower fields. At 3T the highest SNR obtained from human brain images was found to be approximately 40, which falls short of the SNRs reported in some earlier work carried out at just 1.5T. However, it is not possible to be able to make a precise comparison since there is a lot of variability in the SNR data presented at 1.5T, even when the different parameters in each experiment are taken into account. Only one publication exists of brain images at 3T: the STEAM-BURST technique achieved SNRs of up to 20 using stimulated echoes. However, if this SNR is adjusted to take account of the differences in the sequences – stimulated echoes (resulting in a lower signal), bandwidth, attenuation, resolution and flip angle – it comes out a few times higher than the SNR of 40. Also, comparisons were made on the Nottingham scanner between BURST and EPI, which demonstrated that BURST performed at least as well, if not better, than expected. In a set of phantom images it was found that both sequences gave a similar SNR, contrary to expectations. However, in general, EPI images of the human brain acquired on the scanner have a higher SNR than the figure of 40 for BURST above. Therefore, this suggests that the low SNR is in part due to the hardware. It is not clear whether the expected gains from higher fields are fully realised.

The alternative amplitude and phase modulations which have been developed provide a modest improvement to the signal. Amplitude modulation of the pulse

train, in combination with existing phase modulations, has been shown to provide small gains in signal. The novel combined amplitude and phase modulations have been shown to offer a much more versatile method for controlling the echo amplitudes. Modest signal improvements can be obtained with little loss of resolution, while much larger signal gains are possible but only to the detriment of the resolution. A compromise can be chosen depending on the application in question.

Experiments were carried out to detect brain activation in response to an acoustic stimulus using an existing protocol. Spin echoes were acquired to give T_2 contrast, which produces a more spatially precise response but at a lower order of magnitude, since it is dependent only on the diffusion of water molecules in the localised field gradients. The processed data showed possible clusters of activation in the relevant part of the brain. However, the data was noisy and it was unclear whether the apparent activation was significant. It would be useful to be able to use BURST for functional work, and particularly for acoustic studies, but it could not be pursued here for lack of SNR.

RF Power

In implementing BURST at 3T a major obstacle was found to be the levels of peak RF power required, which were far greater than could be obtained with the in-house amplifier. A solution has been proposed which produces up to an N_x-fold reduction, where N_x is the number of DANTE pulses, in peak power. It was shown that the introduction of chirp pulses into the BURST sequence does not result in signal loss, which has usually precluded their implementation in conventional imaging sequences. The quadratic-like phase along the readout direction can be corrected for if required, however the modulus images were not affected. When used in combination with some of the phase modulation schemes, an appealing double quadratic phase progression results - the phases of the individual pulses and the phase modulation of the pulse train are both quadratic. This peak power problem affects both the existing phase modulation BURST sequences, as well as the more demanding combined modulations explored in Chapter 6. At higher field the peak

power will be greater than that required at 3T, and chirp pulses will be of greater importance still.

The problem of the total RF power deposition has been overcome with the introduction of a time-varying gradient. At 3T the RF power approached the SAR limit, and at higher fields the RF power would be even greater. The oscillatory gradient was shown to be able to give reductions in RF power of over 30%. The response of the spins was unchanged following the VERSE transformation of the pulses. This method also reduces the peak power (a reduction of over 40% was demonstrated). However, along with the oscillatory gradient there is the introduction of high pitch acoustic noise. Whilst the technique remains less noisy than EPI it is no longer a quiet technique. Nonetheless, this technique, when used in combination with the chirp pulses, has enabled BURST to be implemented at 3T with optimised parameters.

Other issues

BURST was also used, if unsuccessfully, to acquire a single shot 3DFTdata set. The gradient was reversed a number of times, and each set of refocussed echoes was used to encode a plane in k-space. With only in-plane encoding gradients applied, it was found that the echoes began to spread out with successive refocussing. This effect arose due to eddy currents in the structures of the magnet, and it was possible to correct it with the pre-emphasis unit. The main difficulty encountered was the shot-to-shot variability in the positions of the echoes. This instability, the source of which was not traced, meant that it was not possible to correct for the variations and the technique was not pursued further.

Eddy currents, resulting from the excitation and readout gradients, were an issue in all the experiments. It was found that ramping the gradient more gently did not improve this effect. However, in the main it was possible to successfully compensate for this with the pre-emphasis unit.

In summary, in this work BURST has not so far proved to be a practical routine technique for human imaging at 3T. However, the results are encouraging for the

implementation of BURST at higher fields. The signal gains at higher fields and the image qualities of BURST might make this a useful tool for research, particularly for functional work. The modifications developed in this thesis increase the scope of the sequence. Its implementation at higher fields is now feasible. However, it might necessarily become an acoustically noisy technique in SAR-limited applications. It could be of most use as a multiply-refocussed technique, using shorter trains of RF pulses of higher amplitude. More specifically, it might find use in a multi-element excitation (A. Magill and P. Glover, *Multiple excitation strategies for imaging at ultra-high field*, ESMRMB, Copenhagen, 2004), which can be used to tackle the wavelength effects encountered at higher fields.